Cirrus clouds in the extratropical tropopause and lowermost stratosphere region

Dissertation

zur Erlangung des Grades
Doktor der Naturwissenschaften (Dr. rer. nat.)

von
Irene Bartolomé García

vorgelegt am
23.09.2021

an der
Bergischen Universität Wuppertal
Fakultät für Mathematik und Naturwissenschaften
Institut für Atmosphären und Umweltforschung

Abstract

Cirrus clouds play a fundamental role in the radiative balance of the Earth and have an important impact on the climate. Their net effect depends on their physical characteristics, i.e., altitude, vertical extent, optical thickness and particle size. Quantifying the properties of ice crystals from the observations is a very challenging task. Consequently, models used for climate projections lack observational constrains when predicting the processes related to the evolution of cirrus and their properties. The aim of this thesis was to gain a deeper understanding of cirrus macro-physical properties (cloud top and bottom height, vertical extent, position with respect to the tropopause) and of the micro-physical properties (ice water content (IWC), particle size). For this purpose, data measured by GLORIA (Gimballed Limb Observation for Radiance Imaging of the Atmosphere) during the WISE (Wave-driven ISentropic Exchange) campaign were analyzed. GLORIA is an airborne limb remote sensor that measures radiance in the thermal infrared region ($700\,\mathrm{cm}^{-1}$ to $1\,400\,\mathrm{cm}^{-1}$). Two identification methods were used to detect clouds in the measurements. One mehtod is based on the cloud index (CI) and the other method, on the use of the extinction coefficient in the spectral range $832\,\mathrm{cm}^{-1}$ to $834\,\mathrm{cm}^{-1}$. Between $13 - 27\,\%$ of the total number of observations presented a cloud top located above the tropopause (TP). However, no cirrus layers were found unambiguously above the TP (i.e., both cloud top and cloud bottom above the TP). To estimate the micro-physical properties a combination of two approaches was used. The IWC was then integrated to obtain the ice water path (IWP). The IWP was compared to the ERA5-based dataset, giving satisfactory results (qualitatively) and highlighting that the ERA5 reanalysis does not reproduce most of the very thin clouds close to the tropopause. Quantitatively, the retrieved IWP was smaller than the ERA5-based IWP, pointing to the need of reducing uncertainties to obtain a more accurate product. Additionally, observed cloudy regions close to the TP were selected as case studies to simulate with CLaMS-Ice (Chemical Lagrangian Model of the Stratosphere). The model was able to sucessfully form clouds in the region of interest.

Contents

Chapter 1

Introduction

Weather phenomena, because of their impact on the daily life, have awaken interest since the Antiquity, when the first texts about clouds, rain and seasons were written. These texts were not following the established scientific method, but rather intuition and simple observations. It was not until 1803, when Luke Howard published the first classification of clouds, *Essay on the Modification of Clouds* (Howard, 2011), according to their appearance and process of formation. This initial classification covered only some of the tropospheric clouds and gave them the Latin names that are still used nowadays. Since then, much has changed and our knowledge about clouds has increased thanks to the development of new measuring techniques, instruments and models.

Currently, we know that clouds can be formed by liquid droplets, ice crystals or a mix of both. Tropospheric clouds are divided according to their altitude in low, middle and high clouds. Additionally, clouds in the stratosphere and in the mesosphere have been identified, usually in the polar regions (World Meteorological Organization, last accessed: 28 April 2021). We also know that clouds cover about two thirds of the globe (IPCC, 2013) and do not distribute homogeneously, but rather that their distribution varies by latitude (and season) following low pressure zones, where air masses converge at the surface and rise. Clouds form more often close to the equator (Inter Tropical Convergence Zone (ITCZ)) and around 60° in both hemispheres. (Fig.1.1). Low clouds typically appear over oceans, specially over subtropical oceans and in polar regions. Mid-level clouds

commonly form in storm tracks and in the ITCZ and high-level clouds appear often near the equator and over tropical continents, although can also occur at mid-latitudes over continents in summer and at the storm track regions (IPCC, 2013).
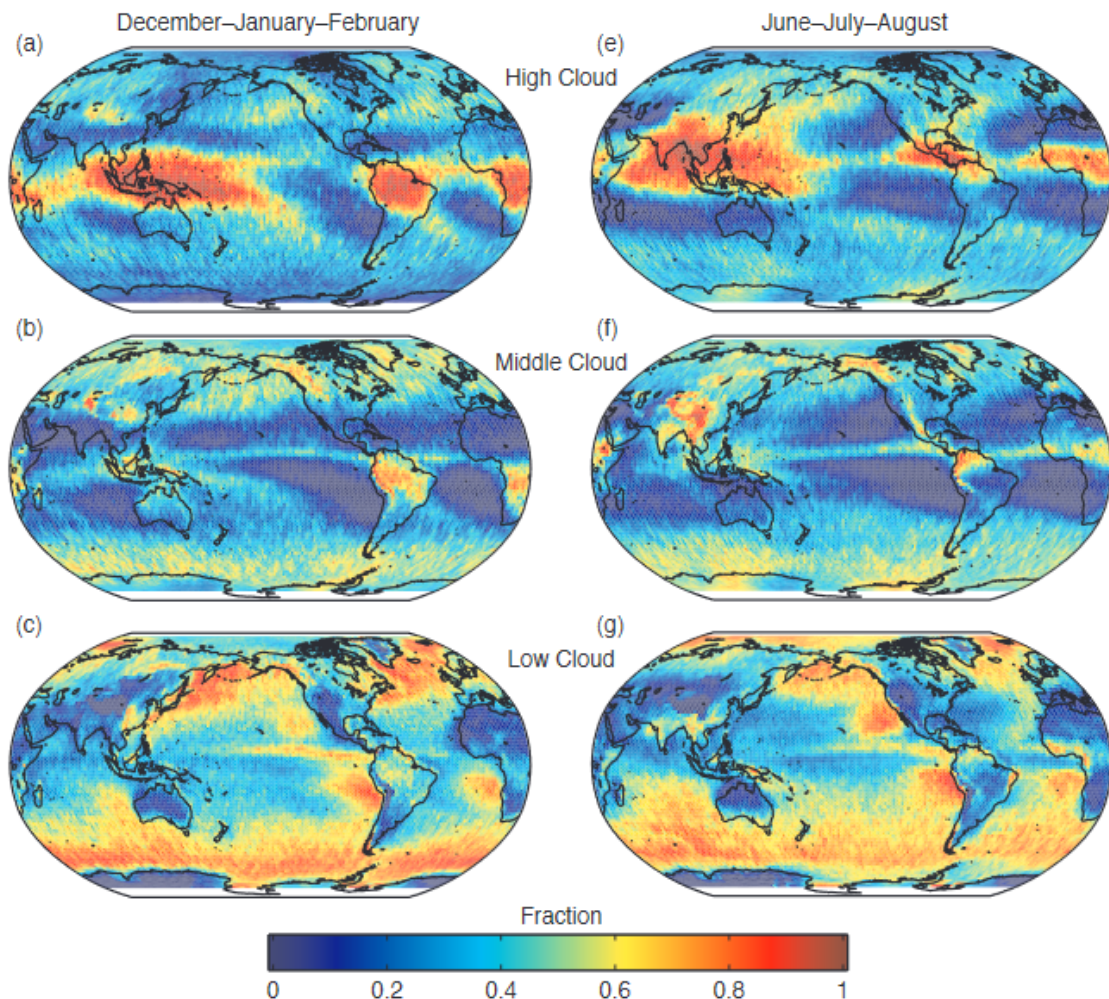
Figure 1.1: (a-c) Mean global distribution of high, middle and low clouds for December-January-February from CloudSat/CALIPSO 2B-GEOPROF R04 and 2B-GEOPROF-LIDAR P1.R04 dataset for 2006-2011 (Mace et al., 2009). (e-g) same as (a-d) but for June-July-August. Figure adapted from Fig. 7.6 of IPCC (2013).

It is also known, that clouds produce a large impact on the weather and climate, which makes them such an important and interesting subject of study. On one hand, clouds can increase the planetary albedo, thus reflecting back to space part of the shortwave solar incoming radiation and leading to a cooling of the surface. On the other hand, clouds can warm the Earth by absorbing the longwave outgoing infrared radiation (greenhouse
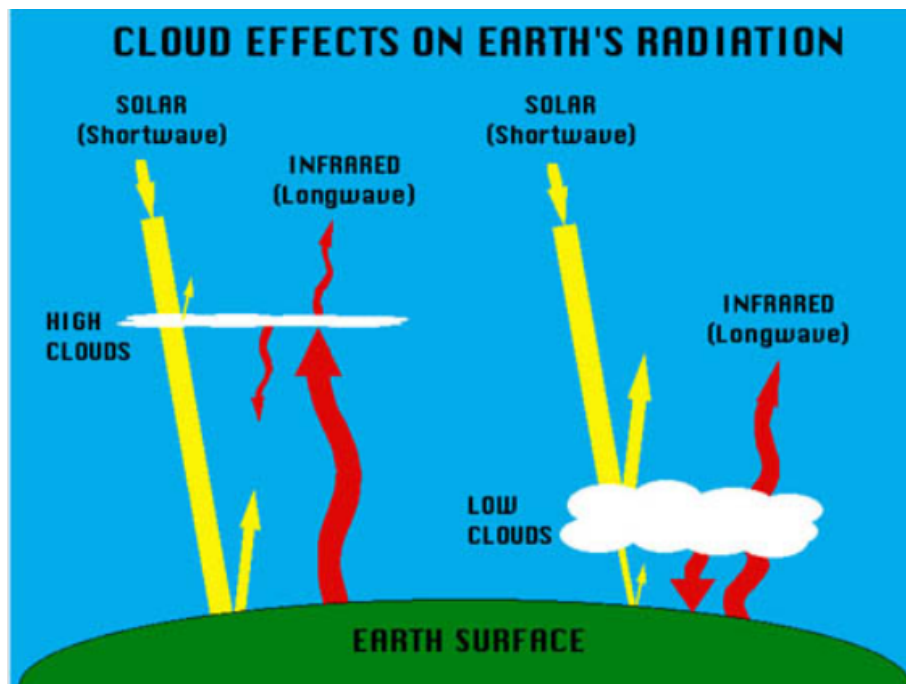
Figure 1.2: Scheme describing the radiative effect of clouds. The overall effect of high clouds is warming, as they are almost transparent to the incoming solar radiation, but block very well the outgoing infrared radiation. As high clouds emit at much lower temperatures, they produce a net warming effect at the top of the atmosphere. Lower thicker clouds cause a cooling because they are good reflectors of solar radiation and let infrared radiation escape to space. Credit: NASA

effect). Their net effect is the sum of both effects, which currently is estimated to be negative, thus clouds overall cool the Earth (IPCC, 2013). However, their effect in a changing climate is not clear, as it is an open question how clouds will be affected. Each kind of cloud has different characteristics, i.e., different altitude, different particle size, different vertical extent, different formation process, different optical thickness, etc. All these properties influence what impact on the radiative budget of the Earth clouds have. For example, low clouds have a cooling net effect, whereas high clouds have a warming net effect (Fig.1.2).

The large diversity in clouds properties leads to great challenges when understanding cloud processes and feedbacks. Consequently, despite being the subject of many studies, processes related to clouds are still not well understood. Therefore, the evolution of clouds and their radiative effects (also in the context of climate change) remain an important open question of climate science. A main reason for this is that quantifying

3

cloud properties from the observations is a challenging task. Remote sensing instruments (both active and passive, from satellites or aircrafts or ground-based) might not be sensitive enough to detect the very translucent clouds. Also multi-layer cloud systems pose a problem when retrieving cloud properties. In situ instruments are capable of detecting the thinnest clouds, but they only capture a temporally and spatially limited snapshot. As a consequence, physical models used for climate projections suffer from a lack of observational constraints when predicting the very complex processes related to the evolution of clouds and of their properties. To contribute to the solution of this problem, this thesis focuses on the retrieval and analysis of properties of high clouds in mid-latitudes observed by the limb sensor Gimballed Limb Observer for Radiance Imager of the Atmosphere (GLORIA) (Riese et al., 2014; Friedl-Vallon et al., 2014). In the following, more specific aspects about high clouds are introduced.

High clouds, composed of ice crystals, are formed in the upper troposphere, where the temperatures are lower than –38 °C. It is possible to differentiate three main groups: cirrus, cirrocumulus and cirrostratus. The first one consist of white delicate filaments, the second one of banks of small, white flakes and the third one of translucent cloud veils. According to Sassen et al. (2008), these high clouds cover 16.7 % of the Earth's surface on average. All these clouds (from now on simply cirrus) are important, due to their frequent occurrence and their effect on the radiative budget of the Earth (Liou, 1986). According to Sassen and Cho (1992) cirrus clouds are defined as optically thick for an optical depth $\tau > 0.3$, optically thin for $0.03 < \tau < 0.3$ and subvisible cirrus (SVC) for $\tau < 0.03$ in the visible wavelength region. The characteristics of the cirrus are determined by the formation process. For example, cirrus formed in slow updrafts have a few large ice crystals and low ice water content (IWC) [1] (Krämer et al., 2016). This type of cirrus are optically thin and cause a warming effect. On the contrary, cirrus formed in fast updrafts have a large number of small ice crystals and high IWC. This type of cirrus are optically thick and have the potential to cool. Another type of optically thick cirrus, also with a cooling effect, are the ones first formed as liquid clouds at an altitude where

---

[1] Ice water content (IWC) is the cloud ice mass in a unit volume of atmospheric air.

the temperature is higher than the cirrus temperature range (–38 °C), and later uplifted. These cirrus also have high IWC, but larger ice crystals.

Of special interest is the effect of cirrus clouds in the upper troposphere–lowermost stratosphere (UTLS) region. Even small changes in the concentration of water vapor in this region affect the radiative forcing of the atmosphere (Riese et al., 2012). The presence of cirrus clouds above the tropopause, that will evaporate as soon as they experience a temperature increase and thus contribute to the water vapor budget, is still an ongoing discussion. While Dessler (2009), indicated the existence of a substantial amount of cirrus above the tropopause, Pan and Munchak (2011), using the same Cloud-Aerosol Lidar with Orthogonal Polarization (CALIOP) data, demonstrated that the amount of cirrus clouds above the tropopause strongly depends on the definition of the tropopause. Moreover, Pan and Munchak (2011) concluded that there is not enough evidence of clouds above the tropopause in mid-latitudes. A follow up study by Spang et al. (2015), using the measurements from the Cryogenic Infrared Spectrometers and Telescopes (CRISTA) and ERA-Interim [2] temperature fields for the determination of the local tropopause, concluded that there is a significant number of occurrences in the lowermost stratosphere at mid and high latitudes. A recent study with the Michelson Interferometer for Passive Atmospheric Sounding (MIPAS) and CALIOP by Zou et al. (2020) found that CALIOP observed occurrence frequencies of about 2 % of stratospheric cirrus clouds at mid and high latitudes and 4–5 % for MIPAS at mid-latitudes (six year mean global distribution 2006-2012). Other studies based on measurements by ground-based lidars showed thin cirrus that were unambiguously located in the lowermost stratosphere (Keckhut et al., 2005). In the analysis of Goldfarb et al. (2001) using data from northern mid-latitudes, cirrus cloud tops often occurred at the tropopause and SVC constituted 23 % of the total occurrences of cirrus clouds.

Detection of optically thin cirrus clouds and SVCs is a challenge due to the need of high vertical resolution and high sensitivity. Martins et al. (2011) analyzed CALIOP measurements over 2.5 years and gave an insight into the global occurrence of SVCs,

---

[2]ERA-Interim is a global atmospheric reanalysis dataset provided by the European Center for Medium-Range Weather Forecasts (ECMWF).

being more common in the tropics (30-40 %). Reverdy et al. (2012) reported a significant population of SVCs in the tropical upper troposphere. However, Davis et al. (2010) found that Cloud-Aerosol Lidar and Infrared Pathfinder Satellite Observations (CALIPSO) would be missing about 2/3 of SVCs with $\tau < 0.01$. Due to the long path of the line-of-sight of a limb sounding instrument through the cirrus, clouds that might be invisible to the nadir viewing instruments, are detectable. Spang et al. (2008) detected optically thin clouds with IWC of down to 0.01 ppmv using the airborne limb instrument Cryogenic Infrared Spectrometers and Telescopes-New Frontiers (CRISTA-NF). This IWC matches the lower limit of the expected IWC for mid-latitude cirrus clouds $0.01 - 200$ ppmv (Luebke et al., 2016). As mentioned before, the data analyzed in this thesis was measured by GLORIA, an airborne limb sensor that possesses the technical characteristics necessary for the detection of thin cirrus and SVC. It has a spatial sampling of 140 m $\times$ 140 m (horizontal sampling $\times$ vertical sampling) at a tangent point altitude (i.e closest point of the line-of-sight to the Earth's surface) of 10 km for a flight altitude of 15 km. It measures in the infrared region between 780 and 1 400 cm^{-1} and its long line-of-sight provides sufficient sensitivity to low ice concentrations. The analyzed data correspond to the Wave-driven ISentropic Exchange (WISE) campaign in September/October 2017 with base in Shannon, Ireland. In this thesis, the following questions were addressed:

- What are the macro-physical properties of cirrus clouds at mid-latitudes, i.e., cloud top and bottom height, vertical extent?

- Do clouds or even complete cloud layers appear above the tropopause? How frequently? In which meteorological situations?

- Is it possible to retrieve micro-physical properties of cirrus clouds from GLORIA, i.e., IWC and particle size?

- Can micro-physical models reproduce the formation of cirrus in the UTLS?

To answer these questions, the thesis is structured as follows. Chapter 2 gives the scientific background with an overview of the state of the art about cirrus clouds. Chapter 3 introduces the limb viewing geometry, GLORIA, the data processing, the WISE campaign

and the meteorological dataset. In Chapter 4, a detailed explanation of the development of the cloud identification methods for GLORIA is given. Chapter 5 includes the definition of the macro-physical properties of cirrus (cloud top height, cloud top bottom, vertical extent and position with respect to the tropopause) and their analysis. Chapter 6 describes the micro-physical properties (IWC and particle size) and explains the followed method to estimate them. In Chapter 7, two cloudy regions from the WISE campaign are selected and compared with the performance of the Chemical Lagrangian Model of the Stratosphere (CLaMS). Finally, Chapter 8 gives a summary of the results achieved in this thesis.

Chapter 2

Scientific and methodical background

This chapter introduces in the following pages concepts related to cirrus clouds that are relevant for the subsequent chapters. One such concepts are the formation mechanisms of cirrus clouds, which will be addressed in Chapter 7. In addition, a description of the radiative transfer theory, key for this study, and of the viewing geometry of GLORIA is given.

2.1 Earth's atmosphere: upper troposphere-lowermost stratosphere (UTLS)

The atmosphere is the gaseous shell that surrounds our planet. It is composed of 78 % nitrogen, 21 % oxygen, less than 1 % argon and other trace gases, such as water vapor, carbon dioxide or methane. The atmosphere makes life on Earth possible by maintaining an average temperature of about 15 ℃ (greenhouse effect) and absorbs a large part of the harmful ultraviolet (UV) radiation. Pressure and density in the atmosphere decrease nearly exponentially with height, while the temperature has a more complicated profile shape (Fig. 2.1). Following the thermal structure, the atmosphere is divided into five layers: troposphere, stratosphere, mesosphere, thermosphere and exosphere. Of inter-
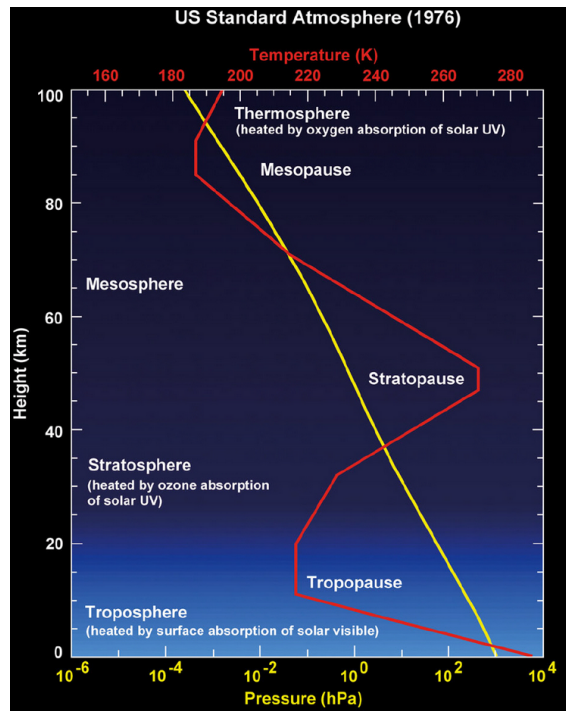
Figure 2.1: Layers of the atmosphere following its thermal structure. The red line indicates the temperature profile in K. The yellow line is the pressure profile in hPa. Credit European Space Agency

est for this study are the troposphere and the stratosphere. The troposphere extends from the surface up to 6–18 km, depending on the latitude and season. In this layer, the temperature decreases with height following an almost constant lapse rate:

$$\Gamma = \frac{\partial T}{\partial z} = \text{–6.5 K/km,} \tag{2.1}$$

with temperature T and altitude z. The troposphere is a turbulent layer that favours mixing of gases. In this first layer of the atmosphere, dynamical and chemical processes occur at different time and spatial scales and it is the layer were most of the weather phenomena take place. Some of these phenomena can be related to cloud formation, and depending on the meteorological situation, cirrus clouds will have different characteristics. For example, jet streams, Rossby waves, fronts or cyclones can be associated with cloud formation. Jet streams are strong narrow currents of wind (129 km h^{-1} to 225 km h^{-1}) that move eastwards with a width of several hundred kilometers, a vertical extent of less than 5 km and a length of several thousand kilometers. They are formed as a consequence

9

of the uneven atmospheric heating and the Coriolis force. Therefore, the air mass at the equatorward side of the jet stream is warmer than the air mass at the poleward side. In each hemisphere there are two mayor jet streams. The subtropical jet stream is located at $\approx 30°$, at an altitude between 10 km and 16 km. The polar jet stream, stronger than the subtropical one, is at 50° and at a lower altitude, between 9 km and 12 km. The jet streams have a meandering shape. Each of these meanders is known as a Rossby wave (or planetary wave) and is associated to high and low pressure systems, that occur at the sides of the jet stream. The breaking of Rossby waves is associated with the detachment of an air mass from the main air flow. Related to the extratropical cyclones is a poleward and upward air stream known as warm conveyor belt (WCB).

Located above the troposphere is a very stable layer, the stratosphere. It is stratified and has a positive lapse rate. The stratosphere is the layer where the ozone layer is located. Due to the absorption of the UV radiation, the temperature increases in this layer. Troposphere and stratosphere are separated by the tropopause. According to the World Meteorological Organization (WMO), the tropopause is defined as "the lowest level at which the lapse rate decreases to $2\,°C\,km^{-1}$ or less, provided also the average lapse rate between this level and all higher levels within 2 km does not exceed $2\,°C\,km^{-1}$" (WMO, 1957). The tropopause defined by this criteria is named thermal tropopause or lapse rate tropopause. There are also situations in which a second thermal tropopause can exist above the first. The WMO defines the second tropopause as follows: "If above the first tropopause the average lapse rate between any level and all higher levels within 1 km exceeds $3\,°C\,km^{-1}$, then a second tropopause is defined by the same criterion as under a) [definition of first tropopause]. This tropopause may be either within or above the 1 km layer." (WMO, 1957). The existence of a second tropopause is associated with enhanced transport between the upper tropospheric air of the tropics and the lowermost stratospheric air at higher latitudes above the subtropical jet. It occurs more often in winter and above a strong cyclonic circulation (Randel et al., 2007; Peevey et al., 2012). Double tropopause occurrences are also strongly linked to the storm track regions over the Atlantic and Pacific oceans (Peevey et al., 2014). Peevey et al. (2014) showed that during

the development of a baroclinic disturbance and the associated WCB, the formation of a double tropopause is the result of an expansion of the lower extratropical tropopause towards the equator. The existence of a second tropopause can also be associated with Rossby wave breaking events, although second tropopauses are frequently observed in their absence (Biondi et al., 2012). The variability of the thermodynamic structure of the tropopause, with events such as the existence of multiple tropopauses, could impact cirrus in the UTLS region affecting its vertical extent and optical thickness.

Another criteria used for the definition of the tropopause is the potential vorticity (PV). This quantity contains thermal (potential temperature) and thermodynamical (vorticity) information and is constant in absence of diabatic processes and frictional forces (Ertel, 1942; Schubert et al., 2004). The potential temperature θ is defined as the temperature that a parcel of air at pressure p and temperature T would have if it was compressed adiabatically to a standard pressure p_0 (usually $1\,000$ hPa):

$$\theta = T(\frac{p_0}{p})^{\frac{R}{c_p}}, \tag{2.2}$$

where R is the gas constant for dry air and c_p is the specific heat of dry air at a constant pressure (Wallace and Hobbs, 2006). Those surfaces with constant θ are called isentropes. It is useful to highlight the isentropes in plots such as cross-sectional views, because they are an indication for the vertical movements and the stability of the air masses. Vertical displacement upwards of the isentropes is an indication of air rising. On the contrary, if the isentropes move downwards, the air is sinking. The larger the separation between isentropes, the more unstable is the air mass. The vorticity is defined as the sum of the shear, i.e., the rate of change of the velocity in the direction transverse to the air flow, and the curvature, i.e., the rate of change of the direction of the flow in the downstream direction (Wallace and Hobbs, 2006).

Typically a constant PV of 2 PVU (1 PVU = 1×10^{-6} K m^2 kg^{-1} s^{-1}) is chosen for defining the dynamical tropopause (Holton et al., 1995). However, there are studies that suggest that a fixed value is not accurate for all latitudes and seasons (Kunz et al., 2009, 2011; Randel et al., 2007). Randel et al. (2007) used PV isolines between 1 and 4 PVU

to indicate the location of the dynamical tropopause and Kunz et al. (2009) deduced a mean PV of 4 PVU for all thermal tropopause heights during the SPURT campaigns.

The upper troposphere-lowermost stratosphere (UTLS) is the transition region between the well mixed troposphere and the stratified stratosphere. This thesis focuses on the extratropical UTLS (Ex-UTLS), defined as the region poleward of the subtropical jet between 8 – 20 km (Fig. 2.2) (Gettelman et al., 2011). The UTLS is a key region for the exchange and transport between the troposphere and the stratosphere. It exhibits complex chemical, dynamical and radiative characteristics. Even small changes in its composition lead to a strong impact in the radiative balance and the surface temperatures (Riese et al., 2012; Hossaini et al., 2015). Radiative active species, aerosols and cirrus clouds in the Ex-UTLS can have a strong radiative forcing (Tuck et al., 1997). The Ex-UTLS is affected by low and high pressure systems, fronts, WCB and other phenomena that affects the strength of the tropopause as a transport barrier (Gettelman et al., 2011), for example, cirrus clouds that will evaporate as soon as they experience a temperature increase, and thus modify the water vapor budget.
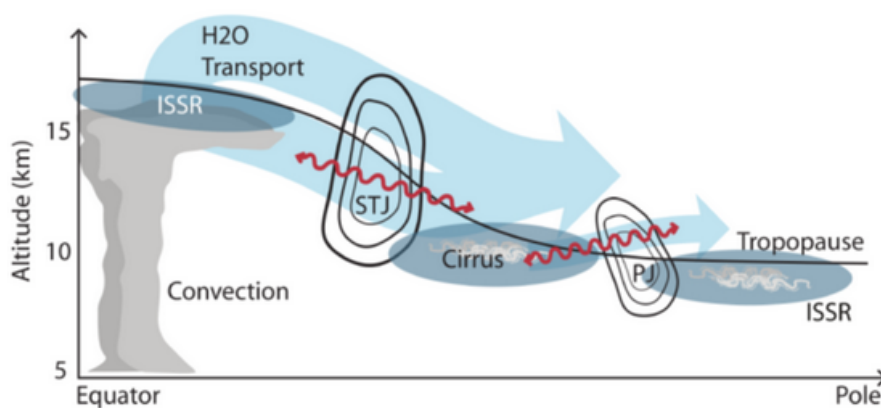
Figure 2.2: Illustration of the extratropical upper troposphere-lowermost stratosphere (Ex-UTLS). Subtropical (STJ) and polar jet stream (PJ). The black line represents the thermal tropopause. Clouds are marked in grey. The orange arrows indicate baroclinic waves. The light blue arrows represent the transport of water vapor and the dark blue shaded aereas, the region of ice supersaturation. Copyright: Martina Krämer and Christian Rolf.

2.2 Cirrus clouds: formation process

Clouds are formed by liquid water, ice crystals or a mix of both suspended in the atmosphere. Clouds form when masses of warm and humid air are lifted and cooled, reaching supersaturation [1]. Depending on their altitude, clouds are classified into three levels: low, middle and high. Clouds are further classified into ten main groups, called genera, depending on their dimension, shape, structure and color (Fig. 2.3). A further subdivision of the genera is made based on the shape and internal structure of the clouds. Additionally, cloud classification includes varieties, which refer to the degree of transparency of the cloud and to the different arrangements of its visible elements (World Meteorological Organization, last accessed: 28 April 2021). This thesis focuses on high level clouds: cirrus, cirrocumulus and cirrostratus (from now on simply referred as cirrus). Cirrus are located in the upper troposphere and in the region around the tropopause, therefore, their altitude range depends on the latitude. In polar regions, cirrus can be found between 3 km to 8 km, in mid-latitudes between 5 km to 13 km and in the tropical region between 6 km to 18 km. The average altitude of cirrus clouds is 9 km.

Cirrus clouds are composed entirely of ice crystals that form under temperatures lower than –38 °C. The formation process occur via homogeneous or heterogeneous ice nucleation. Homogeneous ice nucleation takes place at very high supersaturation, i.e relative humidity with respect to ice (RH_{ice}) between 140-170 % and at very low temperatures (< –38 °C) when supercooled aqueous solution droplets freeze (Krämer et al., 2009). These aqueous solutions are typically composed of sulfuric acid, sulfates or ammonium and their freezing threshold does not depend on their solutes. For the heterogeneous ice nucleation to occur, insoluble particles, called ice nuclei particles (INP), need to be present. INP are particles that favor the formation of ice, such as mineral dust, volcanic ash or coated soot. The freezing threshold depends on the type of INP, for example mineral dust and volcanic ash are very efficient INP, whereas coated soot is moderate. Heterogeneous ice nucleation occurs at RH_{ice} higher than 100 % and at temperatures that can be below –38 °C. Therefore, if supercooled solution droplets and INP are present, heterogeneous

---

[1]An air mass is supersaturated when the relative humidity (RH) is greater than 100 %.
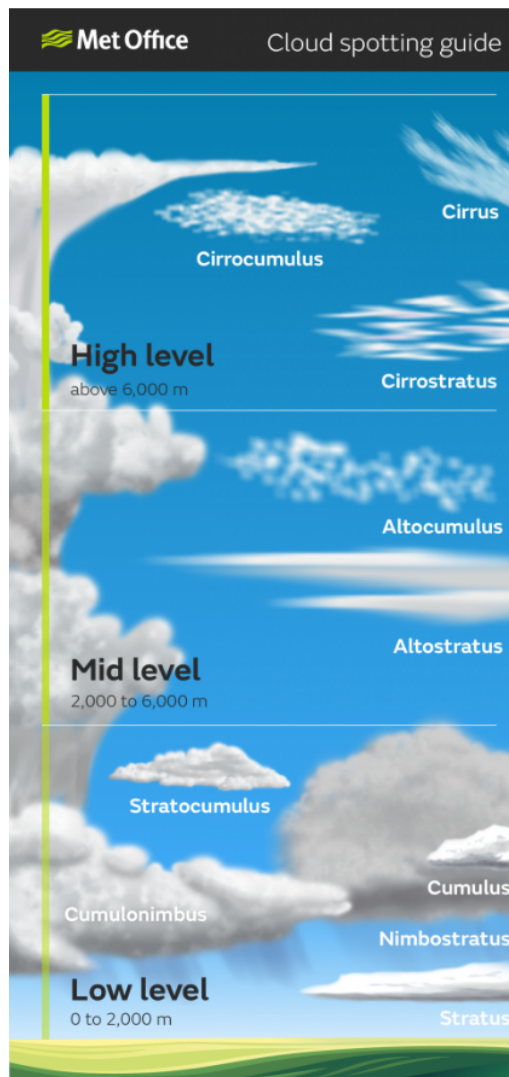
Figure 2.3: Classification scheme of clouds into three levels of altitude: low, middle and high. The classification includes ten main groups (genera) of clouds. Credit: Met Office.

ice nucleation will occur first. Once ice is formed, the ice crystals grow and the RH_{ice} decreases, as there is less water vapor available in the air parcel. When the ice crystals are too large, they sediment and fall to lower air parcels. If the temperature increases and RH_{ice} falls below 100 %, the ice crystals will sublimate.

A key parameter in defining the characteristics of the clouds is the motion of mesoscale waves. Since the micro-physical processes that determine the cloud properties are strongly linked to the temperature, even small temperature fluctuations can heavily impact the ice nucleation (Kärcher et al., 2014; Dinh et al., 2015). However, these processes are not well resolved in simulations and parametrizations are needed.

14

Cirrus clouds can be classified according to the origin of the ice crystals into liquid origin or in situ origin (Krämer et al., 2016; Luebke et al., 2016). Liquid origin clouds originate from mixed-phased clouds, i.e., clouds with both ice and liquid water, that are formed at temperatures above −38 °C and are lifted to altitudes with temperatures below the cirrus formation threshold. Since supercooled water droplets cannot persist at these low temperatures, they will spontaneously freeze. These clouds are optically thick and are characterized by high IWCs together with high ice crystal number concentration and large ice crystals (occasionally >100 μm). In situ origin cirrus are those that formed at temperatures below −38 °C via deposition of water vapour. Within in situ cirrus, two different types are possible: those originated in slow updrafts and those originated in fast updrafts. The ones from slow updrafts (up to $0.1\,\mathrm{m\,s^{-1}}$) are optically thin, characterized by low-middle IWCs together with low-middle ice crystal numbers and middle-to large ice crystals. For these cirrus, heterogeneous ice nucleation occurs first. If the conditions are adequate and there was not already homogeneous ice nucleation due to temperature fluctuations, then homogeneous ice nucleation can happen. Fast updraft cirrus are optically thick and are dominated by homogeneous ice nucleation, i.e., they are not affected by the properties of the INP. These fast updraft cirrus posses high IWC, high ice crystal numbers and small ice crystals. The formed cirrus have different characteristics, depending on the conditions of their origin. For example, in low and high pressure systems under slow updraft conditions, in situ cirrus are formed. At the jet stream, with fast updrafts, also in situ cirrus occur, whereas WCB are linked to liquid origin cirrus (Krämer et al., 2016, 2020).

15

2.3 Radiative transfer theory

Radiative transfer theory describes how the electromagnetic radiation propagates through a medium. This medium can be, for example, the atmosphere, where particles can absorb, emit or scatter radiation. How the atmosphere interacts with radiation depends on its gaseous composition and the characteristics of aerosols and clouds. The atmosphere is relatively transparent to the incoming solar radiation, which heats the surface of the Earth. To return this heat to the space and reach energy balance, the Earth emits thermal infrared (IR) radiation, which is efficiently absorbed and emitted by the atmosphere. The regions of the electromagnetic spectrum that are not heavily influenced by atmospheric absorption are the atmospheric windows, which are used by remote sensors to detect the presence of particles in the atmosphere.

Aerosols and cloud particles can both scatter and absorb radiation with different degrees of efficiency depending on their shape, radius, composition and wavelength of the incident radiation (Petty, 2006). Clouds scatter light in the IR band very efficiently. The scattering by clouds is a function of the real part of the refraction index [2] of water or ice, and the absorption of the imaginary part. As the features of ice and water cloud particles are different, depending on the incident wavelength, this difference is exploited by satellites to discriminate between ice and water cloud particles.

To describe the scattering properties of particles, it is useful to define a dimensionless number called the size parameter x

$$x = \frac{2\pi r}{\lambda},$$ (2.3)

where r is the particle radius and λ the wavelength of the incident radiation. Depending on the value of x, different scattering regimes are defined (Fig. 2.4). For this thesis the interesting wavelength is $12\,\mu$m, corresponding to a wavenumber of $833.4\,\text{cm}^{-1}$ in the thermal IR band. The particle radius of cirrus in mid-latitudes falls between $1\,\mu$m to $\approx 100\,\mu$m, according to the results of the ML-Cirrus campaign analyzed in Luebke et al.

---

[2]In optics the refraction index is a dimensionless number that describes how fast light travels through a medium.

(2016). Therefore, following Fig.2.4, the adequate regime is the Mie scattering, i.e., the size of the particles is comparable to the wavelength of the incident radiation.
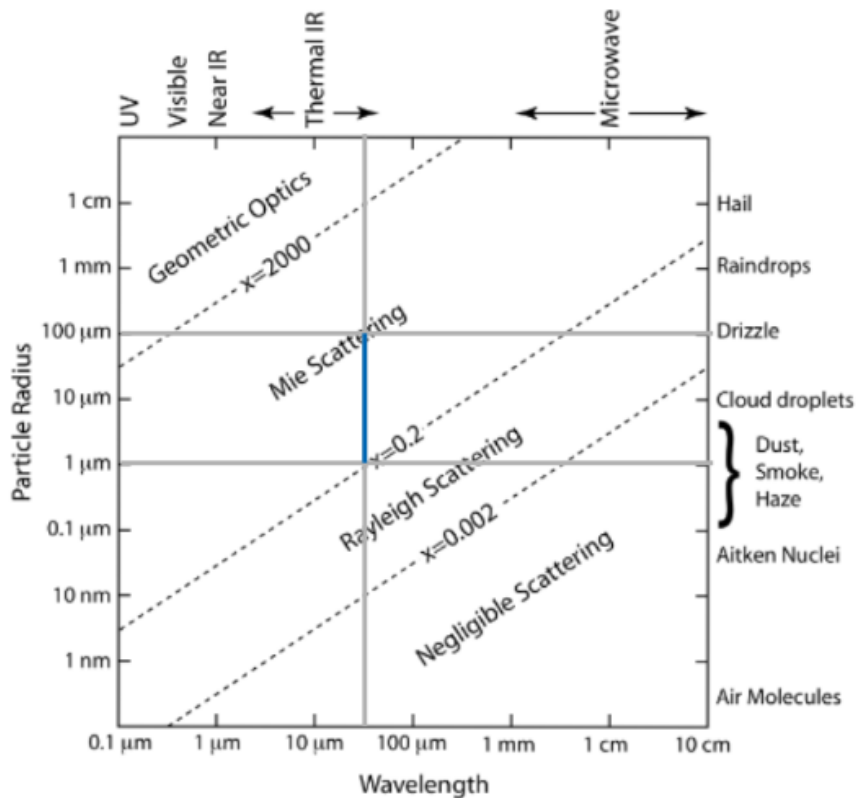

Figure 2.4: Scattering regimes depending on particle size and wavelength of the incident radiation. The blue line marks the area where the extinction retrieval is performed (833.4 cm^{-1}) and the range of particle radius for cirrus in mid-latitudes (Luebke et al., 2016). Figure adapted from Petty (2006).

A key parameter to understand how the radiation propagates in the atmosphere is the extinction coefficient (β_e). It describes the attenuation of radiation per unit length when passing through a medium. It is defined as the sum of the absorption and scattering of the incident beam by particles. Large values of β_e indicate quick attenuation and small β_e indicate that the medium is rather transparent to the radiation. β_e is proportional to the intensity of the incident radiation, to the efficiency of the particles to absorb or scatter and to their concentration.

To describe how the radiation propagates through a non-scattering atmosphere, the

Schwarzschild equation (wavenumber dependent) is defined:

$$dI = dI_\mathsf{abs} + dI_\mathsf{emit} = \beta_\mathsf{a}(B(T) - I)ds, \tag{2.4}$$

where I is the radiance (or intensity) and measures the energy of radiation, β_a is the absorption coefficient, $B(T)$ the Planck's function and s the coordinate in the direction of propagation. The Planck's function describes the radiation of a black body [3] and is given by:

$$B(T) = \frac{2h\nu^3c^2}{\exp\left(\frac{h\nu c}{kT}\right) - 1}, \tag{2.5}$$

where h is the Planck's constant, ν the wavenumber, c the speed of light, k the Boltzmann's constant and T the temperature.

In the presence of clouds and aerosols, radiation is also attenuated by scattering along the ray path. In this case, the Schwarzschild equation is transformed into:

$$dI = dI_\mathsf{ext} + dI_\mathsf{emit} + dI_\mathsf{scat} = -\beta_\mathsf{e}Ids + \beta_\mathsf{a}Bds + \frac{\beta_\mathsf{s}}{4\pi}\int_{4\pi} p(\hat{\Omega}', \hat{\Omega})I(\hat{\Omega}')d\omega', \tag{2.6}$$

where β_s is the scattering coefficient and $\hat{\Omega}$' represents any direction from which the scattered radiation can contribute in the direction of interest $\hat{\Omega}$. The incoming radiance I is weighted with the phase function $p(\hat{\Omega}',\hat{\Omega})$, which describes the likelihood of a photon of being scattered into the direction $\hat{\Omega}$.

The Schwarzschild equation can be solved with radiative transfer models that are able to simulate the radiance that is measured by remote sensing instruments. For it, the atmospheric state (i.e., pressure, temperature, background aerosols) and the path of the light beam through the atmosphere must be defined. Section 3.2 describes the radiative transfer model and the setup used for retrieving atmospheric variables from the measurements.

---

[3]Black body is an idealized surface that absorbs all incident radiation.

2.4   Limb sounding technique

To observe the atmosphere, different techniques are used. Measuring instruments can be in situ, when located at the same position as the region of study, or remote sensing, i.e., their position is different from the targeted area of observation. Remote sensors can be employed from the ground, balloons, aircrafts or satellites and are divided into passive and active systems. Passive systems measure the natural radiation emitted by the atmosphere, whereas the active systems first emit a signal and then detect the reflected radiation. According to their measuring geometry, remote sensors can be, for example, limb-viewing or nadir-viewing.

Limb-viewing remote sensors measure looking tangentially through the atmosphere towards the horizon. They offer several advantages that make them widely used in stratospheric research. As the sensor looks tangentially, the contribution of the Earth's surface is smaller than in the nadir-viewing instruments, where the viewing geometry is in the vertical direction. Therefore, there is less "contamination" coming from the surface in the measurements of the radiation. Due to the long ray path along the atmosphere in the limb geometry, called the line of sight (LOS), limb sensors posses high sensitivity even towards species with very low concentrations. They also offer high vertical resolution, but limited horizontal resolution. The LOS is not a perfect straight line due to the refraction in the atmosphere and when plotted in a reference system with the Earth's surface as a straight line, it adopts a parabolic form. The closest point of the LOS to the Earth's surface is the tangent point and its altitude is called the tangent altitude (Fig. 2.5). Each LOS is associated to its corresponding tangent altitude. The horizontal distance of each LOS, from the instrument to the tangent point, can extend several hundreds of kilometers, for some satellites even several thousands of kilometers. The lowest LOS is the one with the largest path through the atmosphere. The radiance measured by the limb instrument is integrated along each LOS and contains the information related to the presence of clouds.

Associated to each tangent point, there is a tangent layer. For each LOS, the ray path through the respective tangent layer is considerably long. This characteristic makes limb

sounders sensitive to changes of composition of the tangent layer. Considering a tangent altitude (TH) of 10 km, the thickness of the tangent layer (Δz) of 1 km and the Earth's radius (R_E) 6371 km, the length of the ray path (s) through the tangent layer is $\approx$ 226 km, according to equation 2.7:

$$s = 2\sqrt{(R_\mathsf{E} + TH + \Delta z)^2 - (R_\mathsf{E} + TH)^2} \tag{2.7}$$

With respect to the study of clouds, the limb geometry offers an important advantage. As the signal is integrated along the LOS, optically very thin clouds are easily visible to limb sounders, however this also results in losing knowledge of the exact position of the cloud (Fig. 2.5b). It also means that it is hard to differentiate between a patchy cloud, a thin cloud extended along the LOS or a small cloud but optically thick. Nevertheless, due to their high vertical resolution, limb sounders provide very valuable information regarding the vertical structure of the clouds, i.e, cloud top, cloud bottom and vertical extent. Kent et al. (1997) addressed the questions than can arise from using the limb technique and the assumptions done in the retrieval. To do so, they simulated Stratospheric Aerosol and Gas Experiment (SAGE II) cloud measurements and studied the uncertainty in the cloud top determination and possible error situations. The first error is that the true cloud might be located at a higher altitude than that of the tangent layer to which it is attributed. In the study of Kent et al. (1997) about 60 % of the simulations had no altitude error and under 40 % showed an error of 1 km or greater.
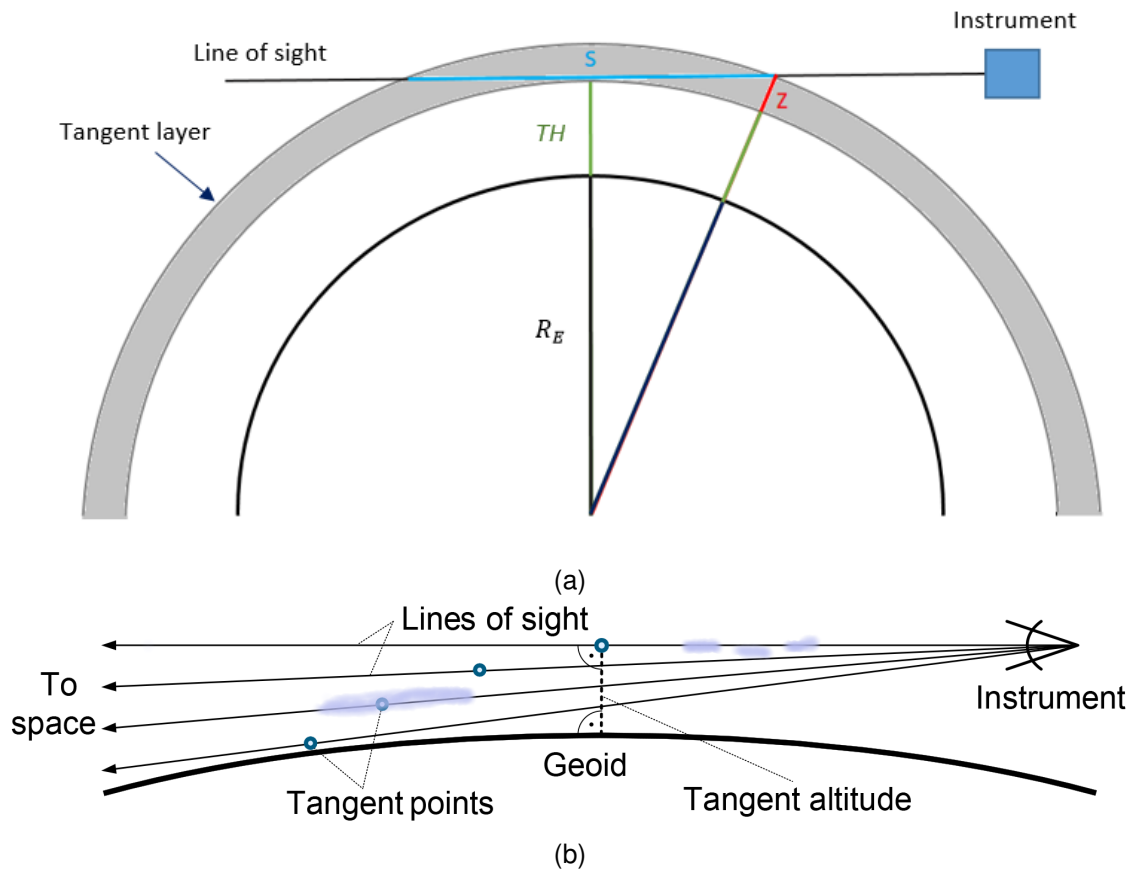
(a)

(b)

Figure 2.5: (a) Sketch of the ray path s (in blue) through the tangent layer (shade in grey). The tangent altitude (TH) is indicated in blue and the thickness of the tangent layer (z) in red. The Earth's radius is represented by the black line R_E. (b) Representation of the limb viewing geometry. The green dots indicate the tangent point of the LOS. The exact position of the clouds (in blue) along the LOS is not possible to determine. The radiance from all LOS is recorded simultaneously and integrated along each path. It contains the information related to the presence of clouds.

Chapter 3

Instrument and datasets

This chapter introduces the datasets employed in this thesis. The analyzed data come from observations, reanalysis data and model simulations. The observations were made by the GLORIA (Gimballed Limb Observer for Radiance Imaging of the Atmosphere) instrument during the WISE campaign (Wave-driven ISentropic Exchange). This campaign took place in Shannon, Ireland during September - October 2017 and covered an area from $37°$N to $76°$N and $57°$W to $12°$E. Necessary for the study was the computation of different meteorological variables, such as the tropopause height. With this purpose and also as input for the models, a meteorological reanalysis dataset from the ECMWF was selected. The employed models include microphysics of the clouds, computation of backward trajectories and radiative transfer theory.

GLORIA is described in Sect. 3.2, including technical characteristics, data processing and the extinction coefficient retrieval. Sec.3.1 introduces the WISE campaign and Sec.3.4 explains how the different parameters from the meteorological dataset were computed.

3.1 WISE campaign

The data analyzed in this study were measured during the WISE (Wave-driven ISentropic Exchange) campaign. It took place in Shannon, Ireland (52.70°N, 8.86°W) in September and October of 2017 and covered the North Atlantic area. With a total of fifteen scientific

flights (plus a first test flight) (Fig. 3.1), it aimed to answer questions related to mixing, the role of Rossby wave breaking events in the transport of trace gases such as water vapor, the formation of cirrus clouds and several other topics (Riese et al., 2017, last accessed: 13 August 2020). Information about the objectives of each scientific flight is found in Table 3.1.

Table 3.1: Scientific objectives of each flight of the WISE campaign.

Scientific flight	Objectives
F02: 13-09-2017	GLORIA tomography above jet and ridge, tracers
F03: 18-09-2017	Tropospheric air, probe edge structure
F04: 20-09-2017	Filamentary structure in subtropical anomaly
F05: 23-09-2017	Gravity waves, tropospheric intrusion, mixing
F06: 27-09-2017	Tracer gradients
F07: 28-09-2017	Tropospheric ridge, tropopause structure
F08: 01-10-2017	Air masses with different origin and age, mixing, thin cirrus
F09: 04-10-2017	Filaments, cirrus
F10: 07-10-2017	Rossby waves breaking
F11: 09-10-2017	Rossby waves breaking
F12: 12-10-2017	Warm conveyor belt outflow, tropopause inversion layer structures, occlusion
F13: 14-10-2017	Occlusion, mixing
F14: 15-10-2017	Warm conveyor belt outflow, Ophelia [1]
F15: 19-10-2017	Mixing
F16: 21-10-2017	Rossby waves breaking, mixing

All the measurements were taken onboard the German research aircraft HALO (High Altitude and Long Range Research Aircraft). HALO is based on a Gulfstream 550 aircraft

---

[1] During the WISE campaign, on the 16th of October, the hurricane Ophelia made landfall in Ireland in the form of an extratropical storm.
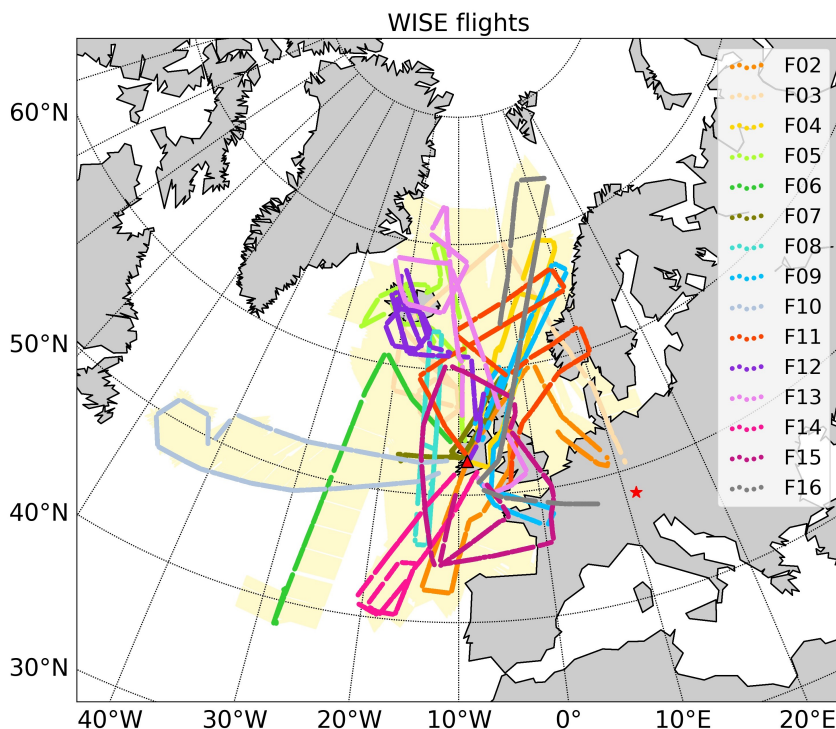
Figure 3.1: Overview of the 15 scientific flights of the WISE campaign. Color points correspond to the positions of HALO with GLORIA measurements. The red star indicates Oberpfaffenhofen, Germany and the red triangle Shannon, Ireland. The shade in light yellow gives a reference of the area covered by the measurements, indicating the distance of the tangent altitude point to the aircraft.

that was adapted for scientific purposes on atmospheric research. It has a maximum cruise altitude of 15.5 km, which due to the payload (maximum three tons) is usually not reached. During the WISE campaign the maximum flight altitude was 15 km, which means that the vertical coverage of GLORIA observations during this campaign ranged from ≈15 km down to ≈5 km. HALO has a maximum flight range that depends on the payload: for one ton payload the range is 10 500 km and for three tons, 8 800 km. Its maximum velocity is 0.088 5 Ma (1 084 km h^{-1}). The scientific payload for each campaign depends on the scientific objectives. For the WISE campaign a total of 13 instruments were installed, three remote-sensing and ten in situ instruments. The instruments can be placed in the cabin in special racks, in under-wing carriers or in the belly-pod, like GLORIA (Fig. 3.2). There are sample air inlets, radiation sensors, antennas and optical windows. More information about the payload is found in Table 3.2.

Figure 3.2: The German High Altitude and Long Range Research Aircraft (HALO) during the WISE campaign with GLORIA (red rectangle), mounted in the belly-pod and looking from the right side of the aircraft. Photo by Peter Preusse.

Table 3.2: Scientific instruments on board of HALO during the WISE campaign.

Instrument	Parameter
Remote sensing	
GLORIA-AB	Cirrus, temperature, H_2O, O_3, HNO_3, CCl_4, CFC-11, CFC-12, C_2H_2, C_2H_4, C_2H_6, HCOOH, HNO_3, . . .
WALES	H_2O, O_3, cirrus
Mini-Doas	H_2O (gas, liquid, solid phase), O_3, NO_2, HONO, CH_2O, IO, OIO, OClO, BrO, O_4
In-situ	
FISH	H_2O (total and gas phase)
HAI	H_2O (gas phase)
Dropsonde system (HALO DS)	Pressure, temperature, humidity and wind profiles
UMAQS	CO, N_2O, CO_2
FAIRO	O_3
AENEAS (IPA-NOY)	NO, NO_y
GhOST-MS (HALO GH)	SF_6, F12, C_2Cl_4, CFCs, Br source gases
AIMS	HCl, HNO_3, SO_2 or H_2O (total and gas phase)
HAGAR-V	CO_2, SF_6, CH_4, halons and NMHCs
BAHAMAS	Wind velocity, pressure, temperature, humidity, aircraft position, water vapor

25

3.2 Gimballed Limb Observer for Radiance Imaging of the Atmosphere (GLORIA)

GLORIA is part of the heritage of CRISTA-NF, which was a limb viewing airborne instrument with a vertical sampling of 200 m to 400 m and two spectrometers with spectral resolution of $\approx 2\,cm^{-1}$ and $\approx 1\,cm^{-1}$, respectively. This instrument represented an important stepping stone towards future remote sensing limb instruments with even higher vertical and horizontal resolution, which has been achieved with the development of GLORIA. The GLORIA instrument and the data processing chain has been described in previous studies (Kleinert et al., 2014; Friedl-Vallon et al., 2014; Riese et al., 2014; Ungermann et al., 2015).

GLORIA was designed for deployment on an aircraft with the purpose of providing information about trace gases and temperature fluctuations in the observational gap that comprises small-scale structures of less than 500 m of vertical extent and less than 100 km in the horizontal along the LOS. With GLORIA, it is possible to retrieve the distribution of different trace gases, to analyse the 3D structure of gravity waves and study clouds and aerosols in the UTLS (e.g. Ungermann et al., 2010, 2020; Blank, 2013; Krisch et al., 2018; Höpfner et al., 2019).

GLORIA is an infrared limb emission sounder that combines the Fourier-transform spectroscopy with a 2D infrared detector and measures radiance in the mid-infrared range ($780 - 1\,400$ cm^{-1}). Other components are a Michelson interferometer, a control unit, a gimbal frame to hold the instrument in the belly-pod of the aircraft, two black bodies used for calibration and a flight computer that serves as a communication unit (Fig. 3.3).

The high spatial resolution, 140×140 m (horizontal sampling $\times$ vertical sampling) at a tangent point altitude of 10 km and observer altitude of 15 km, and the high precision sensors to obtain a good pointing accuracy, make GLORIA an instrument well suited for investigating optically and vertically thin cirrus. The instrument is typically configured to use 48×128 pixels (horizontal $\times$ vertical) of its 2D detector array. GLORIA is able to produce 2D IR images that allow observing structures with an even smaller horizontal
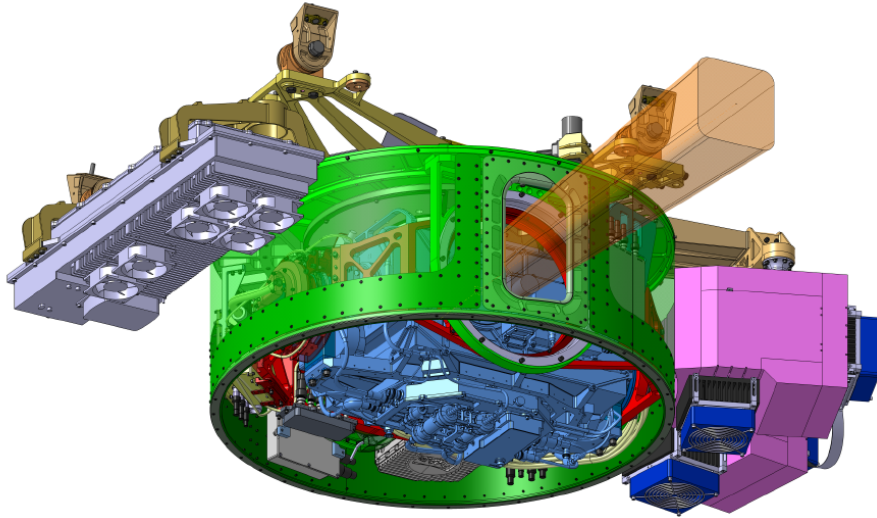
Figure 3.3: Sketch of GLORIA with its different components colored. The light gray indicates the power supply unit, pink the blackbodies, blue the pitch frame with the spectrometer, red the roll frame, green the yaw frame and gold the mounting frame to the aircraft. The field of vie of GLORIA is represented by the orange cone. Figure from Friedl-Vallon et al. (2014).

structure (Fig. 3.4). Although this option has not been explored in this study, it is considered for future work. The amount of radiance that each pixel of the detector receives is determined by the point spread function (PSF), which describes the response of an imaging system to a point source. The shape of the PSF is approximated by an Airy-disk with an aperture of $3.6\,\mathrm{cm}$ and using $830\,\mathrm{cm}^{-1}$ as a reference wavelength. This configuration was computed from a theoretical set-up of the instrument and was validated by cloud top measurements.

As the main focus of this thesis is the characterization of cirrus clouds close to the tropopause and thus the most important feature is the vertical resolution, each individual pixel is typically not analyzed, but the horizontally averaged spectrum (averaged over 48 pixels) of each row of the 2D array. The final result is one profile for each measured set of interferograms with 128 spectra, which for a tangent altitude of $10\,\mathrm{km}$ and observer altitude of typically $15\,\mathrm{km}$, means a vertical sampling of $140\,\mathrm{m}$ and a horizontal sampling of $6.7\,\mathrm{km}$. The vertical sampling is coarser the closer the tangent point altitude is to the observer altitude, as the projection of the PSF gets wider the further the tangent point is. For example, if the observer altitude is $14.7\,\mathrm{km}$, at the tangent point of $13\,\mathrm{km}$, the
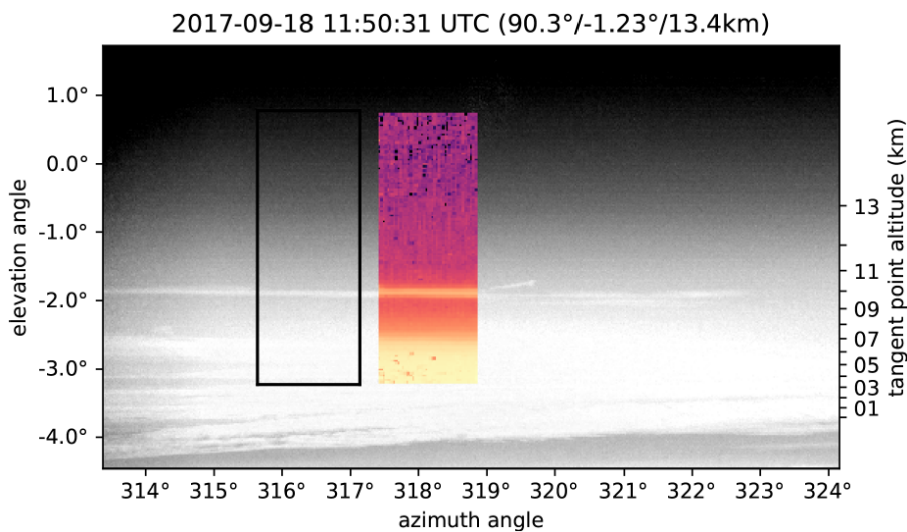
Figure 3.4: Single IR image from GLORIA of a cirrus cloud at 10.5 km overlapped with the corresponding image of the visible camera during the WISE flight on the 18-09-2017 at 11:50:31 UTC. The IR image is the averaged radiance over the spectral range 831.2 cm^{-1} to 835.0 cm^{-1} in logarithmic scale with arbitrary units. The black rectangle shows the original position of the IR image. Figure from Ungermann et al. (2020).

vertical sampling is about 88 km, at 10 km it is about 150 m and at 8 km it is about 179 m. GLORIA always points towards the horizon from the right side of the plane. It is typically configured to one of three measuring modes: one high spectral resolution mode called chemistry mode (CM) with a spectral sampling of 0.062 5 cm^{-1} and two modes, premier and panorama modes (DM) with a lower spectra sampling (0.625 cm^{-1}) and a focus on dynamical effects in the atmosphere. During CM, GLORIA has a fixed viewing direction of usually 90° with respect to the flight trajectory. During the premier and panorama mode, it changes its viewing direction between 45° and 135° in steps of 4° and 2°, respectively, which gives the possibility of observing the same volume of air from different perspectives and thus of performing tomographic studies. This capability of GLORIA was used for the 3D reconstruction of gravity waves (Krisch et al., 2018) and clouds (Ungermann et al., 2020). Table 3.3 summarizes the most important technical characteristics of GLORIA.

3.3 Data processing

The data processing chain of GLORIA consists of three stages: the raw data processing (level 0), the processing into geolocated calibrated spectra (level 1) and the retrieval

Table 3.3: Instrument specifications (Friedl-Vallon et al., 2014). Observer altitude of 15 km and tangent altitude of 10 km. * Ungermann et al. (2021)

Property	Value
Temporal sampling	2 s ($\approx$0.5 km) / 12.8 s ($\approx$3.2 km) for DM/CM
Spectral coverage	780 cm^{-1} to 1 400 cm^{-1}
Spectral sampling	0.062 5 cm^{-1} to 0.625 cm^{-1}
Detector array size	256 $\times$ 256 pixels
Used detector array size	48 $\times$ 128 pixels
Vertical sampling	0.031°, equal to 140 m
Horizontal sampling	0.031°, equal to 140 m
Vertical spatial coverage	-3.3° below horizon to 0.8° above horizon
Horizontal spatial coverage	1.5°(=48 $\times$ 0.031°) equal to 6.7 km
Yaw pointing range	45° to 135°
Pointing precision (vertical)	0.012°, equal to $\approx$50 m (1σ)
*Pointing accuracy	0.1°

of geophysical quantities using the fast radiative transfer model JURASSIC2 (Hoffmann et al., 2008; Griessbach et al., 2013; Ungermann et al., 2015). This work uses level 1 (radiance) and level 2 (extinction coefficient, temperature and pressure) products.

3.3.1 Level 1 data

As mentioned at the beginning of this section, two main components of GLORIA are the Michelson Interferometer, formed by two mirrors, one of them movable, and a beamsplitter and a 2D detector array. The light is divided into two beams at the beamsplitter and when they arrive at the detector they have been transmitted once and reflected twice. The detector registers a signal that is proportional to the incoming intensity. The electric output signal of the detector is divided in two terms, the DC and the AC. The DC term, or unmodulated component, can be removed because it has no spectrometric relevance. The AC term, or modulated component, contains information about the incoming light's frequency. These two terms form the interferogram or interference pattern. The level 0 processing resamples these interferograms on a space equidistant grid that are transformed into calibrated spectra, i.e., radiances, using the inverse Fourier transform (level 1 processing). Detailed information about the level 0 and level 1 processing can be found in Kleinert et al. (2014); Guggenmoser (2014). During the analysis of the WISE measure-

29

ments, parasitic images, i.e., abnormal low radiances, appeared above and under strong signals such as clouds. During some of the flights, the instrument was pointed into the direction of the Moon and these measurements were used to study the phenomenon of the parasitic images. It was discovered that the anomaly was negative above the Moon and positive below it (Fig. 3.5). However, these anomalies did not correspond to the typical parasitic images that affect the main image processed with a Michelson interferometer. Sha (2013) characterized the Imaging Fourier Transform Spectrometer GLORIA and reported the formation of parasitic images at the sides of the main image due to multiple reflections at the beamsplitter surface that contribute to the DC and AC part of the interferogram. GLORIA was further examined in the laboratory and the cause of the anomalies was discovered. The beamsplitter was defective causing reflections above and below in the reference laser signal.
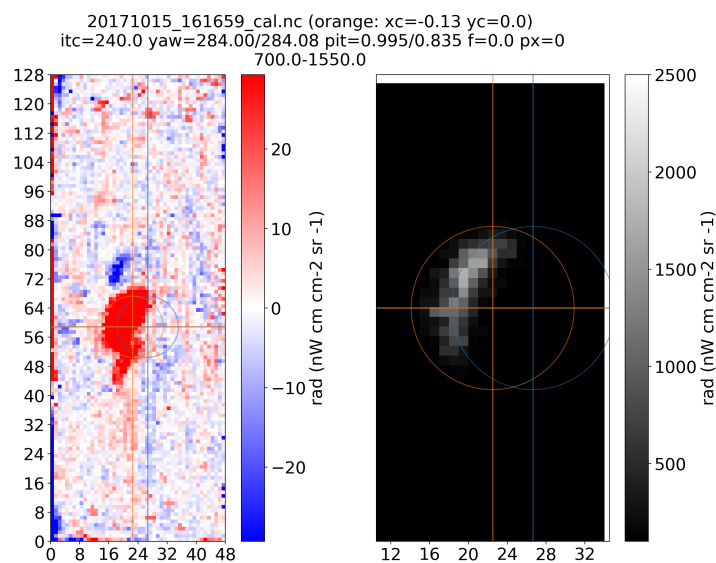

Figure 3.5: Moon measurement during flight 14 of the WISE campaign on the 15-10-2017. The image corresponds to the used area of the 2D detector array with 128 pixel rows and 48 pixel columns. On the left panel the radiance difference is plotted. Between rows 52 and 70 and columns 14 and 26 in bright red is the increased of radiance created by the Moon. Below it, between rows 44 and 58, the positive anomaly in red is seen. Above the Moon, between rows 70 and 80 in dark blue, the negative anomaly. The right panel corresponds to the measured radiance of the Moon.

To find a correction, calibrated spectra and detrended calibrated spectra of Moon

measurements for three flights were analyzed in detail covering the whole spectral range of GLORIA. Detrended means that only the atmospheric contribution is taken into account and not the instrument offset. As the Moon and clouds are very bright sources, the effect of the instrument offset is assumed to be small. For the negative signal besides the Moon measurements, cross-sections of the radiance in the microwindow $833.0 - 834.0$ cm^{-1} for all flights were used to obtain an adequate correction. After comparing the radiance of the anomalies with the radiance of a box with the same size in pixels as the anomalies, placed at their right and at their left, the spectral regions that were more affected by the negative parasitic image are:

- $770.0 - 1\,020.0$ cm^{-1} (effect of 15 nW cm cm^{-2} sr^{-1}),

- $1\,080.0 - 1\,300.0$ cm^{-1} (effect of 7 nW cm cm^{-2} sr^{-1}),

and for the positive parasitic image:

- $740.0 - 1\,020.0$ cm^{-1} (effect of 30 nW cm cm^{-2} sr^{-1}),

- $1\,060.0 - 1\,260.0$ cm^{-1} (effect of 14 nW cm cm^{-2} sr^{-1}),

In the microwindow $960.0 - 1\,020.0$ cm^{-1} and in the spectral regions $791.0 - 793.0$ cm^{-1}, $1\,225.0 - 1\,226.0$ cm^{-1} and $1\,406.0 - 1\,407.0$ cm^{-1} the anomalies were not clearly noticeable, which means that the effect was at noise level. When the original radiance was multiplied by a correction factor and shifted up (for the negative anomaly) or down (for the positive anomaly), the corresponding parasitic image disappeared (Fig. 3.6). The possible combinations were:

- Negative anomaly: shift of 13 or 14 pixels, multiplication factor of 0.016.

- Positive anomaly: shift of 13 or 14 pixels, multiplication factor of –0.028 or –0.025, respectively.

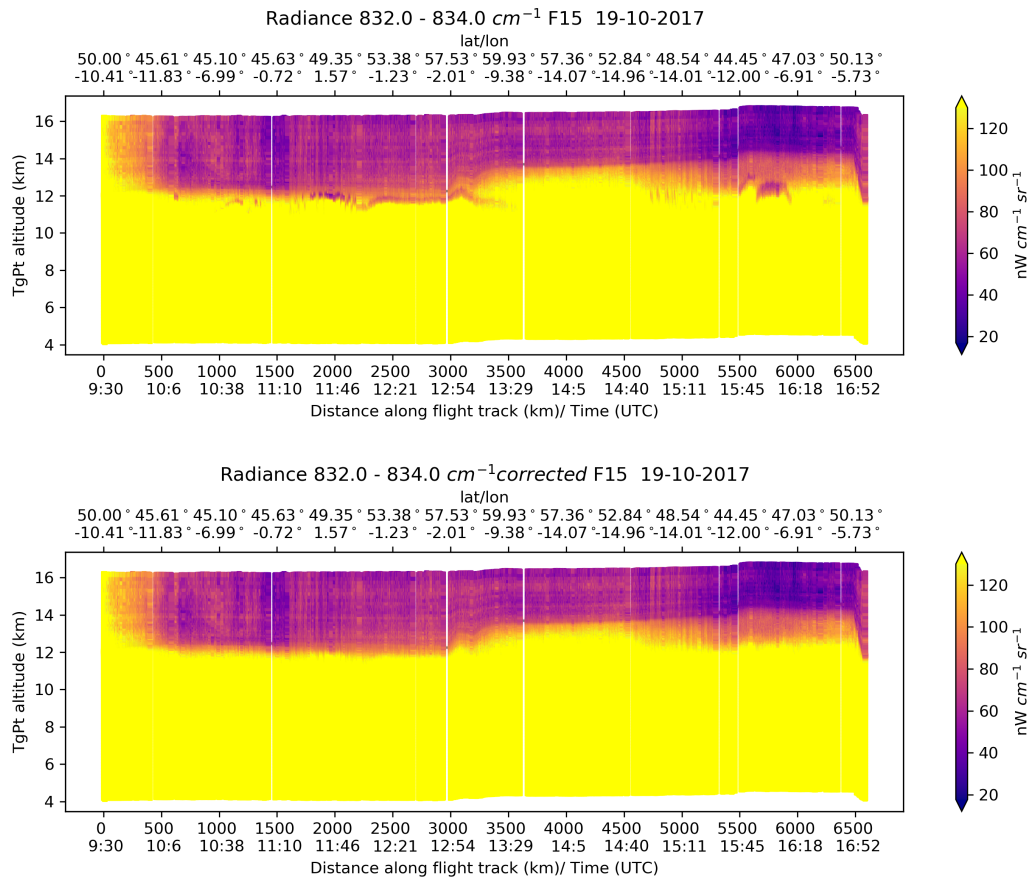The chosen combination for correcting the data was 13 pixels upwards and a multiplication factor of 0.016.

Figure 3.6: Cross-section of flight 15 with color code radiance in the microwindow 832.0 to 834.0 cm^{-1}. The color scale is saturated so the negative anomaly on top of the clouds is visible. The upper panel corresponds to the level 1 data with no correction applied. The negative anomalies are localized at 12 km between 500 to 3 500 km and 5 500 to 6 000 km. The lower panel corresponds to the level 1 data with the correction applied. The y-axis is the altitude of the tangent points in km, the lower x-axis is the time (UTC) and distance along the flight trajectory in km. The upper x-axis is the position of the aircraft in degrees of longitude and latitude.

3.3.2 Level 2 data

The level 2 processing corresponds to the retrieval of geophysical quantities, such as temperature, pressure, trace gases or the extinction coefficient using the fast radiative transfer model JUelich Rapid Spectral Simulation Code V2 (JURASSIC2) (Hoffmann et al., 2008; Griessbach et al., 2013) and the JUelich Tomographic Inversion Library (JU-TIL) (Ungermann et al., 2015). JURASSIC2 is a fast radiative transfer model developed at Forschungszentrum Jülich for analyzing the measurements of remote sensing instruments. It combines a forward model with retrieval techniques and allows to derive pressure, temperature and trace gases volume mixing ratios among others. Although scattering by cloud particles has an impact on the measured radiance (Höpfner and Emde, 2005), the simulation of radiative transfer was done without scattering. The reasoning for this is explained in Sect. 3.3.3.

The first step of the calculation is to do ray tracing, i.e., define the path through the atmosphere of each ray, known as pencil beam. For the simulations, the atmosphere is divided into homogeneous layers, through which the rays passes. The path of the pencil beam is not a straight line, due to refraction, and is divided in short cells, such that each cell can be considered homogeneous. Once the ray tracing is done, JURASSIC2 solves the Schwarzschild Equation (Petty, 2006; Wallace and Hobbs, 2006) in the mid-infrared region using spectrally averaged radiances, the Curtis-Godson Approximation (CGA; Curtis (1952); Godson (1953)) and Emissivity Growth Approximation (EGA; Weinreb and Neuendorffer (1973); Gordley and Russell (1981)) in combination with emissivity look up tables (Ungermann et al., 2011). The look up tables are typically computed by the line-by-line Reference Forward Model (Dudhia, 2017).

To retrieve geophysical quantities from the measured radiance, it is necessary to solve an inverse problem. This means finding an atmospheric state that fits the measurement. In the inverse problem, there is a state vector x describing the state of the atmosphere (quantities to be retrieved), a measurement vector (radiance from GLORIA) y with error ϵ, and a forward model F (JURASSIC2) implementing the physics of the involved

processes.

$$y = F(x) + \epsilon \tag{3.1}$$

JURASSIC2 simulates a certain atmospheric state according to a set of radiances and iteratively adjusts the simulated state until there is, within an expected error, agreement with the observed radiance. This inverse problem is ill-posed, therefore it has to be approximated by a well-posed problem using additional constraints (Tikhonov regularization).

The retrieval of the extinction coefficient is done for radiance in the atmospheric window $832.4 - 834.4\,\mathrm{cm}^{-1}$. The retrieval grid consists of a constant altitude grid with 81 levels ranging from 6 km to 16 km with a sampling distance of 125 m. The model includes corrections of the tangent altitudes due to the elevation angle offset and the refraction. Several tests comparing the radiance of a theoretical case of a cloud as a step function and the retrieved one have been performed to determine the influence of the radiance of cloudy pixels on the pixels above, i.e. the effect of the PSF (Fig. 3.7). The results show that the retrieved profiles are affected by the Gibbs phenomenon (Gibbs, 1899). The Gibbs phenomenon describes the behaviour of a Fourier series at a jump discontinuity, where an overshoot occurs and it does not disappear even if more terms are added to the Fourier sum. The overshoot, i.e. radiance larger than the maximum of the step function, is of of the order of 10 %. At the edges of the function and after the overshoot, ringing artifacts, i.e small oscillations, appear. These effects can cause an error in the determination of the cloud top height of one grid point (± 125 m). These oscillations could also affect the determination of the cloud bottom, creating a false detection of a thin layer ($1 - 2$ grid points) above a thick cloud in ≈ 1 % of all the cloudy profiles. The leading error term in the determination of the cloud top altitude is the pointing knowledge along the LOS. This error is about a tenth of a degree, which was validated by measurements of the Moon during several flights (Ungermann et al., 2021). Other sources of error are: precision, offset, gain, elevation, temperature, the error in the forward model and background aerosols. As can be seen in Fig. 3.8, there is a difference between clear sky and clouds (between 9 and 11 km). In the clear sky, the leading cause of error is the preci-

sion. For the clouds, the main contribution to the error in the position of the cloud top is the elevation, whereas for the magnitude of the extinction is the temperature and gain. The temperature contributes approximately a 3 % and the gain about 1 %.
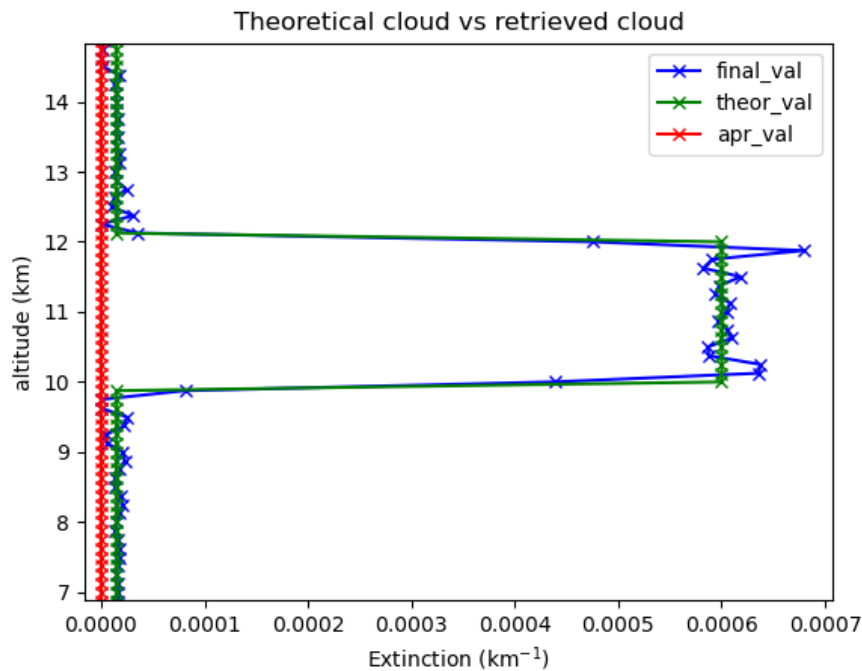

Figure 3.7: Test case of an extinction profile of a modelled cloud affected by ringing artifacts and Gibbs oscillations. In green is the extinction profile of a step function that represents the theoretical case. In blue, the retrieved extinction profile and in red the background aerosols.

The range of retrievable cloud extinction from the WISE measurements is from about 2×10^{-4} to 4×10^{-2} km^{-1} and allows the detection of optically thin cirrus, one of the objectives of this study. The upper limit is determined by the optical thick conditions in the limb direction and the lower limit by background aerosol and calibration uncertainties.
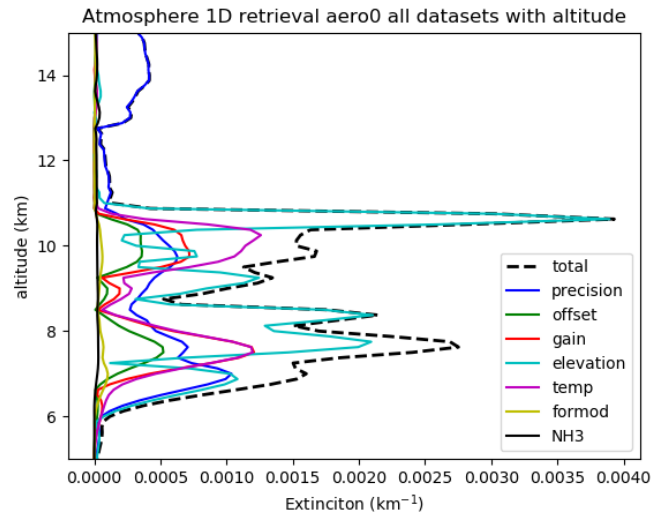
(a) Error sources
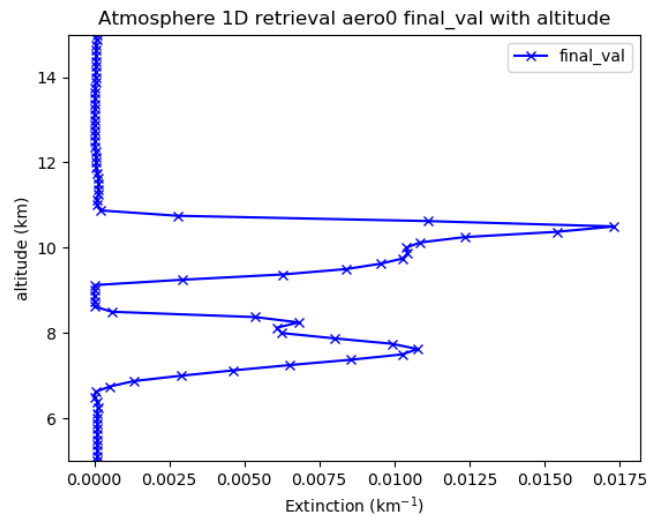
(b) Extinction profile

Figure 3.8: (a) Error sources and contributions to the extinction retrieval for one profile of flight 3. The black dashed line corresponds to the sum of all errors. The blue line indicates the precision; the green line, the instrument offset; the red line, the gain; the cyan line, the elevation; the purple line, the temperature; the yellow line, the error in the forward model and the black, the background. (b) Corresponding extinction retrieval profile.

3.3.3 No scattering vs. single scattering

This section presents the test cases of two flights for which single scattering was included and justifies the decision of performing the retrievals without scattering.

As introduced in Sect. 2.3, clouds can absorb and scatter radiation with different degrees of efficiency. Scattering can be modeled as single scattering, i.e., only one single scattering event is taken into account, or multiple scattering, i.e., the incident radiation is redirected several times in different directions. As explained by Höpfner and Emde (2005) the difference between zero scattering and multiple scattering for a case that falls between the two cases presented in their study (one with strong absorption and one with strong scattering), would be between 25-28 %, in terms of radiance. For investigating the impact in the extinction of neglecting scattering, retrievals with single scattering for two flights using the radiative transfer model JURASSIC2 were performed. The motivation to use single scattering instead of multiple scattering, which would be closer to reality, had computational reasons, as multiple scattering requires much more computation time. During the selected flights, both thin cirrus and thick cirrus were observed, and therefore, constitute an interesting case for studying the influence of scattering under different conditions.

The tests were prepared as follows. Homogeneous spherical particles were assumed, which allowed the use of Mie calculations, highly simplifying the calculation. Even though ice crystals are present in complex habits (which are not spherical), the approximation by spheres is valid as long as the effective size of the particle is less than 30 µm (Baran et al., 2003). The particle size was described with a log-normal distribution [2] with a width of 1.4 µm and a median radius of 8 µm. For the refractive index of ice, the values of Toon et al. (1994) at 163 K for the infrared range were selected. To conserve computation time, instead of processing all profiles, only a short section was selected while maintaining the same high vertical resolution of 125 m. Figure 3.9a is an example of such extinction profiles. The difference (calculated as the mean of the median difference of both flights) between the extinction neglecting scattering and the extinction including single scattering

---

[2] A log-normal distribution is a continuous probability distribution whose logarithm is normally distributed. It is described by the width σ and the median μ.

is 21 %, with 73 % as the percentile 95 and -86 % as the percentile 5. The mean difference at 2σ, i.e., percentile 16 and percentile 84 is -4 % and 49 %, respectively. This overestimation of the extinction, which is larger for larger extinction values (Fig. 3.9b), has a negligible impact in the determination of the macro-physical properties of clouds, like cloud top or bottom height (Sect.4). For the retrievals with single scattering, the cloud top was computed following the same procedure as for the retrievals with no scattering. For 98 % of all cases, both retrievals detected a cloud. Out of this 98 % about 71 % had the same cloud top height in both retrievals. The mean difference between cloud tops was 0 m with a standard deviation of 229 m. Following the same procedure for the cloud bottom, for 90 % of all cases, both retrievals detected a cloud bottom, obtaining the same altitude in 58 % of the coincidental profiles. The mean difference between cloud bottoms was 0 m with a standard deviation of 465 m.

3.4 Meteorological dataset

The high resolution ERA5 dataset provided by the European Centre for Medium-Range Weather Forecasts (ECMWF) was used for comparison and computation of meteorological variables. ERA5 stands for ECMWF reanalysis 5th generation and is available at 31 km horizontal resolution at 137 levels from surface to 80 km (Hersbach et al., 2020). The ERA5 dataset provides hourly data for a large variety of meteorological and climate variables. To perform the comparison between the reanalysis dataset and measurements, the variables of interest were sampled according to the GLORIA measuring geometry, as shown in Fig. 3.10. This figure represents the limb geometry during one measurement. The altitude range is limited from 5 km to 20 km.

For each LOS, every 30 km, the longitude, latitude and altitude of the corresponding point was calculated. Then, the meteorological variables were computed from the corresponding parameters of the ERA5 dataset (temperature, pressure, specific humidity), i.e. first thermal tropopause (TP), equivalent latitude (Eqlat) and ice water content (IWC), i.e. the cloud ice mass in unit volume of atmospheric air. The procedure was done without interpolation, simply selecting the closest ERA5 profile, and within the profile, the point

with the closest altitude. As the signal is integrated along the LOS of the instrument, the same applies for the IWC, thus the final parameter used for the comparison was the limb ice water path (IWP), i.e. the IWC integrated along the LOS (Spang et al., 2015). In addition, the potential vorticity (PV) and equivalent latitudes from the ERA5 data at the tangent point are retrieved.

To analyze the stability of the atmosphere, the static stability (N^2) was computed from GLORIA temperature and pressure retrievals (Sect. 3.3.2). The static stability is the square of the Brunt-Vaisala frequency (N), defined as:

$$N = \sqrt{\frac{g}{\theta}\frac{\partial \theta}{\partial z}}, \tag{3.2}$$

where g is the local acceleration of gravity, θ is the potential temperature, and z is the altitude of the air parcel. N^2 describes the vertical temperature stratification of the atmosphere and gives an insight of if an air parcel is in a transition region between the troposphere, characterized by low N^2 ($N^2 \approx 1 \times 10^{-4}\,\text{s}^{-2}$) and the stratosphere, characterized by high N^2 ($N^2 \approx 5 \times 10^{-4}\,\text{s}^{-2}$) (Grise et al., 2010). The potential temperature product needed for the computation of N^2 was computed from pressure and temperature of the final dataset, which contains the retrieval results and a priory information taken from ECMWF. The results are dominated by the a priori in regions, where no measurements are available, i.e., in or below thick clouds.
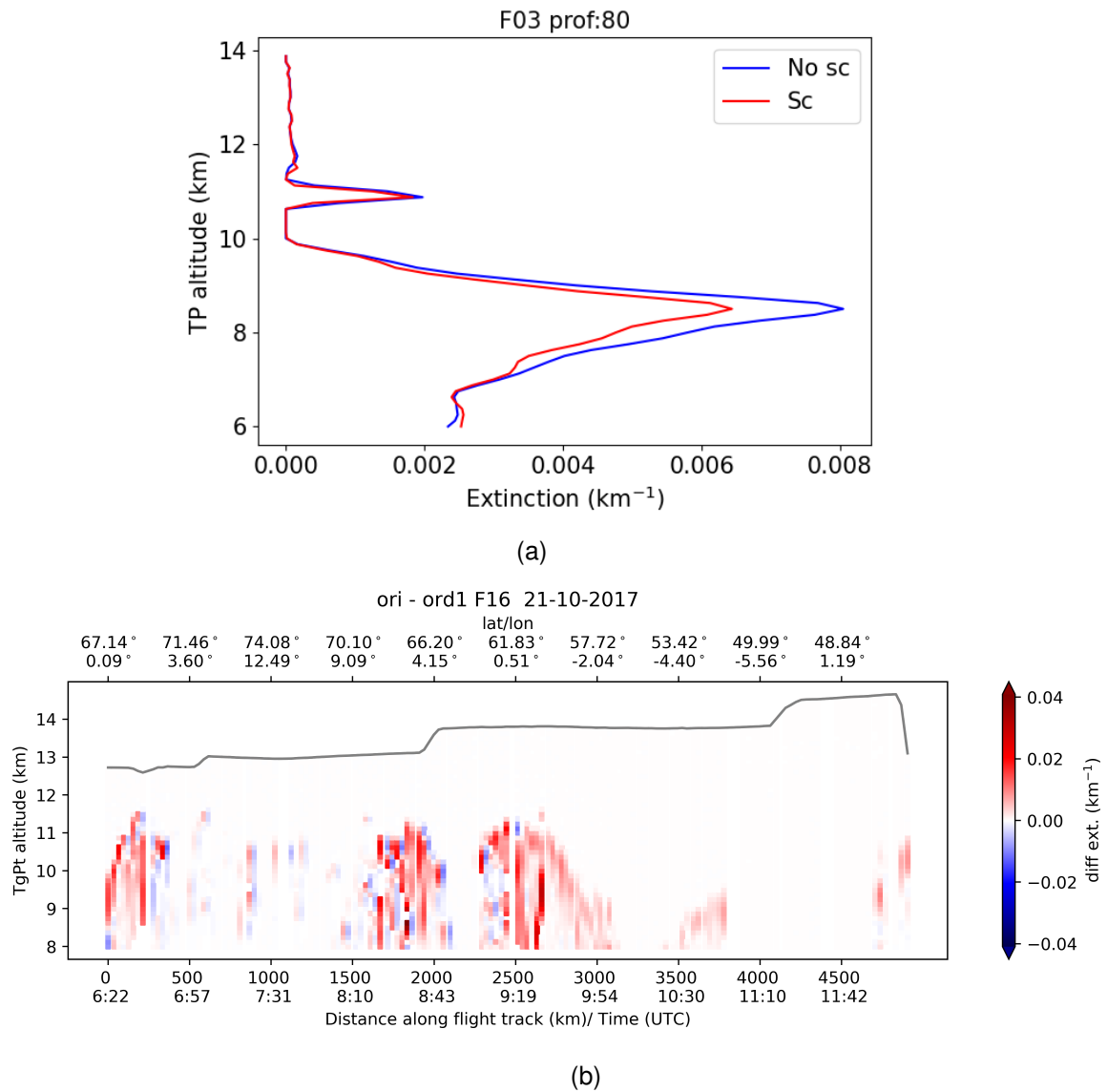
(a)

(b)

Figure 3.9: (a) Example of an extinction profile without scattering (in blue) and the same profile with single scattering (in red). (b) Cross-section for flight 16 with the difference between extinction with no scattering and extinction with single scattering. Red colors indicate an overestimation of the extinction, while blue colors and underestimation. The y-axis is the altitude of the tangent points in km, the lower x-axis is the time (UTC) and distance along the flight trajectory in km. The upper x-axis is the position of the aircraft in degrees of longitude and latitude. Each vertical column of the cross-section corresponds to the difference between extinction profiles of both retrievals.
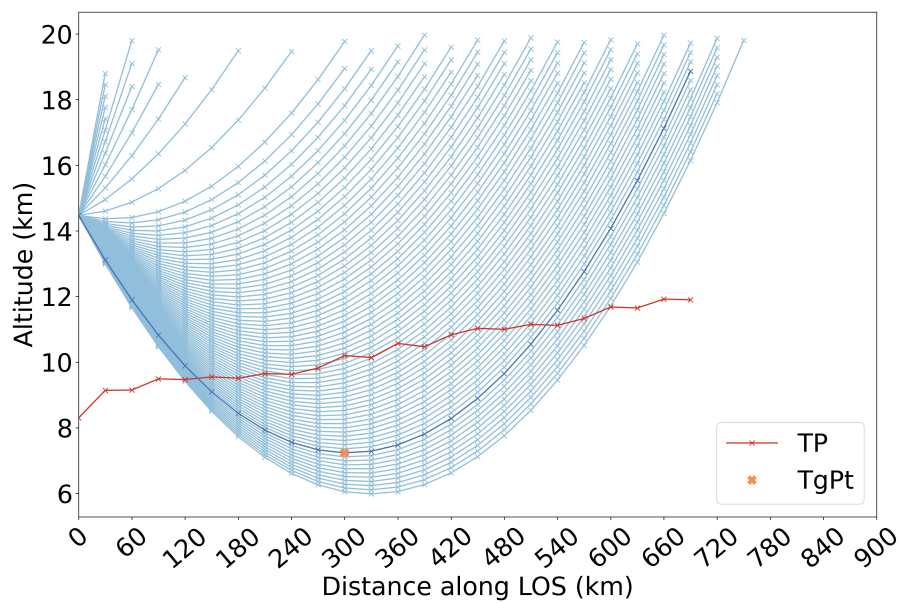
Figure 3.10: Example of the measuring geometry of GLORIA for one measuring time in a Cartesian system with the Earth's surface as a straight line. Each light blue line represents a different LOS that corresponds to a different tangent altitude. The red line is the tropopause (TP) calculated from the corresponding ERA5 variables along the corresponding LOS, in dark blue. The tangent point (TgPt) of the LOS is marked by the orange cross.

Chapter 4

Cloud detection

This chapter describes the employed cloud detection methods to analyze the data obtained with GLORIA during the WISE campaign. The first one is the cloud index, introduced in Sect. 4.1 and the second one makes use of the retrieved extinction coefficient, presented in Sect. 3.3.2. Section 4.2 explains the procedure to define the identification threshold for both methods and Sect. 4.3 analyzes the presence of aerosols in the measurements. Due to the presence of numerous aerosol particles in the atmosphere, which could affect the cloud detection, it is important to determine whether aerosols are present or not. To do so, the methods developed by Griessbach et al. (2014) and Griessbach et al. (2016) were applied.

4.1 Cloud index

The cloud index (CI) was first introduced by Spang et al. (2001) and has been widely used in different studies for the analysis of clouds in the UTLS and polar stratospheric clouds observed by CRISTA and MIPAS (Spang et al., 2001; Sembhi et al., 2012; Spang et al., 2015, 2016). The CI is a dimensionless number defined as the ratio between the mean radiance of two microwindows:

$$CI = \frac{\bar{I}[788.2 - 796.2]\mathrm{cm}^{-1}}{\bar{I}[832.4 - 834.4]\mathrm{cm}^{-1}} \tag{4.1}$$

The first spectral window is mainly dominated by emissions of a CO_2 Q-branch and the second is an atmospheric window region. The CI is affected by the water vapor continuum contribution to the atmospheric window at low altitudes and depends slightly on latitude and season (Spang et al., 2012; Sembhi et al., 2012). When clouds are present, the emission in both microwindows increases. However, the relative increase in the CO_2 Q-branch is smaller. As a result, the ratio decreases, therefore low values of CI indicate cloudy conditions. Typically, a CI between ~ 1.1 and 4 indicates the presence of clouds (Spang et al., 2008, 2015) and lower numbers indicate saturation. Figure 4.1 illustrates the limb radiance spectra in the region $750\,cm^{-1}$ to $1\,450\,cm^{-1}$ of a thin cirrus, a thick cirrus and clear sky at the same tangent altitude (11.3 km) from three different vertical profiles. For the thick cirrus spectra, the enhanced radiation at both microwindows is evident, causing a low CI (1.2). Such enhancement is not so pronounce for the thin cirrus, having a higher CI (2.9) and it does not occur for the clear sky (CI=10). The CI is a robust
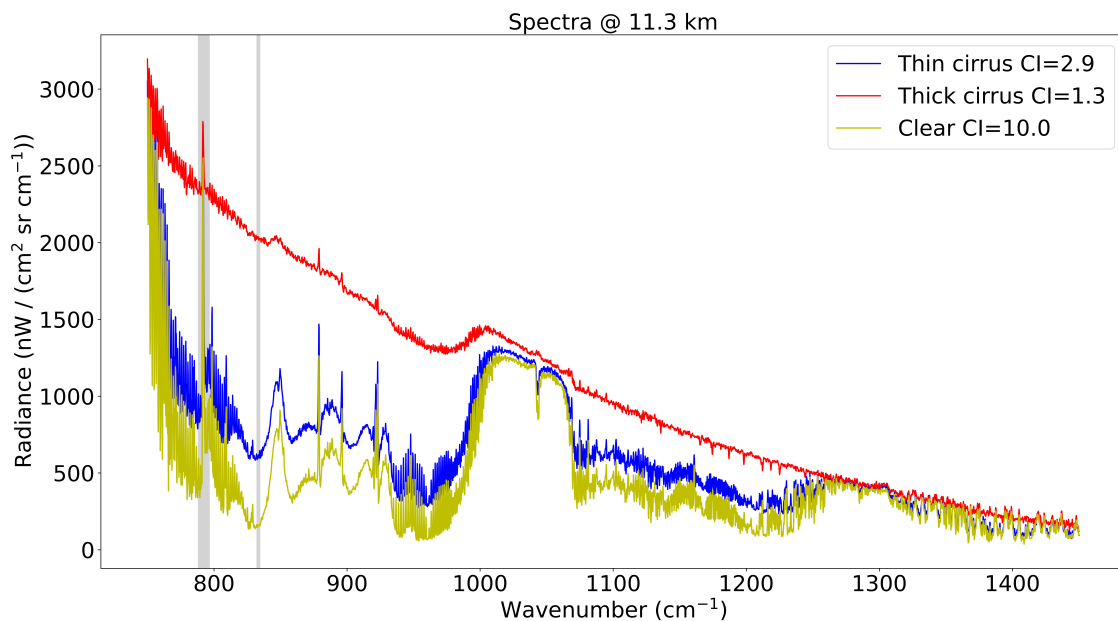

Figure 4.1: Limb radiance spectra corresponding to a thin cirrus (blue line), thick cirrus (red line) and clear sky (yellow line) with their corresponding cloud index (CI). All spectra are referred to a tangent altitude of 11.3 km from three vertical profiles of flight 16. The vertical grey bars indicate the two microwindows used in the definition of the CI.

method for the detection of cloud tops with very low computational costs, compared to the extinction retrieval. It is limited to the cloud top region for optically thick conditions. At the

tangent point below the cloud top, the CI is affected by the effects of cloudy layers above the radiance of the actual tangent height layer. To compare the CI and the extinction (Sect.3.3.2) cloud detection capabilities, the CI has been sampled at the retrieval grid (note that the radiance was averaged over the horizontal pixels). As a result, for each flight there are vertical profiles of CI and extinction as shown in Fig. 4.2. This figure shows a clear sky profile, a layer and an optically thick cirrus. For the optically thick conditions, the CI and the extinction behave differently. The CI profile saturates an stays at that CI value. The extinction profile reaches a maximum and then, since the instrument cannot observed deep into the optically thick cloud, the model fits the radiances but with no physical meaning. Another option to visualize these vertical profiles, adding information about the location or the measuring time, is in the form of cross-sections, where each column corresponds to a single profile of CI or extinction. Figure 4.3 shows an example of an extinction and CI cross-section for flight 3 restricted to altitudes below the flight path. The white areas in both cross-sections correspond to a first filtering of optically thicker regions (CI < 2).The radiative transfer model assumes for practical reasons a horizontal homogeneous atmosphere. As such, it assumes that simulated measurement rays diving below a cloud layer pass through the cloud twice, whereas in the actual situation it may 'miss' the cloud above on both occasions; if this occurs, the retrieval assigns nonphysical low extinction close to 0 to those regions (Fig. 4.3a, e.g. at 11:29 UTC, 11 km to 12 km). Above the clouds (125 m to 250 m), the low extinction values are due to the second order regularization that smooths the profiles and causes Gibbs oscillations in the extinction profile at strong extinction changes. For the CI cross-section (Fig. 4.3b), depending on the altitude, different CI threshold values indicate the presence of clouds. A detailed explanation about the detection threshold is found in the following section.
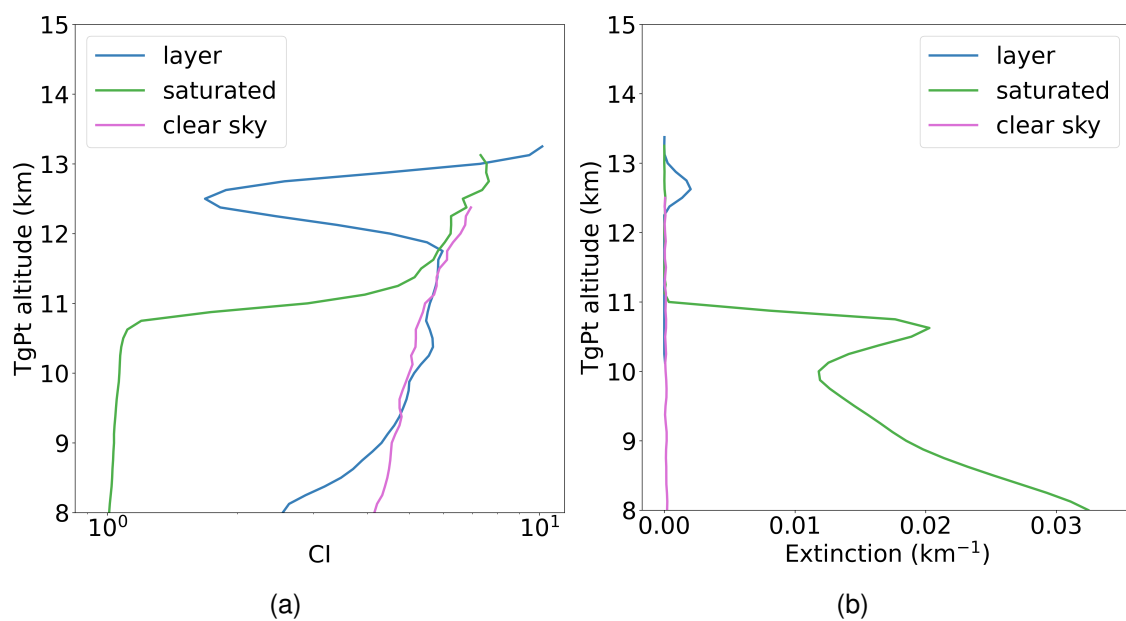
Figure 4.2: (a) Vertical profile of CI for three different measuring times. (b) Vertical profile of extinction for the same three measuring times as for (a). The blue line represents a cirrus layer, the green line a saturated profile, i.e an optically thick cirrus and the purple line indicates clear sky. The y-axis is the altitude of the tangent points in km. For each profile, the maximum altitude depends on the flight level.
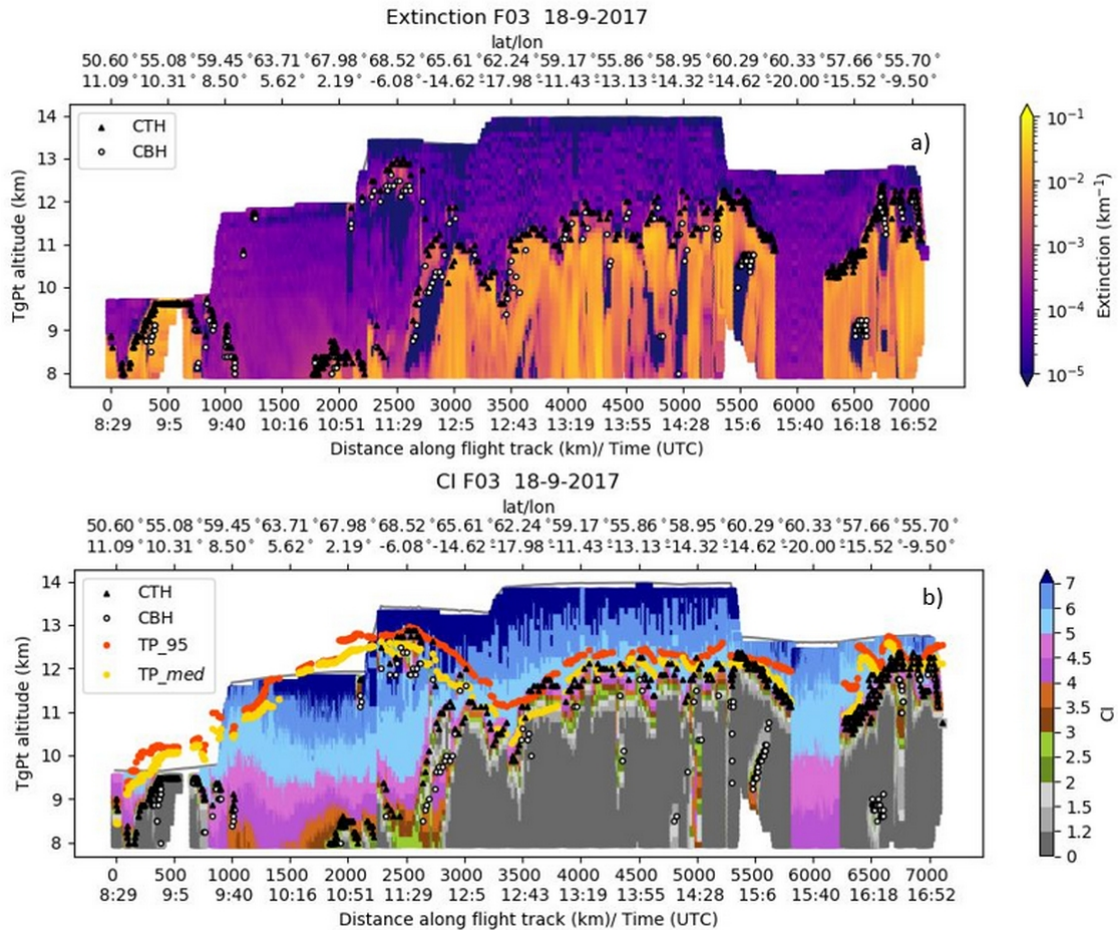
Figure 4.3: Cross-sections of extinction (a) and cloud index (b) for flight 3 of the WISE campaign. The results are restricted to levels below flight path. (a) Color code for extinction in km-1. Orange-pink colors indicate the presence of clouds; (b) color code for CI. Depending on the altitude, CI below 2 to 5 (colors from grey to pink) indicate the presence of clouds. Median tropopause (TPmed) and the percentile 95 of the tropopause (TP95) are represented with orange and yellow circles, respectively. Detailed information about TPmed and TP95 is given in Sect. 5.3. Cloud top height (CTH) and cloud bottom height (CBH) are represented with a black triangle and with a white circle, respectively. The altitude of the tangent points (TgPt) is the y-axis. The white areas in both cross-sections correspond to a first filtering of optically thicker regions (CI < 2). These areas correspond to the tangent layers where the clouds are optically too thick.

46

4.2 Derived detection thresholds for CI and extinction

To identify clouds in the WISE measurements, a detection threshold for CI and for extinction was defined. First, clear sky regions were selected. As a first approximation of clear sky conditions, profiles with CI always greater than 2 and extinction always less than 1×10^{-3} km^{-1} were selected. From this first coarse pre-selection, the vertical extinction gradient (Fig. 4.4) was computed to have an automated method that is more sensitive to optically thin clouds. If this gradient has a small variability, that means there are no elements, i.e., aerosols or cloud particles, that cause a sudden increase in the extinction and therefore a large gradient. Clear sky profiles were defined to be those with an extinction gradient lower than a threshold defined as the median extinction gradient of the pre-selected profiles of all flights together plus 5σ. 5σ was chosen after a visual fit to the gradient to reduce the number of false detections to a minimum. It is possible that the aircraft flies inside a cloud, which causes the vertical gradient of the extinction to be approximately constant and thus considered as clear sky. To exclude these cases, the condition that the CI must always be greater than 2 was added. Below 8 km, the extinction gradient increases, which indicates the influence of the water vapor continuum at low altitudes (Fig. 4.4). Therefore, the analysis was limited to the range from 8 km to the aircraft altitude.

For all the clear sky profiles, probability density functions (PDFs) of CI and extinction were calculated and normalized for each altitude bin. Using the PDF for guidance, a threshold for each parameter was defined. The extinction coefficient threshold (k_{thres}) was defined as the median of the extinction plus 5σ. This threshold is sensitive to structures with very low extinction, down to 2×10^{-4} km^{-1} for a tangent point between $\sim$11.5 km and 15 km (Fig. 4.5a, b). This detection limit is similar to the one estimated by Sembhi et al. (2012) for the Michelson Interferometer for Passive Atmospheric Sounding (MIPAS), with an extinction detection limit above 13 km of 1×10^{-4} km^{-1} and to the findings of Griessbach et al. (2020), specified in Table 1 of the cited study. The CI threshold (CI$_{\mathrm{thres}}$) is the percentile 1 (%) shifted by 0.3 (CI). Above 12 km a constant CI of 5 was applied because there, the low number of observations and occurrences of clear sky shifts the
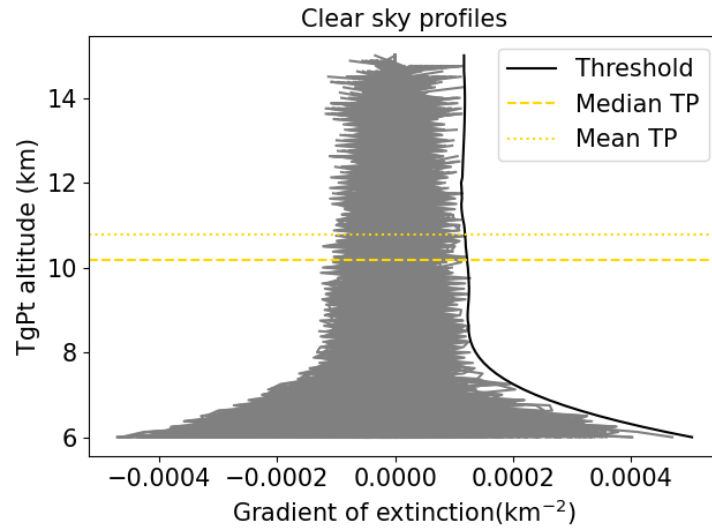
Figure 4.4: Vertical gradient of the extinction coefficient in the case of clear sky conditions. In black, the threshold defined as the median of the extinction gradient plus 5σ. Altitude of the tangent points (TgPt) in the y-axis. The median tropopause height (Median TP) and the mean tropopause (Mean TP) height of all clear profiles is indicated by a dashed and point yellow line, respectively.

threshold towards too high CI numbers. This threshold for this and lower altitudes agrees with the one defined by Sembhi et al. (2012) for northern mid-latitudes and Spang et al. (2012) for the MIPAS instrument. The threshold lines separate the clear air and cloudy cluster from each other, following the vertical gradient of the clear air cluster (Fig. 4.5 a, b).

Out of the total 13539 analyzed profiles, about 40 % were classified as clear sky. As seen in Fig. 4.5c, the relation between CI and extinction is not one-one. However, for CI between 3 and 5, which corresponds to optically thin clouds (Spang et al., 2008), the relation is stronger.
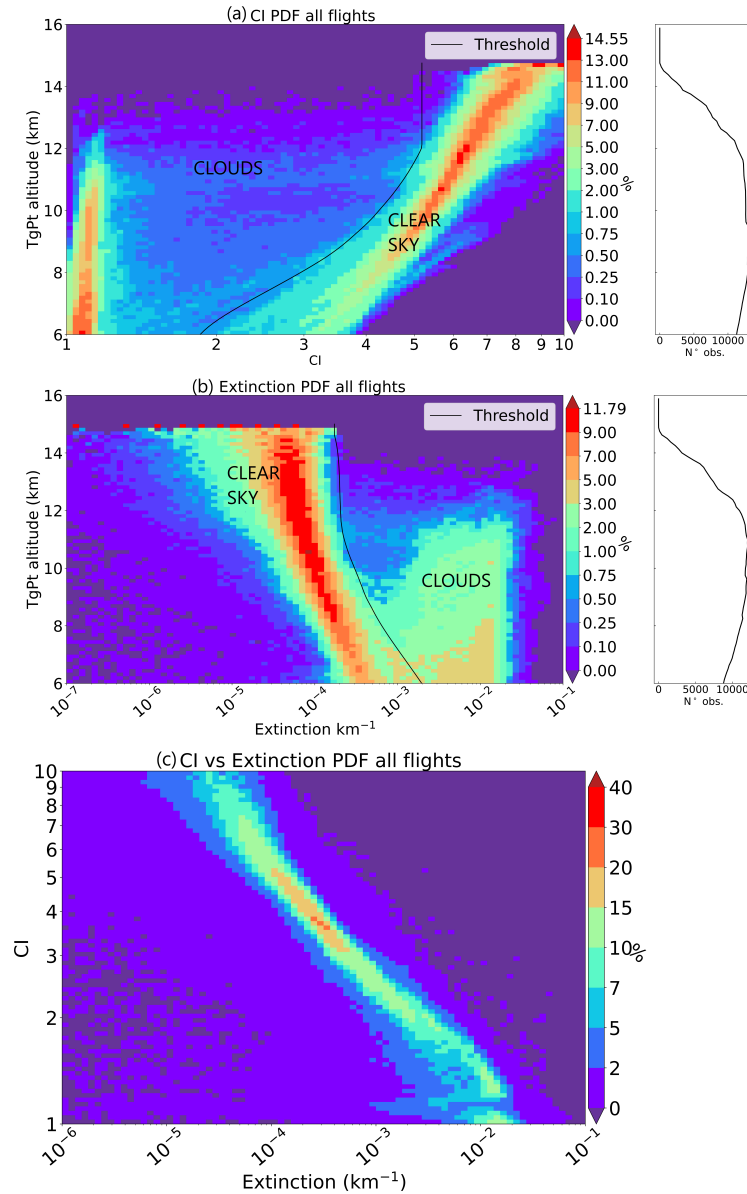
Figure 4.5: PDF for CI and extinction for all flights including all profiles. The bins are normalized by altitude. In black the threshold for differentiating cloudy conditions from clear sky. For (a) clouds correspond to small CI, i.e, the left side of the CI_{thres}. For (b) clouds correspond to high extinction, i.e., to the right side of the k_{thres}. The altitude of the tangent points (TgPt) is the y-axis. The plot placed to the right of (a) and (b) indicates the number of observations per altitude for each detection method. (c) PDF of CI as a function of extinction, normalized by CI. The total number of analyzed profiles is 13539.

4.3 Differentiation between clouds and aerosol

During the summer months several wildfires started in British Columbia and California that continued until September – October. Also in the Iberian Peninsula during mid-October mayor wildfires occurred. Besides these wildfires, 70 volcanoes around the globe erupted, for example in Russia, Hawaii or Nicaragua (Global Volcanism Program, 2013). These eruptions and the large fires are responsible for the emission of large amounts of aerosols into the atmosphere. Enhanced aerosol number densities can affect the CI values and cause false cloud detection. To investigate if the presence of aerosol particles influenced the results, two methods described by Griessbach et al. (2014) and Griessbach et al. (2016) were applied. These methods take advantage of the different wavelength dependence of ice and aerosols, such as volcanic ash or sulfuric acid, in five wavelength regions to establish thresholds that differentiate them. The chosen microwindows, adapted to the spectral sampling of GLORIA, are: $825.6\,\text{cm}^{-1}$ to $826.4\,\text{cm}^{-1}$, $830.6\,\text{cm}^{-1}$ to $831.2\,\text{cm}^{-1}$, $950.0\,\text{cm}^{-1}$ to $951.0\,\text{cm}^{-1}$, $960.0\,\text{cm}^{-1}$ to $961.0\,\text{cm}^{-1}$ and $1\,224.0\,\text{cm}^{-1}$ to $1\,224.6\,\text{cm}^{-1}$. Hereafter these windows are referred as the 825, 830, 950, 960 and $1224\,\text{cm}^{-1}$ windows. Both discrimination thresholds were obtained from MIPAS measurements, from the analyses of the observations of several volcanic eruptions during 2011, and from radiative transfer simulations. The simulations of clear air, ice clouds, sulfate aerosol and volcanic ash layers were performed with JURASSIC, including scattering, and for different scenarios: polar winter, polar summer, mid-latitude and tropical atmosphere (Remedios et al., 2007).

4.3.1 Volcanic ash vs. ice clouds

To differentiate between volcanic ash clouds and ice clouds, Griessbach et al. (2014) used the $825\,\text{cm}^{-1}$ and $950\,\text{cm}^{-1}$ windows and defined the following threshold:

$$I(950\,\text{cm}^{-1}) \geq 2.5 \times I(825\,\text{cm}^{-1}) + 2.5 \times 10^{-7}\,\text{W/(cm}^2\,\text{sr}\,\text{cm}^{-1}), \qquad (4.2)$$

which can also be applied for the detection of mineral dust and smoke from wildfires. All points at or above this threshold are classified as non ice particles. Fig. 4.6a includes all observations for all scientific flights. Most of the measurements that would be classified as volcanic ash, were at 8 km or lower. Therefore, these results strengthen the decision of only analysing the data above 8 km. When considering only cirrus measurements, identified with the thresholds defined in Sec. 4.2, a few observations fell at or slightly above the threshold (Fig. 4.6b). These points, that could be volcanic ash, correspond to clouds between 8 and 9 km. Most of them belong to two clouds in flight 8 and to isolated occurrences in flights 9 and 12 for the extinction method, and to one cloud in flight 8 and a single occurrence in flight 9 for the CI method.

4.3.2 Ice vs. non ice particles

Griessbach et al. (2016) created a simple color ratio method to differentiate between ice particles and non ice particles, such as volcanic ash and sulfate aerosol. This method uses the aerosol index (AI), which is sensitive to aerosols, defined as:

$$AI = \frac{\bar{I}[788.2 - 796.2]\text{cm}^{-1}}{\bar{I}[960.0 - 961.0]\text{cm}^{-1}},$$ (4.3)

combined with the CI to create a new index, the aerosol cloud index (ACI), defined as the maximum of the CI and the AI. Griessbach et al. (2016) established a constant threshold of 7 for the ACI and only measurements with a lower value are analyzed. The next step is to use the following brightness temperature differences (BTDs):

- BT(960 cm^{-1}) − BT(1 224 cm^{-1})

- BT(830 cm^{-1}) − BT(1 224 cm^{-1})

together with the following threshold for BTDs larger than –30.4 K:

$$BTD_{960-1224} = 0.87 \times BTD_{830-1224} + 6\,\text{K}$$ (4.4)

and the threshold for BTDs lower than −30.4 K:

$$BTD_{960-1224} \;=\; 1.33 \;\times\; BTD_{830-1224} \;+\; 20\,\text{K} \tag{4.5}$$

All points at or above the threshold correspond to aerosols. Figure 4.7a includes all observations from all scientific flights. Once again, the affected measurements were located at 8 km or lower. As can be seen in Fig. 4.7b, when considering only the cirrus occurrences there are no cloudy observations at or above the threshold for any of the identification methods. This gives confidence for the conclusion that the analysed spectra correspond to ice particles and not to volcanic ash or sulfate aerosol.

These results, combined with the results of the previous subsection, give confidence to conclude that the influence of aerosols in the analyzed cloud measurement is negligible and only one flight seems to be slightly affected by mineral dust or smoke.
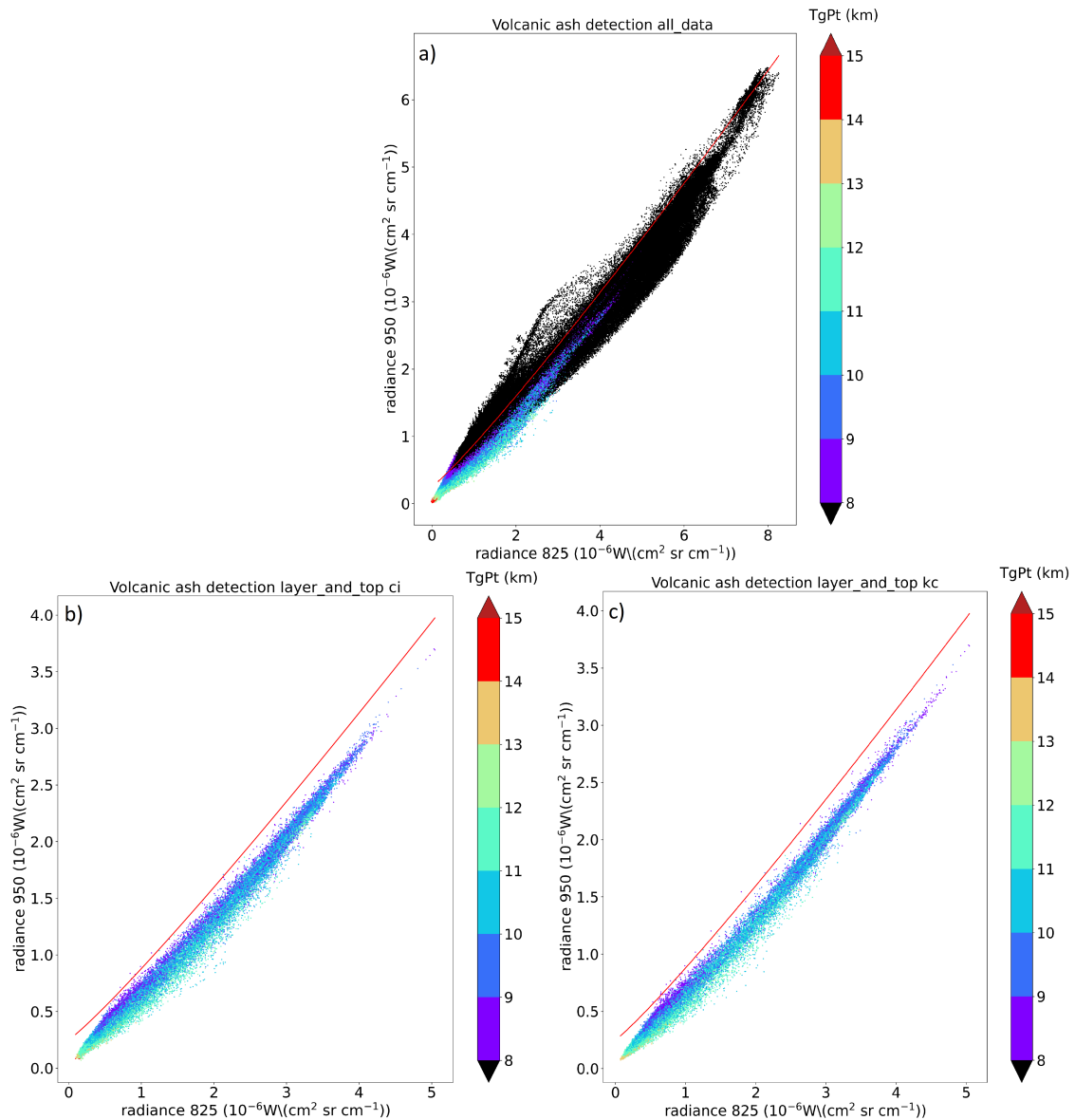
Figure 4.6: Differentiation between ice particles and volcanic ash, mineral dust and smoke from wildfires following the criteria by Griessbach et al. (2014). (a) All observations from all scientific flights together. (b) Only cloudy layers and cloud tops of optically thick clouds identified with the CI method. (c) The same as (b) but for the extinction method. Color code indicates the altitude of the tangent point (TgPt). Observations above the threshold are not ice particles.
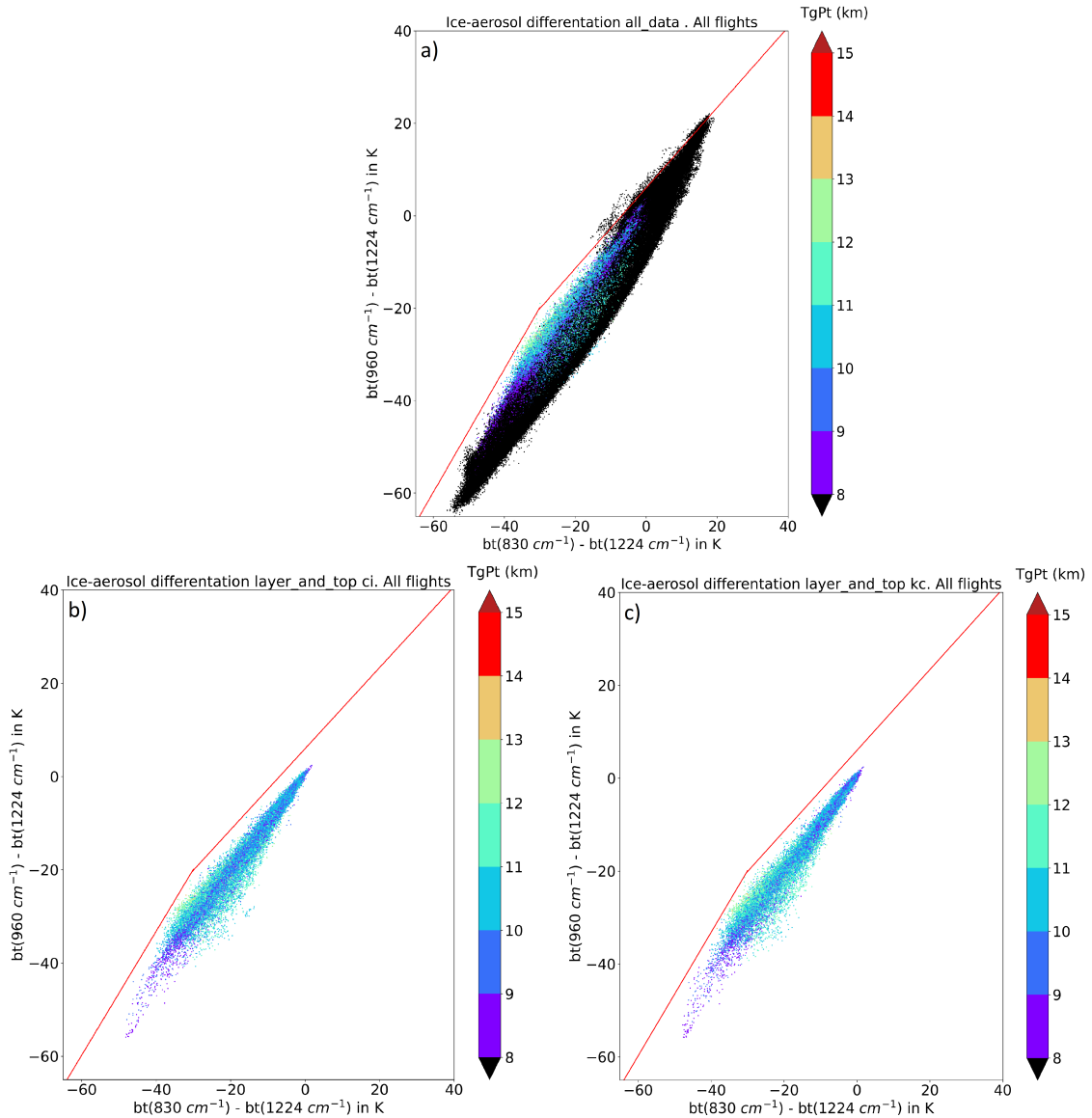
Figure 4.7: Differentation between ice particles and aerosols, such as volcanic ash and sulfates following the criteria by Griessbach et al. (2016). All observations from all scientific flights together. b) Only cloudy layers and cloud tops of optically thick clouds identified with the CI method. c) The same as b) but for the extinction method. Color code indicates the altitude of the tangent point (TgPt). Observations above the threshold are not ice particles.

Chapter 5

Macro-physical properties

This chapter includes the results regarding the macro-physical properties of cirrus clouds, i.e., the altitude of their cloud top, cloud bottom, their vertical extent and their position with respect to the tropopause. Their definition is presented in Sect. 5.1 and their analysis in Sect. 5.2. For the study of the location of cirrus with respect to the tropopause, the definition of the tropopause is a key point, as different definitions lead to different results (Pan and Munchak, 2011). The analysis was done with respect to the first thermal tropopause and the second thermal tropopause following the definition of the WMO (World Meteorological Organization) using the ERA5 dataset (Sect. 5.3). A comparison of the GLORIA measurements with the ERA5 dataset is included.

5.1 Definition of the macro-physical characteristics

As explained in Sect. 2.4, in the limb geometry, the position of the cloud along the LOS is not exactly known. For analyzing the data, the observed clouds were referred to the tangent point and the corresponding tangent height layer. Using this definition of the cloud position, the cloud top height (CTH) is defined as the first point in which the extinction (CI) is equal to or larger than the k_{thres} (less than or equal to the CI_{thres}) described in Sect. 4.2. As a homogeneous cloud layer was assumed, the real extinction might be underestimated. This could cause an underestimation of the CTH for some cases, in which the cloud is on the ray path far from the tangent point location (Kent et al., 1997)

(see Sect. 2.4). All the CTHs belong to the first cloud detected, i.e., the analysis does not include multi-layer clouds (two or more clouds with a clear separation in between).

Using the extinction method, the cloud bottom height (CBH) is the altitude of the first detection in the series of limb observations with an extinction smaller than the k_{thres}; this ensures the identification of an altitude at or below the true cloud bottom. For the CI method, the CBH was computed using the minimum of the CI gradient of the profile (Kalicinsky et al., 2021). CBH could only be reliably determined for optically thin clouds. For optically thick conditions, the CI profiles saturate and the extinction profiles decrease in an unrealistic manner. Optically thick profiles are characterized by CI lower than 1.2 from an altitude h down to the lowest altitude (Spang et al., 2015, 2016). Optically thin profiles, i.e. with small extinction, are those for which it was possible to define a CBH. Figure 5.1 shows an example of a saturated CI profile and a profile for a cloud layer. It is possible to observe how the CI profile reaches saturation for altitudes below where the CI becomes smaller than 1.2. The last macro-physical characteristic that was analyzed is the vertical extent, defined as the CTH – CBH.

As described in Sect. 3.4, to perform a comparison between the GLORIA results and the ERA5 dataset, the needed variables from ERA5 were sampled following the instrument geometry. One of the computed variables was the IWC, which when integrated along the LOS, results in the limb IWP. The CTH in the ERA5-based dataset is the highest tangent point for which IWP > 0.

5.2 Analysis of cloud top height and cloud bottom height

During the WISE campaign, 61 % of all observed profiles show CTHs using the extinction method and 59 % for the CI approach. 58 % of all profiles show a CTH for both methods, which indicates a similar performance. These percentage is also in agreement with the ERA5-based dataset, for which the fraction of detected CTHs is 59 %. These fractions are comparable to the climatology presented in Goldfarb et al. (2001) for lidar observations, with a cirrus occurrence frequency of 60% for fall. However, a fraction of 60 % is considerably larger than the $\approx$17 % reported by Sassen et al. (2008) for CALIPSO measurements
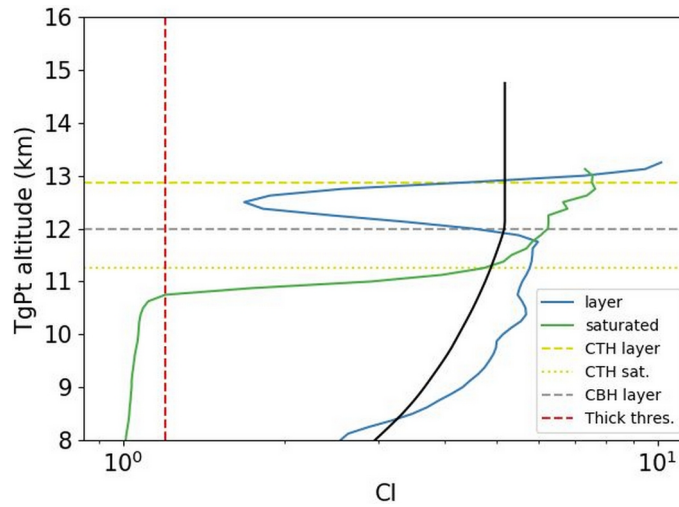
Figure 5.1: CI profile for a cloud layer (blue) and an optically thick case (green) that saturates. The horizontal yellow lines indicate the cloud top height (CTH) for the layer (dashed line) and the thick case (dotted line). The horizontal dashed line in grey is the cloud bottom height (CBH) of the cirrus layer. The red vertical line corresponds to CI = 1.2 i.e. optically thick cases. In black, the CI threshold. The altitude of the tangent points (TgPt) is the y-axis.

and the International Satellite Cloud Climatology Project (ISCCP) for mid-latitudes. It is rather unlikely that this difference is related only to the disparate observational periods, but also to the differences in cirrus cloud selection criteria of the studies. While for this thesis there is no temperature threshold, Sassen et al. (2008) considered as cirrus only clouds with $\tau < \approx 3.0 - 4$ and with a maximum cloud top temperature of -40 °C. Goldfarb et al. (2001) considered for the detection of cirrus a threshold that was defined for each nighttime measurement and required that the cloud layer was in an air mass with a temperature of -25 °C or lower. The extinction method and the CI method show good agreement in the determination of the CTHs, presenting a similar distribution (Fig. 5.2 a and b). Fig. 5.2 shows the distribution of CTHs as a function of the equivalent latitude. The equivalent latitude is a variable that helps to determine the origin of the air masses. The CTHs between 8 and 10 km were observed in air masses with equivalent latitudes that spread from tropical to polar regions, having a slightly higher frequency at the polar equivalent latitudes. CTHs between 10 km and about 12.5 km often occurred at equivalent latitudes typical for mid-latitudes, whereas the CTHs above about 12.5 km were related to subtropical equivalent latitudes. For both identification methods, there is

slightly higher frequency of observations following the zonal mean tropopoause (as function of the equivalent latitude) between $30 - 50°$N. Since lowest temperatures are found close to the tropopause, it is natural to find more cirrus in the tropopause region, as the conditions for their formation are favorable. The main difference between both methods is that the CTHs inferred from the CI are slightly higher ($1 - 2$ grid points) than for the extinction method. The results from ERA5 (Fig. 5.2c) show a similar pattern of inferred CTHs as those derived from the measurements.
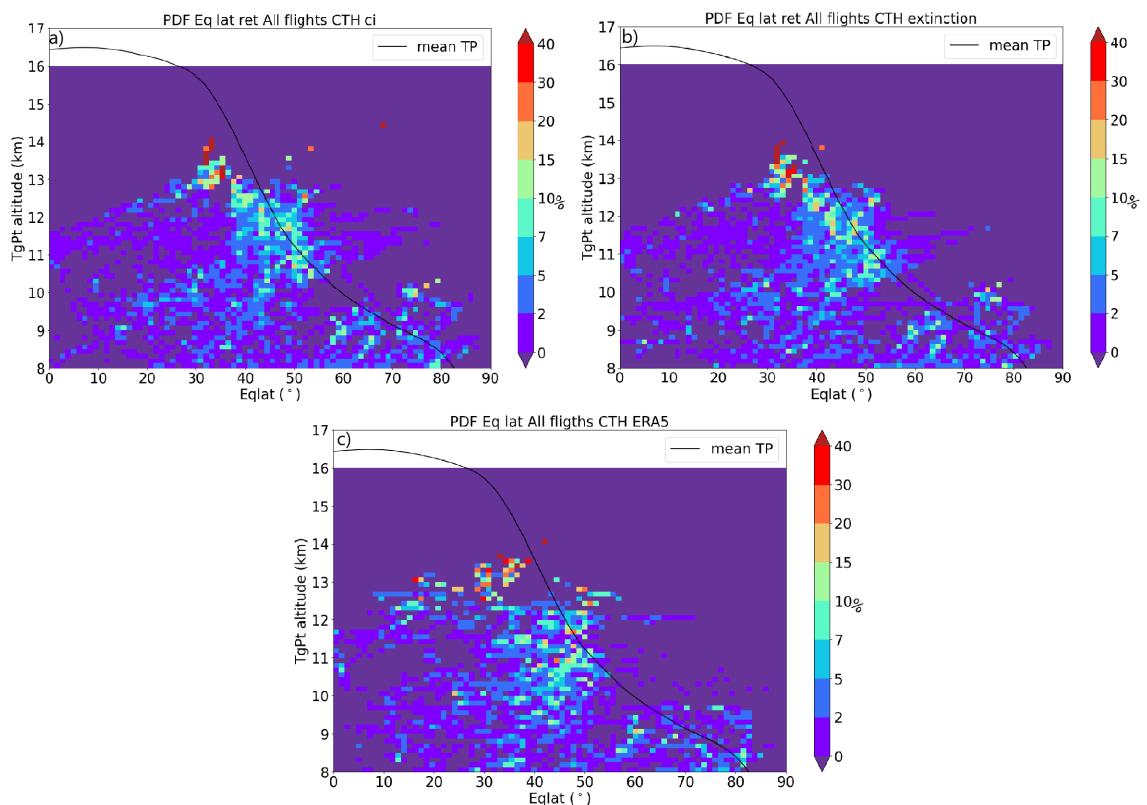
Figure 5.2: PDFs of CTHs as function of equivalent latitude (Eqlat) normalized for each altitude bin from (a) the CI, (b) the extinction and (c) ERA5. The y-axis shows the altitude of the tangent points (TgPt). The black line represents the zonal mean tropopause height during September-October 2017 as a function of the equivalent latitude. It was computed from ECMWF analysis data.

Figure 5.3 shows that between 8 and 11 km altitude, ERA5 indicates more frequently CTHs than the observations. This could be related to discarded multi-layer clouds in the detection algorithm. However, it can also be related to the instrument being sensitive to higher and thinner cirrus clouds than the clouds assimilated by ERA5. In Appendix A

cross-sections comparing the inferred ERA5 cirrus and the observed ones are presented as a classification of true-true, true-false, false-true, false-false cases, where this effect is clearer. ERA5 misses a large fraction of the higher cirrus that are close to the tropopause. Figure 5.4 shows an example where the cirrus between approximately 6:45 UTC and 8:30 UTC are detected by GLORIA but not assimilated by ERA5. Other differences can be related to the measuring time. While GLORIA is measuring continuously every few seconds, the ERA5 based dataset has hourly resolution. The largest number of GLORIA occurrences that are not matched by ERA5 occur around the tropopause, between 1 km under it and about 0.5 km above it. For the opposite case, i.e., ERA5 occurrences not matched with GLORIA observations, the largest incidence is located between 4 and 1.5 km under the tropopause.
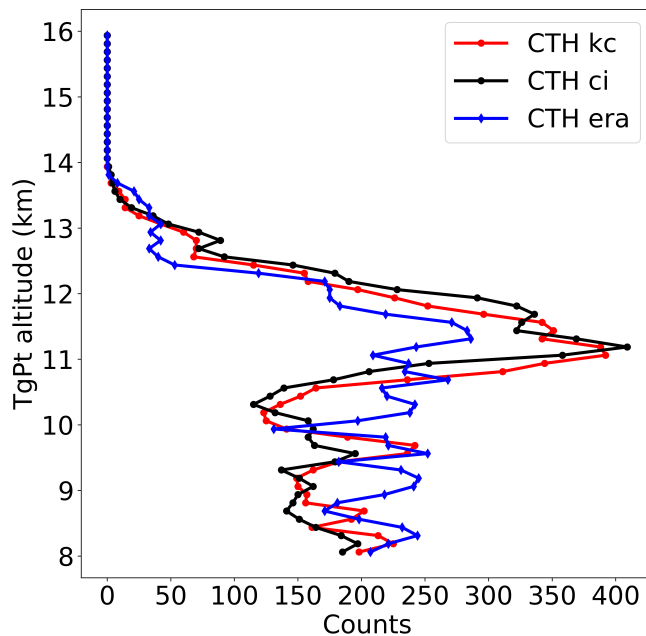
Figure 5.3: Number of cloud top heights (CTH) per altitude bin for the extinction method (*kc*) (red line), the CI method (black line) and ERA5 (blue line). The altitude of the tangent points (TgPt) is the y-axis. The used tropopause is the median tropopause (TP$_{med}$). The three profiles were smoothed with a three points running mean.

From all considered profiles (13539), about 39 % (5232 profiles) become optically thick using the extinction and 41 % (5517 profiles) the CI method. 36 % of all profiles
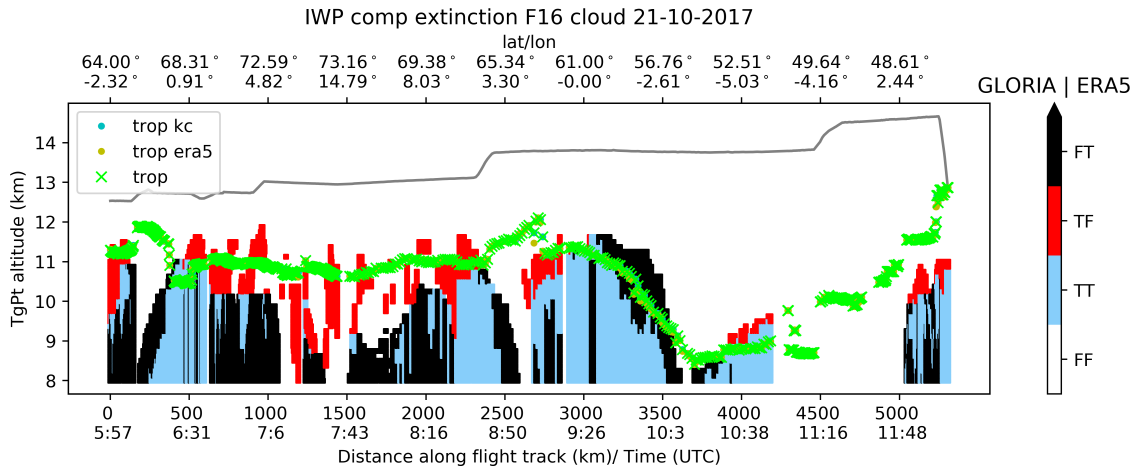
Figure 5.4: Cross-section comparing ERA5 inferred clouds and clouds identified with the extinction method for GLORIA for flight 3 of the WISE campaign. The results are restricted to levels below flight path (grey line). Color code represents the true-true cases (TT, in light blue) when both datasets identified a cloud; true-false (TF, in red) when a cloud was observed with GLORIA but ERA5 indicated clear air; false-true (FT, in black) when GLORIA indicated clear air and ERA5 registered a cloud and false-false (FF, in white) when both datasets indicated clear air. The blue dots indicate the median tropopause TP_{med} corresponding to the location of the observed cirrus by GLORIA. The yellow dots represents the TP_{med} corresponding to the location of the inferred cirrus with ERA5. The green crosses indicate the combined TP_{med}. The altitude of the tangent points (TgPt) is the y-axis.

become optically thick for both methods. The maximum extinction detected for optically thin clouds in which a CBH was possible to determine is 4×10^{-2} km^{-1}. The distribution of the vertical extent of clouds is presented in Fig. 5.5. The extinction method results in a higher amount of vertically thin clouds than the CI method, due to the slightly higher CBHs of the extinction method (Ungermann et al., 2020). For both methods, a large fraction of the optically thin cirrus clouds were located between $45 - 65°$N and had a vertical extent smaller than 1.5 km (31 % of the clouds detected with the extinction method and 20 % of the clouds detected with the CI method). These results are qualitatively similar to the findings of Noël and Haeffelin (2007). They showed that between May and November the frequency distribution of the vertical extent of the observed clouds was biased towards values between 0 and 1.5 km. The results presented in this thesis are also in agreement with the mean layer thickness of 1.4 km computed by Goldfarb et al. (2001).
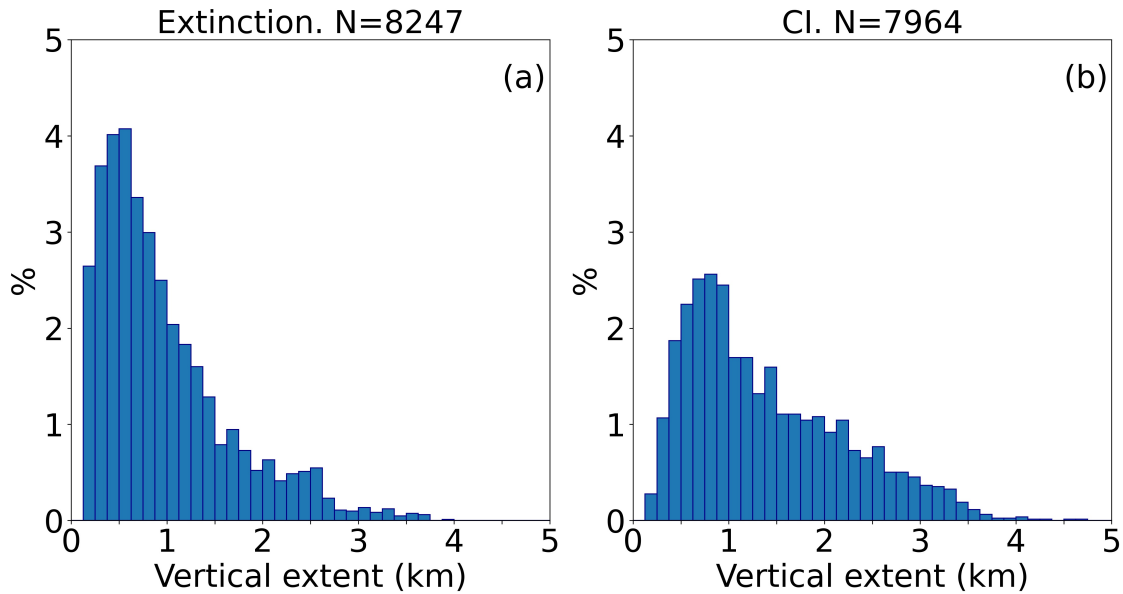
Figure 5.5: Distribution of the vertical extent of cirrus clouds for all flights for (a) the extinction method and (b) the CI method. The percentage is given in relation to the total number of CTHs (N) detected for each method.

5.3 Cloud top position with respect to the tropopause

The occurrence frequency of cirrus clouds above the tropopause remains a matter of debate. The exact computation of the tropopause height is crucial for such an analysis. However, accuracy on the determination of the tropopause height is limited by the vertical and horizontal resolution of the underlying temperature profile of the meteorological analysis and also by the measurement geometry. As discussed in Pan and Munchak (2011) different definitions of the tropopause can lead to different results. For this study, the first thermal tropopause altitude (see definition in Sect. 2.1) was computed from the ERA5-based dataset following the GLORIA geometry. For each LOS, every 30 km the closest ERA5 temperature profile was chosen. To this temperature profile, a high resolution spline fit was applied on a 20 m grid for a more precise determination of the tropopause height, following a similar procedure described in Spang et al. (2015). Then, the definition of thermal tropopause was applied. The result is a tropopause height for every point (every 30 km) along the LOS, up to a maximum of 20 km, as it is not expected to find clouds at so high altitudes during the WISE period. The LOS of GLORIA typically extends several hundreds of kilometers from the instrument to the tangent height, hence the sampled

air masses could be heterogeneous in the horizontal. To take into account the variability of the tropopause along the LOS, two altitudes for the tropopause were computed for each LOS where a CTH was identified: the median and the percentile 95. The median is a more relaxed criteria, whereas the percentile 95 is a very conservative approach. Considering that the altitude of the determined cloud top could be lower than the true one (Sect. 2.4) if a cloud top is above the percentile 95, it gives confidence to conclude that cloud tops were observed above the tropopause, despite the uncertainty in its exact location. Table 5.1 provides a deeper insight into the variability of the tropopause height for each flight, taking into account the maximum (max), the minimum (min), the median (med) and the percentile 95 (p95) of the tropopause. The maximum of the difference max − min (of all flights) is around 8 km, however, the median of the max-min is about 1 km for each flight, indicating that such a big difference is not often encountered.

Additionally, the dynamical tropopause (TP_{dyn}) was obtained from the dataset provided by J. Clemens following the work of A. Kunz (Kunz et al., 2011) (personal communication with J. Clemens). This dataset contains the TP_{dyn} computed from ERA-Interim wind velocity and potential temperature every six hours for θ levels between 300 and 400 K. Only the period from the 13 of September 2017 to the 21 of October of 2017 was selected. For each level, the median TP_{dyn} was computed for the selected period.

All extinction and CI cross-sections of the WISE campaign with CTHs, CBHs, median tropopause (TP_{med}) and the percentile 95 (TP_{95}) can be found in Appendix B. Figure 4.3 illustrates the case of a flight with both homogeneous and heterogeneous air masses. E.g. the air mass at 16:18 UTC was homogeneous and TP_{med} and TP_{95} are close to each other (less than 125 m apart). At 11:29 UTC, there were heterogeneous air masses with TP_{med} and TP_{95} separated (three times the distance of the previous example), which affects the statistics of CTHs above the tropopause, since as to whether the CTH is located above or below the tropopause depends on the chosen tropopause criterion.

For the extinction method, the occurrence frequency of CTHs above the TP_{med} is 24 % of the total number of observations, whereas for the CI method the ratio is 27 % (Fig. 5.7). The ≈3 % difference is due to the CI detecting CTHs slightly higher than the extinction

Table 5.1: Variability of the tropopause height along the LOS of GLORIA for each scientific flight and for all flights. The differences include the median (med), maximum (max), minimum (min) and 95 (p95). All values are expressed in kilometers.

	med(max-min)	med(max-p95)	med(p95-med)	med(med-min)
F02	0.6	0.02	0.18	0.23
F03	0.8	0.02	0.23	0.43
F04	0.59	0.02	0.11	0.33
F05	1.02	0.05	0.34	0.44
F06	0.77	0.02	0.2	0.46
F07	1.28	0.03	0.5	0.6
F08	0.79	0.03	0.3	0.41
F09	0.9	0.02	0.35	0.45
F10	0.9	0.02	0.37	0.28
F11	0.39	0.02	0.16	0.17
F12	1.38	0.03	0.6	0.4
F13	1.02	0.04	0.37	0.32
F14	2.1	0.05	0.5	0.98
F15	1.05	0.02	0.46	0.41
F16	0.37	0.01	0.13	0.16
Med all	0.93	0.03	0.32	0.4
Max all	8.3	2.94	7.52	6.8
Min all	0.03	0	0.008	0.01

method. When considering TP_{95}, the percentages decrease to 13 % and 16 % respectively as it uses a more conservative criterion. This gives confidence to conclude that CTHs above the lapse rate tropopause were detected, even when considering the uncertainties in the CTH determination, which is in the order of ± 125 m. Figure 5.6 shows the distribution of all CTHs (Fig. 5.6a) and the distribution of CTHs above TP_{med} (Fig. 5.6b) for the extinction method. As can be seen, most of the occurrences of CTHs above TP_{med} were found between $50 - 70°N$, with varying altitudes from 10 km to 14 km. About 6 % of all profiles show for both methods CTHs above the TP_{med} and are classified as optically thin. The ratio of clouds with both CTH and CBH above the TP_{med} is 2 % for the extinc-

tion method and 1 % for the CI method. When considering the TP_{95}, both occurrences decrease but still CBHs above the tropopause were detected (< 1 %). The presence of complete layers above the tropopause is inconclusive, since these CTHs and CBHs are only separated by one altitude bin and the CBH is only one or two altitude bins above the tropopause, which is within the uncertainties of the CBH. When comparing the observations with the ERA5-based results (Fig. 5.7), is it possible to see that the distribution of all CTHs is similar beyond 0.5 km distance from the TP_{med}. Between –0.5 km to 0.5 km, there are more cirrus measured by GLORIA than present in ERA5. When considering all occurrences above the TP_{med}, the observations indicate about 50 % more cirrus clouds than found in ERA5. This result indicates limitation in the cloud scheme used in the assimilation system of ERA5 for these optically thin clouds close to the tropopause.

The results presented in this thesis (summarized in Table 5.2) agree with previous studies that claim the detection of CTHs above the tropopause for mid-latitudes. Goldfarb et al. (2001) used lidar ground based instruments and found 5 % of CTHs at least 1 km above the tropopause, and approximately 15 % above 0.5 km. Spang et al. (2015) analyzed CRISTA data and concluded to a 5 % occurrence frequency of cirrus clouds (of all observations) and Zou et al. (2020) inferred their occurrence to 2 % for CALIPSO data and 4 – 5 % for MIPAS data. The analyses of Spang et al. (2015) and of Zou et al. (2020) used the criterion of the cirrus CTH being 0.5 km above the ERA-Interim thermal tropopause. Using the same criterion, the occurrence frequency is 4 % for CTHs above the TP_{med} for the extinction method and 7 % for the CI method. These occurrence frequencies are comparable to those reported in the literature (Goldfarb et al., 2001; Spang et al., 2015; Zou et al., 2020). However, as for this study the used meteorological dataset was ERA5, which has a better vertical resolution than ERA-Interim, the equivalent criterion would be to mandate the cirrus CTH to be located 250 m above the tropopause. In this case, the occurrence frequency increases to 13 % above the TP_{med} for the extinction method and to 17 % for the CI method. These differences in the occurrence frequency can be explained by different periods being compared, the sensitivity and vertical resolution of the instruments, the uncertainty of the meteorological data used to estimate the
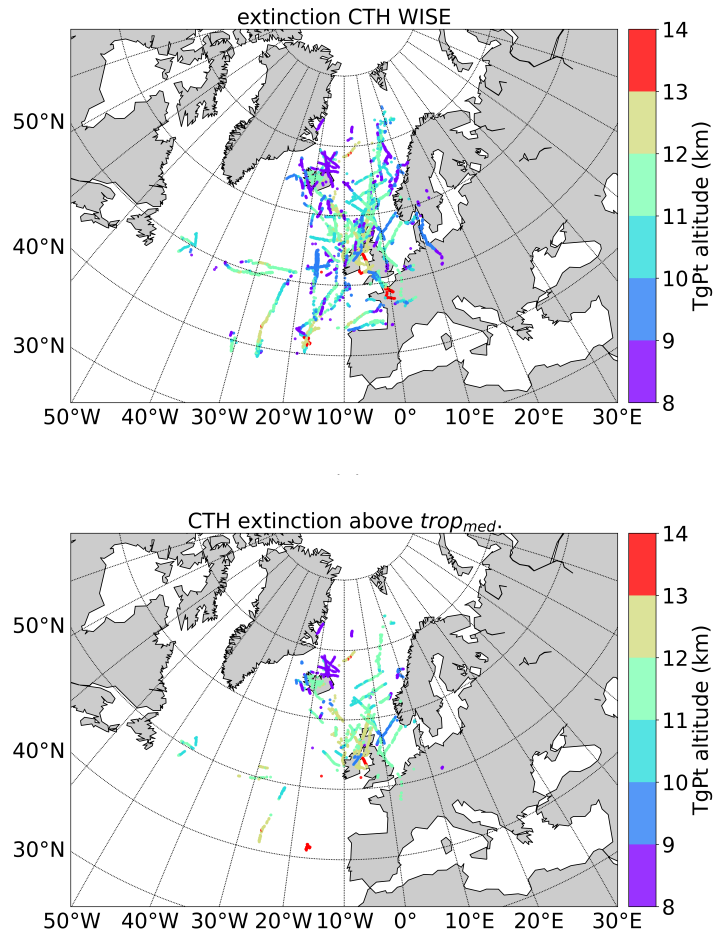
(b)

Figure 5.6: Distribution for (a) all cloud top heights (CTHs) for extinction with color code as the tangent point altitude in km (TgPt) and (b) CTHs for the extinction method above the median tropopause (TP$_{med}$). Colors indicate the tangent point altitude (TgPt).

tropopause height and the definition of stratospheric cirrus used in each study.

CTHs were also observed above the TP$_{dyn}$. For the extinction method, 18 % of the total number of profiles had a CTH above the TP$_{dyn}$ and for the CI method, 21 %. This frequencies of occurrence fall in between the results for the TP$_{med}$ and TP$_{med}$ plus 250 m.
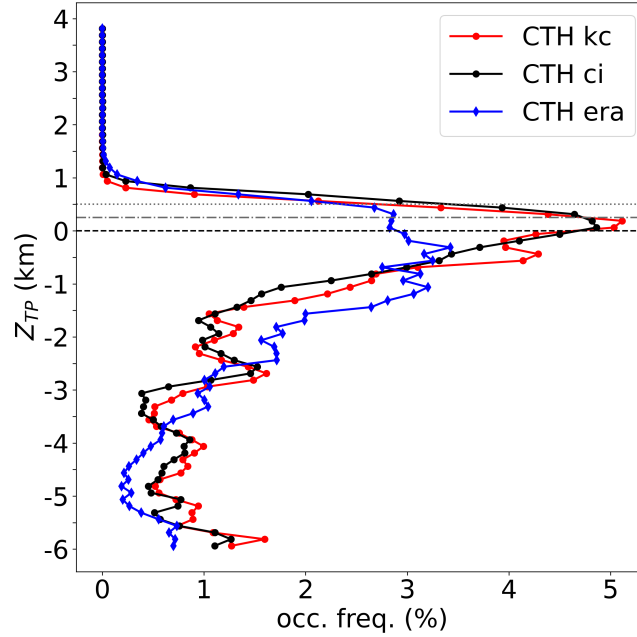
Figure 5.7: Occurrence frequencies of cloud top heights (CTH) per altitude bin for the extinction method (*kc*) in red, the CI method (black) and ERA5 (blue) in tropopause co-ordinates (Z_{TP}). The distance of the CTH to the tropopause is the y-axis. The used tropopause is the median tropopause (TP_{med}). The dash-dot and dotted grey lines are placed at 250 m and 500 m above the TP, respectively. The three profiles were smoothed with a three points running mean.

Table 5.2: Percentages of cloud top heights (CTHs) and cloud bottom heights (CBHs) detected above the median tropopause (TP_{med}) and the percentile 95 of the tropopause (TP_{95}) relative to all retrieved profiles for both detection methods. The last three rows correspond to the occurrence frequency of stratospheric cirrus from the studies of Goldfarb et al. (2001), Spang et al. (2015) and Zou et al. (2020).

	TP_{med}	TP_{med}	TP_{95}	TP_{95}
	CI	ext	CI	ext
CTH all	27	24	16	13
CTH thin	7	7	5	4
CTH and CBH	1	2	1	1
Goldfarb et al. (2001)	Lidar > 1 km	5		
	Lidar > 0.5 km	15		
Spang et al. (2015)	CRISTA	5		
Zou et al. (2020)	CALIPSO	2		
	MIPAS	$4 - 5$		

5.3.1 Cirrus and multiple tropopauses

Cirrus clouds that are located in between the first and second tropopause (see definition in Sect. 2.1) are called intertropopause cirrus. If only the cloud top of the cirrus is above the tropopause, then it is named cross-tropopause cirrus. The second tropopause was computed along the LOS following the same procedure as for the first tropopause. For the discussion, only the median of the second tropopause ($TP2_{med}$) is considered as in this case, the statistics do not vary if a more conservative criteria is used and in no case a CTH was observed above the second tropopause. Out of the 15 scientific flights of the WISE campaign, second tropopauses were found during 14 of them. The thickness of the intertropopause region extends 2 km to 13 km, with a maximum at $\approx$3 km. The frequency of intertropopause cirrus was negligible ($\approx$0.01 %) and as mention at the beginning of Sect. 5.3, the distance of the CBHs are within the uncertainties, and therefore there is no affirmation made of complete layers being detected above the tropopause. For the TP_{med} and $TP2_{med}$, the occurrence frequency of cross-tropopause cirrus varies from 5 – 6 % to 3 % (of all profiles) when the criteria of CTHs above the TP_{med} by more than 250 m is applied. 4 to 5 % of all profiles present a cross-tropopause cirrus that is thick and only 1 % thin cirrus. The vertical extent distribution of the thin cross-tropopause cirrus presents two maximums, one at $\approx$150 m and another at $\approx$1.5 km. When the TP_{95} is selected, all percentages decrease to $\approx$ 2 %. Both identification methods present similar frequencies of occurrence and distributions, which are summarized in Table 5.3.

Table 5.3: occurrence frequency of cross-tropopause CTHs with respect to the total number of CTHs considering the median of the second tropopause ($TP2_{med}$) together with the (TP_{med}) and the percentile 95 of the tropopause (TP_{95}) for both detection methods. All numbers are in percentage relative to the total number of profiles (13559).

	$TP_{med} + TP2_{med}$		$TP_{95} + TP2_{med}$	
	Ext	CI	Ext	CI
CTH above TP	5	6	2	3
CTH > 0.250 km above TP	3	3	2	2
Thin cirrus	1	1	<0.5	1
Thick cirrus	4	5	2	2

5.4 Cloud tops above the tropopause: meteorological situation

As introduced in Chapter 2.1, there are specific meteorological situations that trigger the formation of cirrus clouds. To study them, cross-sections with the retrieved PV and levels of potential temperature (θ) were analyzed. Usually the CTHs above the tropopause are observed around potential temperatures of 320 K, 330 K, 340 K and 350 K. These θ levels are selected for 2D maps of PV, N^2 and wind speed obtained from the ERA5 database with $1° \times 1°$ resolution. Additionally, meteorological charts from the United Kingdom Meteorological Office (UKMO) (Met Office, 2017) and IR images at 10.8 µm from SEVIRI were used. The meteorological charts include low and high systems and the associated fronts.

The meteorological analysis is focused on the cirrus with CTHs above the TP_{med}. Cirrus were found to be related mainly to fronts, followed by Rossby waves and to WCBs in last place. Additionally, one cloudy region is located in an area dominated by anti-cyclonic circulation. This case is further analyzed in Sect. 7.2.

5.5 Chapter conclusions

In this chapter, an analysis of the macro-physical properties CTH, CBH and vertical extent was performed for the CI method and the extinction method. The analysis focused on high cirrus clouds close to the tropopause and excluded multi-layer clouds. The extinction method identified very thin clouds with an extinction as low as 2×10^{-4} km^{-1}. The extinction method, the CI method and the ERA5-based dataset are in good agreement, since the occurrence frequency of profiles with CTHs is 61 % (of all observed profiles), 59 % and 59 %, respectively. The CTHs range from 8 km to $\approx$14 km, being the cloud tops more frequently detected at $\approx$11.5 km. From all considered profiles, about 39 % become optically thick using the extinction and 41 % the CI method. 36 % of all profiles become optically thick for both methods. A large fraction of the optically thin cirrus clouds were located between $45 - 65°$N and had a vertical extent smaller than 1.5 km (31 % of the clouds detected with the extinction method and 20 % of the clouds detected with the CI

method). The main differences are the slightly higher CTHs of the CI method and the more accurately CBHs identified by the extinction method.

Two criteria were applied to compute the tropopause. First, the median tropopause from ERA5 along the LOS of the GLORIA instrument and second, a more conservative criteria using the percentile 95. The occurrence frequency above the tropopause varied from 27 % to 16 % for the CI and from 24 % to 13 % for the extinction method, where the difference between both approaches were due to LOS scenes with heterogeneous tropopause heights.

The results presented in this chapter support the higher occurrence frequencies reported in literature (Goldfarb et al., 2001; Spang et al., 2015; Zou et al., 2020) in contrast to lower frequencies derived from CALIPSO (Pan and Munchak, 2011; Zou et al., 2020) at mid-latitudes. Using the same criterion as in Spang et al. (2015); Zou et al. (2020), i.e. 0.5 km above the tropopause, the occurrence frequency is 4 % − 7 %. Since the used dataset is ERA5, which has a higher vertical resolution, it is reasonable to consider 250 m above the tropopause instead of 0.5 km. With this new criteria, the fraction of CTHs above the tropopause increases to 13 % − 17 %. This means, that when the uncertainty of the tropopause estimate and the measurements is smaller, like for the GLORIA cloud measurements, the stratospheric cirrus cloud occurrence are even higher. Additionally, an analysis using the dynamical tropopause was performed, leading to occurrence frequencies between 18 % − 21 %. An important result is that the observed occurrence of cloud tops close to and above the tropopause is about 50 % higher than indicated by ERA5, which evidences that the thinner clouds close to the tropopause are missing in the re-analysis.

CBHs above the tropopause were found, but they were within the uncertainties. Consequently, the GLORIA WISE campaign data cannot confirm the presence of unattached cirrus layers above the first thermal tropopause, but can confirm the presence of cirrus clouds at the tropopause with cloud tops penetrating well into the lower stratosphere.

Chapter 6

Micro-physical properties

The aim of this chapter is to present the retrieval of the micro-physical variables defined in Sect. 6.1. Sect. 6.2 presents the procedure employed to estimate the micro-physical properties of the observed cirrus, based on a combination of different approaches. Section 6.3 includes the analysis of the limb ice water path/ice water content and the particle size.

6.1 Definition of micro-physical properties

The contribution of cirrus to the energy budget depends on their location, phase, type and micro-physics. Therefore, a better characterization of their micro-physical properties is necessary to improve our understanding and the representation of cirrus clouds in climate models. Micro-physical properties include, among others: ice water content, particle size and shape. In the following, the later analyzed properties and those necessary for their computation are defined.

To retrieve information about cirrus from remote limb observations, it is necessary to describe their particle size distribution (PSD). Cirrus PSDs are typically represented by gamma, exponential or log-normal distributions. According to Tian et al. (2010), the distribution that provides the best fit to the observed spectra is the log-normal distribution. However, there are recent studies using gamma distributions, such as Delanoë et al. (2014) to represent normalized PSD or Wolf et al. (2019), who parameterized gamma

distributions of Arctic cirrus. Hansen and Travis (1974) proposed a parameter that would be representative for the PSD to facilitate the solution of the inversion problem from remote sensing techniques. Such parameter is the mean radius for scattering (r_{sca}). In case the wavelength of the incident radiation is smaller or similar to the r_{sca}, the r_{sca} can be approximated by the effective radius (r_{eff}) or area-weighted mean radius:

$$r_{eff} = \frac{\int_{r_1}^{r_2} \pi r^3 \frac{dN}{dr} dr}{\int_{r_1}^{r_2} \pi r^2 \frac{dN}{dr} dr}, \tag{6.1}$$

where dN/dr is the PSD. If the PSD is described by a mono-modal lognormal distribution, the r_{eff} and the median (μ) of the PSD are related as follows:

$$r_{eff} = \mu e^{2.5 \log \sigma^2}, \tag{6.2}$$

with σ the width of the PSD. For this thesis, the selected PSD is a mono-modal log-normal distribution with a width σ = 1.4.

A fundamental quantity to describe cirrus is the ice water content (IWC), i.e the cloud ice mass in a unit volume of atmospheric air. It represents the amount of frozen water and is proportional to the extinction coefficient and the effective radius. The IWC covers several orders of magnitude, depending on the type and origin of the cloud. According to the extensive climatology presented in Krämer et al. (2020), the IWC spreads from 1×10^{-7} gm^{-3} to 1 gm^{-3}. This climatology includes also tropics, where the largest IWCs are usually found, where typically liquid origin cirrus are located. On the contrary, the lowest IWC are observed at higher altitude, where in situ cirrus are more common. The integral of the IWC is the ice water path (IWP). As the radiance measured by GLORIA is integrated along the LOS, the property analyzed in this thesis is the limb IWP.

The shape (or habit) of ice particles is determined by the temperature and saturation conditions that define the cloud formation process. It can vary from simple needles, columns and plates when there is a slight supersaturation, to elaborate dendrites, bullet rosettes or complex clusters under high supersaturation (Magono and Lee, 1966; Lawson et al., 2006). As mentioned in Sect. 3.3.3, crystal habits determine the light scattering

properties, and therefore, the effect of cirrus on climate. The assumed crystal shape for this thesis are spheres. This approximation is valid as long as the effective size of the particle is less than 30 µm (Baran et al., 2003). In the climatology presented by Krämer et al. (2020), the size of cirrus spread from 1 µm to 200 µm. Typical cirrus at European mid-latitudes are related to slow updrafts frontal systems. These synoptic cirrus have a mean radius of 10 µm and larger (Rolf, 2013).

Another micro-physical characteristic that determines the optical properties of ice particles is the complex refractive index, which describes how fast the light travels through the particle. The complex refractive index is divided in a real part that describes the refraction and an imaginary part, that describes the attenuation. The imaginary part will be zero for the non-absorbing particles. It is wavelenght and temperature dependent. Several studies focus on developing tables with the complex refractive index of ice crystals and aerosols. For this thesis, the selected table for ice is described in Toon et al. (1994). It is specific for the infrared region and the data was measured at 163 K.

6.2   Estimation of micro-physical properties

In this thesis, the estimated micro-physical properties are the limb IWP and the median radius (R_{med}). The procedure used to estimate them is based on the combination of two approaches: a look-up table in which particle size depends on IWC and temperature, and the relation between extinction coefficient and IWC with particle size. The look-up table is constructed by Donovan (2003) using lidar signals, radar reflectivity and average radar Doppler velocity. From the instruments, Donovan (2003) derived ice-cloud effective size and fitted the data from the Atmospheric Radiation Measurement Program's Southern Great Plains site to a bimodal gamma size distribution model. The parametrization can be used to calculate different quantities as a function of temperature and IWC. Look-up tables for two habits, complex polycrystal and compact polycrystal are available. The look-up table employed in this thesis is the one for compact polycrystal particles. This table was chosen because this habit is closer to spheres of small radius, which fits better to the assumptions of the second part of the procedure in which the Mie calculation is

applied and therefore, spherical particles are assumed. For the second part, the relation between IWC and extinction depending on the particle size is determined. To do so, Mie calculations together with a log normal distribution with $\sigma = 1.4$ and complex refractive indexes for ice tabulated at 163 K by Toon et al. (1994) for a wavenumber of 830 cm^{-1} are used. It is important to note, that the radius specified in the look-up table from Donovan (2003) is the effective radius (from a bimodal gamma distribution), whereas the one in the IWC vs. extinction relation is the median radius (from a log-normal distribution). Even thought there is an impact in the final result, the effective radius (r_{eff}) was transformed into median radius (μ) via Eq.6.2:

$$\mu = \frac{r_{\text{eff}}}{e^{2.5 \times \log \sigma^2}} \tag{6.3}$$

As explained in Sect. 2.4 and Sect. 3.4, each analyzed vertical profile is formed by multiple LOS with different elevations angles. For each LOS, the latitude, longitude and altitude of points every 30 km was computed. This information is crucial to be able to determine the limb IWP. The first step is to assign an extinction value to each point along the LOS. As the altitude of the point is known, the extinction of the closest tangent height is assigned to it. Note that the tangent height layer is assumed homogeneous in the radiative transfer model. The same is done with the temperature. Once these variables are computed for the the complete LOS, an iterative process to determine the final IWC is applied. This iterative computation works as follows (Fig.6.1): first, for each point along the LOS, an initial value of IWC is given. With this value and the temperature of that point the corresponding radius is found in the look-up table from Donovan (2003). With this radius, together with the corresponding extinction at that point, another value for IWC is found, which together with the temperature serves as an input for the first step of the next iteration. The procedure continues until there is convergence (Fig. 6.1). Once the R_{med} and the IWC are estimated for all points, the ice water path (IWP) is calculated as the integral of the IWC along the LOS.

In theory, the micro-physical properties can be calculated for all points. However, due to the unphysical behaviour of the extinction profiles when the clouds reach opaque

conditions, only the results for optically thin clouds are reliable, and therefore analyzed.
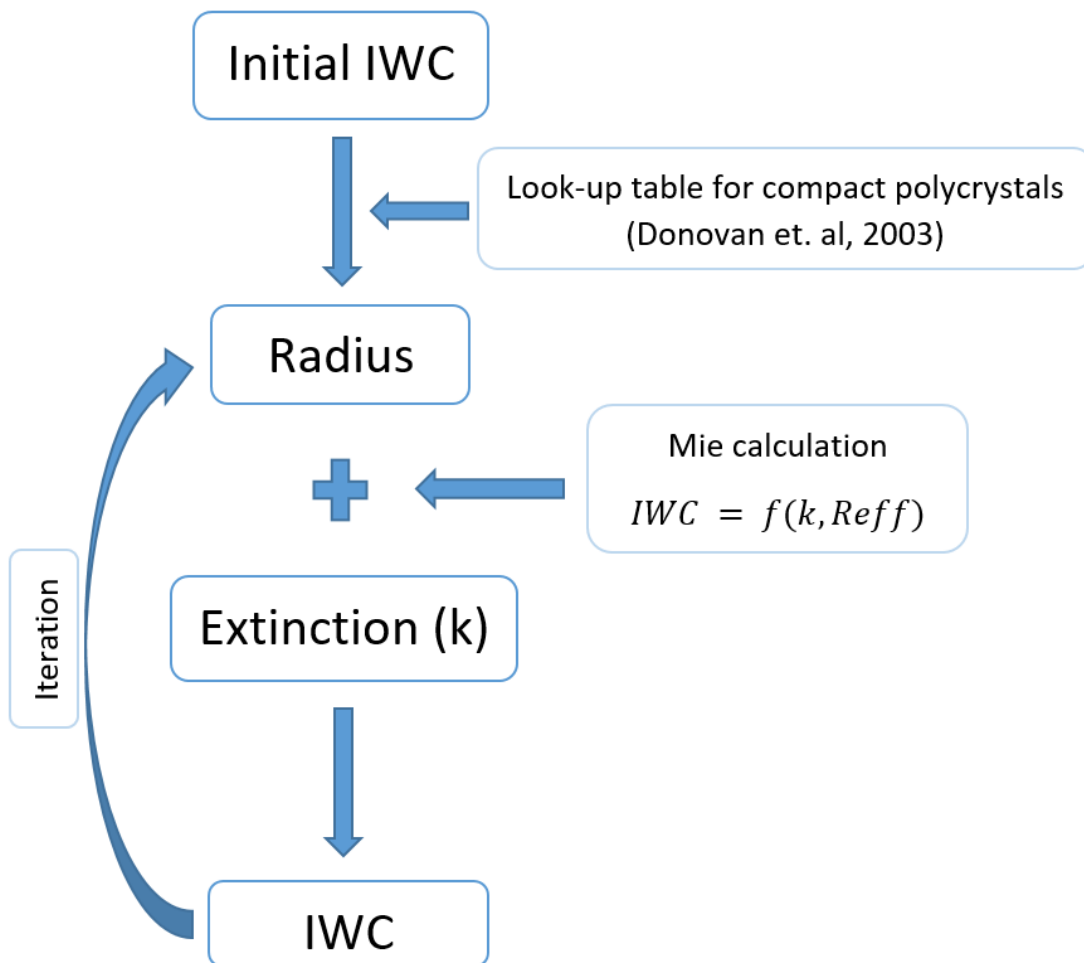
Figure 6.1: Iterative process for the calculation of micro-physical properties: median radius, IWC and limb IWP.

6.3   Ice water content, ice water path and median radius

The comparison of the ERA5-based dataset and the GLORIA observations was done for the clouds that fulfilled the following requirements. First, only thin clouds (i.e with defined CTH and CBH) were selected, since for optically thick clouds the retrieval is not reliable. By definition, the CBH can underestimate the altitude of the bottom of the cloud and be out of the real cloud. Therefore, the CBH is excluded. Second, only grid points in which both observations and ERA5 detected a cloud were selected.
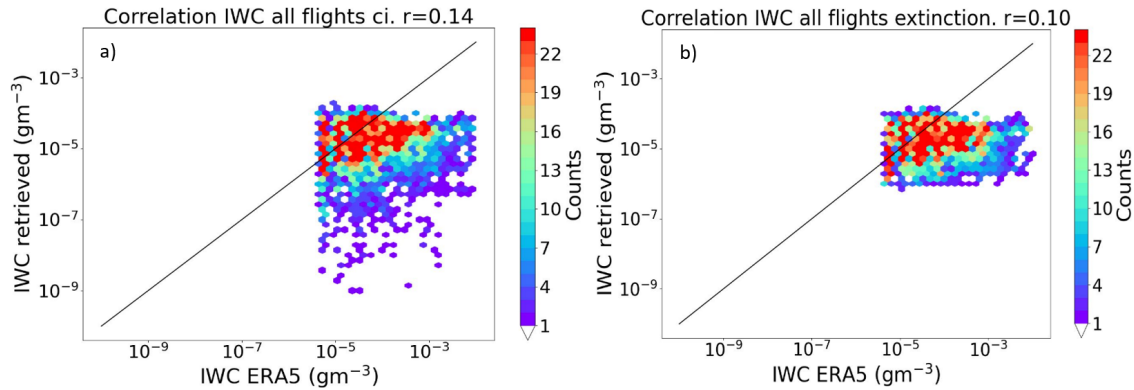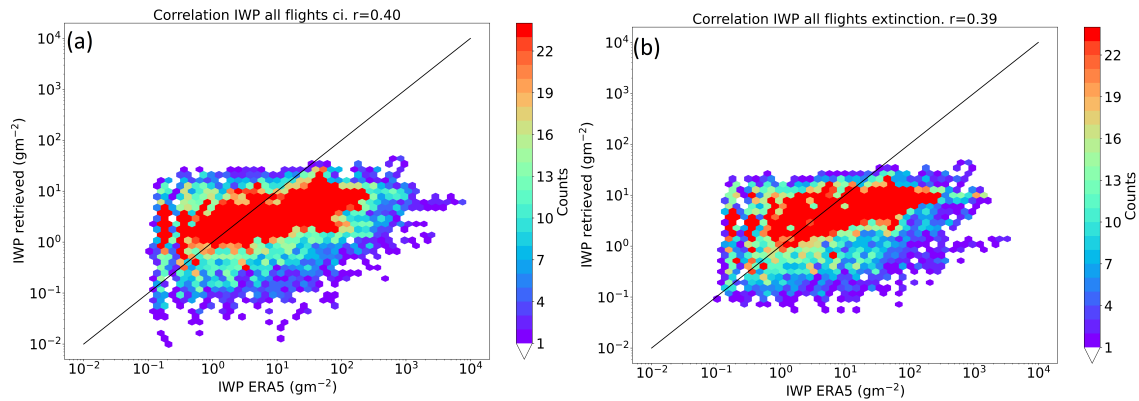
Figure 6.2: Comparison of the ice water content (IWC) from ERA5 and the retrieved IWC from GLORIA for (a) the CI method and (b) the extinction method. Only thin clouds from all flights with occurrence in both datasets are included.

The IWC values discussed in this section correspond to the IWC at the tangent point of the LOS where a cloud is detected. The values for the extinction method range from 1×10^{-6} gm^{-3} to 1×10^{-4} gm^{-3} and for the CI from 1×10^{-9} gm^{-3} to 1×10^{-4} gm^{-3} (Fig. 6.2). The difference in the lower value is explained by the different CBH. The CI method leads to lower CBH with respect to the extinction method, which means, that the tangent points between the higher CBH of the extinction method and the lower CBH of the CI method, have extinction values lower than the extinction threshold. These low extinctions imply lower IWC. As seen in Fig. 6.2, the ERA5 IWC spread from 5×10^{-6} gm^{-3} to 1×10^{-2} gm^{-3}. The lower limit agrees better with the lower limit of the extinction method, which could indicate a better determination of the bottom of the cloud. The upper limit for ERA5 is two orders of magnitude higher than the upper limit of the observations. This could be due to an underestimation of the retrieved IWC, but also because 1×10^{-4} gm^{-3} is the limit where the measurements start to be optically thick in the limb for GLORIA. The correlation between both datasets is low, with only a correlation number of $0.10 - 0.14$. The definition of what is "low" and "high" IWC changes from campaign to campaign, depending on the area of study. For example, during ML-Cirrus, a campaign focused on cirrus at mid-latitudes in Europe, IWC ranges from 1×10^{-5} gm^{-3} to 0.2 gm^{-3} were measured (Luebke et al., 2016). For the campaign SPARTICUS, also in mid-latitudes but over Central USA, the values of IWC fall between 1×10^{-3} gm^{-3} to 0.4 gm^{-3}. ML-Cirrus registered lower values corresponding to in situ origin cirrus in slow updrafts, whereas
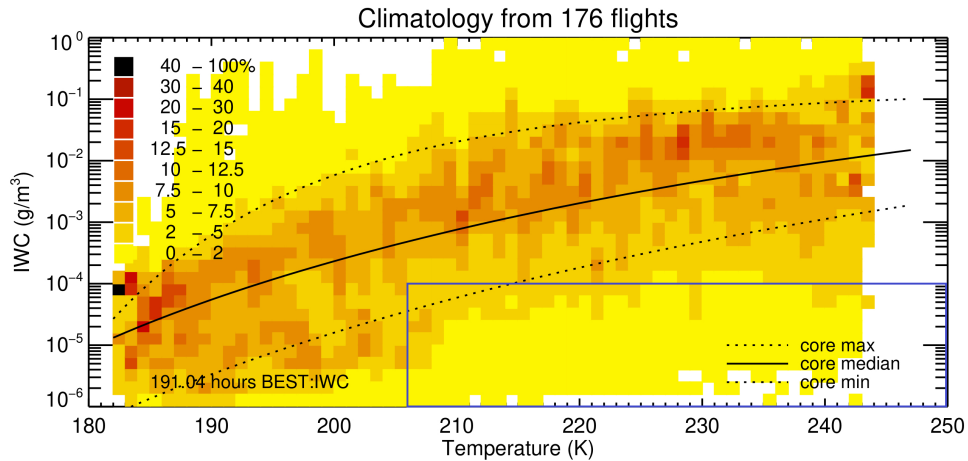
Figure 6.3: Climatology including mid and tropical latitudes of ice water content (IWC) from 176 flights from different campaigns with color code frequency. The x-axis is temperature and is divided in 1 K bins. The blue rectangle indicates the IWC and T range of the GLORIA observations during WISE. Figure adapted from figure by M. Krämer after personal communication.

is missing the larger IWC typical of anvil cirrus. As the analysis presented here focuses on the thin cirrus, it is not expected to reach very high values. The lower limit of the estimated IWC detected with GLORIA is one order of magnitude lower than the offered in the literature (Luebke et al., 2016; Krämer et al., 2016). A more recent study by Krämer et al. (2020), including the observations of about 170 hours of flights across all latitudes, obtained a climatology for IWC with 1×10^{-7} gm^{-3} as the lower limit. The IWC retrieved with GLORIA is within the IWC range provided by Krämer et al. (2020) and it falls into the rarely observed IWC-Temperature combination (Fig. 6.3), which as explained above, could be partially due to an underestimation of the retrieved IWC and to reach saturation in the observations.

The IWC is however, not the ideal parameter to compare with GLORIA, due to the uncertainty in the location of the cloud and the signal being integrated along the LOS. Therefore, it is more useful to compute the limb IWP. As explained in Sect. 3.4, the adequate variables from the ERA5 dataset were sampled according to the measuring geometry of GLORIA. Therefore, IWC for each point along the LOS is obtained for both ERA5-based dataset and GLORIA. The resulting limb IWP for both datasets is the integration of the IWC along the LOS. The retrieved limb IWP for the extinction method

spreads from $5 \times 10^{-2}\,\mathrm{gm^{-2}}$ to $40\,\mathrm{gm^{-2}}$ and for the CI method $1 \times 10^{-2}\,\mathrm{gm^{-2}}$ to $40\,\mathrm{gm^{-2}}$ (Fig. 6.4). The ERA5 limb IWP has a higher lower limit ($1 \times 10^{-1}\,\mathrm{gm^{-2}}$) and an upper limit two orders of magnitude higher ($9 \times 10^{3}\,\mathrm{gm^{-2}}$). In Fig. 6.4 is possible to see how the retrieved IWP saturates for values, which would indicate the maximum limb IWP that GLORIA can retrieved, since there is no sensitivity to higher IWPs. The correlation factor with the ERA5 IWP is about 0.4, which is better than for the IWC comparison.

Figure 6.4: Comparison of the limb ice water path (IWP) from ERA5 and the retrieved limb IWP from GLORIA for (a) the CI method and (b) the extinction method. Only thin clouds from all flights with occurrence in both datasets are included.

As for the particle size, Fig. 6.5 shows the R_{med} for thin cirrus. R_{med} spreads from $5.6\,\mu\mathrm{m}$ to $10.5\,\mu\mathrm{m}$. In coordinates relative to the tropopause, it is possible to observe how R_{med} decreases as it gets closer to the tropopause. In comparison with the climatology from Krämer et al. (2020), the retrieved R_{med} is within the small-middle size ice particles measured in middle-latitudes. This could be an indication of in situ cirrus, which have small ice crystals.

As suggested by Spang et al. (2012) using simulated data, the CI is very well correlated with the ratio IWP/R_{med}. Figure 6.6 shows that this relation exists for the observed data and that the scatter is larger for the very thin conditions (x-axis between 3 and 8). This relation becomes clearer when only an altitude range of CTHs is selected, like shown in Spang et al. (2012) for modelled cirrus cloud scenarios.
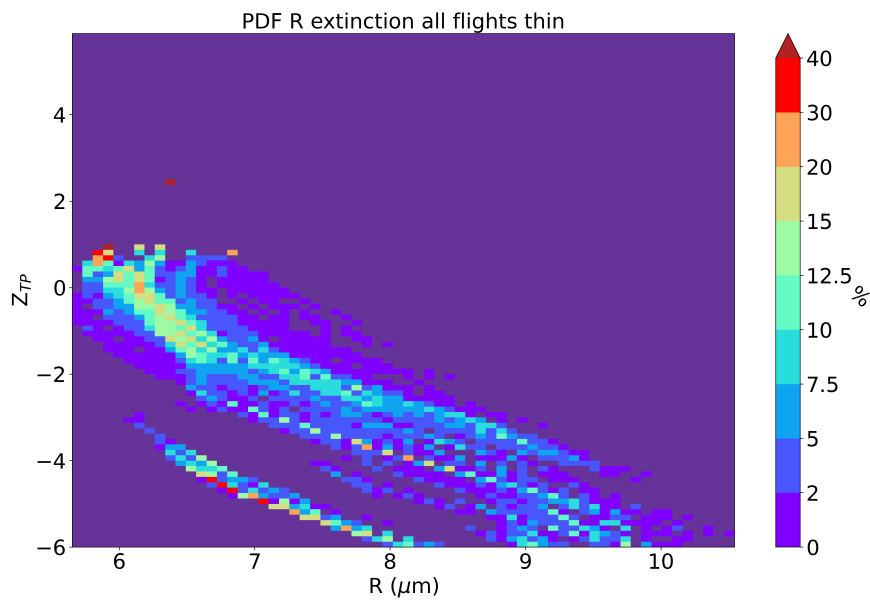
Figure 6.5: Retrieved median radius (R_{med} (μm)) of thin cirrus identified with the extinction method.
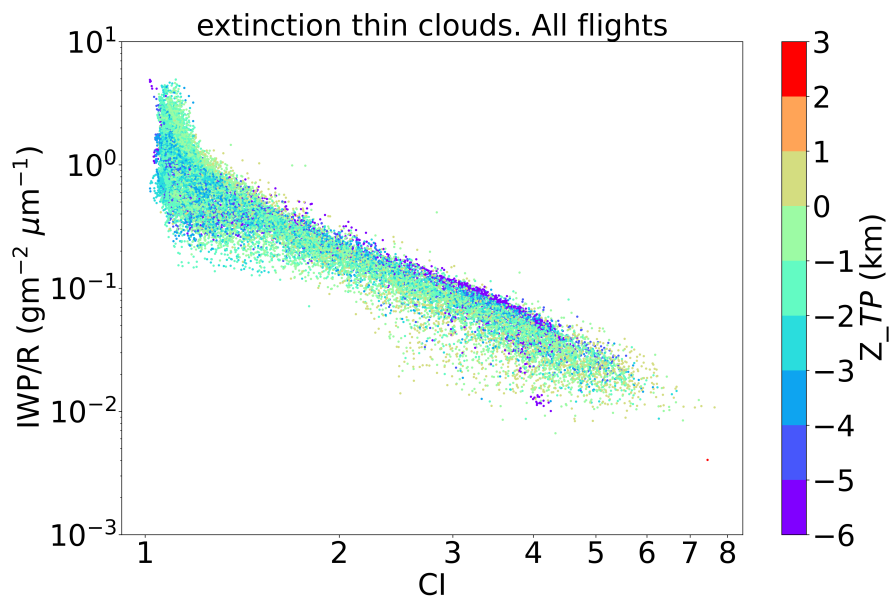
Figure 6.6: Correlation between IWP/R_{med} and cloud index (CI) for thin clouds (detected with the extinction method) for all flights of the WISE campaign. The color code indicates the distance of the CTH to the tropopause (TPmed)).

6.4 Chapter conclusions

A better characterization of the micro-physical properties of cirrus is necessary to improve our understanding of their formation, evolution and feedbacks. The analyzed micro-physical properties in this chapter are IWC, limb IWP and R_{med} for thin clouds. To retrieve these quantities from the observations, two approaches were combined in an iterative procedure: a look-up table by Donovan (2003) for several parameters as function of temperature and IWC, and the relation between extinction coefficient and IWC with particle size. Once the R_{med} and the IWC were estimated for all points along the LOS, the limb IWP was calculated as the integral of the IWC along the LOS. The limb IWP is a more suitable variable to compare with ERA5, since the signal is integrated along the LOS. This method is limited by the assumptions made, such as spherical particles or transforming the effective radius from the look-up table into median radius, since a log-normal distribution is used for the second approach.

The estimated IWC ranges from 1×10^{-6} gm^{-3} to 1×10^{-4} gm^{-3} and for the CI from 1×10^{-9} gm^{-3} to 1×10^{-4} gm^{-3}. The difference in the lower value is explained by the different CBH. The CI method leads to lower CBH with respect to the extinction method, which means that the cloud identified with the CI method has lower extinctions, which implies lower IWC. The lower limit for ERA5 agrees better with the lower limit of the extinction method, which could indicate a better determination of the bottom of the cloud. The upper limit for ERA5 is two orders of magnitude higher than the upper limit of the observations. This could be due to an underestimation of the retrieved IWC and the observations reaching saturation. The IWC is however, not the ideal parameter to compare with GLORIA, due to the uncertainty in the location of the cloud and the signal being integrated along the LOS. This is evidenced by the low correlation with the IWC from the ERA5-based dataset for both methods ($0.10 - 0.14$). It is more useful to compute the limb IWP. The retrieved limb IWP for the extinction method spreads from 5×10^{-2} gm^{-2} to 40 gm^{-2} and for the CI method 1×10^{-2} gm^{-2} to 40 gm^{-2}. These numbers agree better with the limb IWP from ERA5 and the correlation between both datasets is better than for the IWC (about 0.4). The retrieved R_{med} ranges from $5.6\,\mu$m to $10.5\,\mu$m, which would

correspond to small-middle size ice particles in mid-latitudes according to the climatology of Krämer et al. (2020).

Chapter 7

CLaMS-Ice: case studies

In this chapter, the results from the comparison of the GLORIA observations with the model CLaMS-Ice (Chemical Lagrangian Model of the Stratosphere) are presented. As the model computes backward trajectories starting from a certain air parcel, and then runs forward trajectories, it is possible to gain insight into the origin of the cirrus and determine if they are of liquid origin (origin T > 235 K) or in situ origin (T < 235 K; see Sect. 2.2). Two optically and vertically thin cirrus (one in flight 3 and one in flight 16) with cloud tops at or above the tropopause, that were not represented by the ERA5 dataset, were selected as case studies. In Sect. 7.1 the model and the set up used for the simulations are described. The results are explained in Sect. 7.2 and Sect. 7.3.

7.1   CLaMS-Ice: description and setup

To examine the origin of the observed cirrus clouds, first backward trajectories starting in the area of observation were run with CLaMS-Ice, followed by simulating ice microphysics along the trajectories in forward direction. CLaMS (Chemical Lagrangian Model of the Stratosphere) is a modular chemistry transport model developed at the Forschungszentrum Jülich (IEK-7), Germany. The main four modules are: the trajectory module, the chemistry module, the Lagrangian mixing module and the Lagrangian sedimentation scheme. In a later stage, CLaMS was expanded into three dimensions. CLaMS is widely used in the research of UTLS processes and also during the planning of aircraft field

campaigns, since it allows the forecast of variables with scientific interest in a determined area, helping to optimize the flight planning. CLaMS is well documented, more information can be found in, e.g. McKenna et al. (2002a), McKenna et al. (2002b) and Konopka et al. (2004).

The model used in this thesis was CLaMS-Ice (Luebke et al., 2016; Baumgartner et al., 2021), which combines the trajectory module of CLaMS with a double moment bulk microphysics scheme (cirrus bulk model). CLaMS-Ice serves as a large-scale cirrus analysis and forecast tool. The two moments predicted are the mass and the number of ice crystals. The two moments scheme used in CLaMs-Ice is described in detail in Spichtinger and Gierens (2009). The model includes all mechanisms relevant for cirrus formation and evolution: homogeneous and heterogeneous ice nucleation, deposition growth, sublimation, sedimentation and aggregation of ice crystals (Sect. 2.2).

MODEL INITIALIZATION AND SETUP

Specific setups can be defined in CLaMS-Ice, depending on the purpose of the simulation. The input parameters are: small-scale temperature fluctuation superimposed on the reanalysis temperatures along the trajectories, time resolution, number of days for the backwards calculations, type of nucleation, deposition, aggregation, sedimentation strength, initial specific humidity and values for the heterogeneous ice nucleation parametrization (ice nucleating particle (INP), mean concentration and freezing humidity). Temperature fluctuations refer to the altitude fluctuations of isentropes caused by atmospheric waves and depend on season, latitude, topography and altitude. The importance of having a proper characterization of this phenomenon lies in their importance for the modeling of micro-physical processes along Lagrangian trajectories. During the ice nucleation phase, even small changes in the RH_{ice}, triggered by temperature fluctuations, strongly impact the final ice crystal concentrations. The used parametrization is based on the parametrization for tropical latitudes by Podglajen et al. (2016) based on balloon observations and a stochastic model. The authors proposed a simple parametrization of the wave-induced temperatures and heating cooling rates, in which a power law describes the behavior of potential and kinetic energy spectra. This parametrization for the

tropics was adapted for mid-latitudes (personal communication with Aurelien Podglajen and Christian Rolf). The freezing humidity at which the heterogeneous ice nucleation starts is in most cases set to RH_{ice} = 120 % and the distribution of INPs is described by a log-normal distribution randomly generated and centered at the given initial mean concentration of INPs. The selected values for the initial INP concentration are: $10\,m^{-3}$, $5 \times 10^3\,m^{-3}$ and $2 \times 10^4\,m^{-3}$. According to DeMott et al. (2003), INP concentrations between $5 \times 10^3\,m^{-3}$ to $2 \times 10^4\,m^{-3}$ are typically found in measurements in the mid-latitude upper troposphere. For the lower INP concentration ($10\,m^{-3}$) there is no reference in the literature available (sparse number of observations at the UTLS for INP concentrations), but it was chosen to investigate the relevance of heterogeneous and homogeneous ice nucleation at the UTLS under clean environmental conditions. The initial concentration of aqueous solution particles for triggering of homogeneous nucleation is set to $3 \times 10^8\,m^{-3}$. The ice deposition process is activated during the simulations, but not the aggregation. The sedimentation factor is set at 0.97, based on comparisons between measurements and simulations performed by Costa (2017). This parameter parameterizes ice particles that sediment and fall out of an air parcel by ice particles that have fallen into it from above. A sedimentation factor of zero means that no ice particle is replaced, whereas a factor of 1 indicates that all ice particles have precipitated. The time steps during the simulation can vary, depending on the conditions, to save computation time. For cloud-free air parcels with RH_{ice} < 100 % for the current and the next step, the model increases the time step to 10 minutes. When the RH > 100 % but it is not expected that a cloud form in the next interval, the time step is reduced to 1 minute. When clouds are present, the time step is 1 second. If the threshold for homogeneous ice nucleation is close, the time step is reduced to 0.1 seconds. In case of sublimating and sedimenting ice crystals, the time step increases.

The CLaMS backward trajectories are computed based on hourly ERA5 temperature, pressure and wind fields. The vertical coordinate in CLaMS-Ice is zeta, a hybrid coordinate that changes from pressure coordinates to potential temperature coordinates depending on the region of the atmosphere. The length of the backward trajectories is

different for each air parcel, since the cold point (CP), i.e the time with the lowest temperature, was chosen as initial time for simulations along the forward trajectories. The CP was determined after running CLaMS 10 days backwards. When the CLaMS-Ice simulation starts, RH_{ice} (the parameter controlling ice formation and evolution) is computed from the respective temperature and pressure in each time step. If the trajectory originates at a temperature higher than 238 K, the model starts at the time when the temperature falls below 238 K. If a cloud is predicted by ERA5 at the start point of a trajectory, its IWC is used to characterize it, following the Boudala et al. (2002) parametrization that calculates the ice particle number. This cloud is called in the model "pre-existing ice" and is treated as any cloud formed later.

CLOUD POSITION APPROACH

For the CLaMS-Ice simulation of cirrus clouds observed by the GLORIA instrument one difficulty is that, as explained in Sect. 2.4, the specific position of the observed clouds is not exactly known. This complicates a one-one model-observations comparison. One approach to overcome this problem is to define an area where the trajectories should end that encloses the latitude-longitude coordinates of the tangent points of the LOS for which a cloud signal was detected. Another approach, used for the study case of flight 16, is to chose the points along the LOS as the ending points of the forward trajectories. This option is more accurate, as it follows the measuring geometry. However, it is computationally more expensive and is only used in the case of a cloud that covers a few LOS.

7.2   Case study: flight 3

On the 18th of September 2017, the second scientific flight (F03) of the WISE campaign was conducted with the main objective of sampling a tropospheric air mass between Greenland and Norway and probing the edge structure of this air mass (region of the air mass where the PV gradient is large). During this flight, between $11:00 - 11:46$ UTC a cloudy area was identified north of Iceland in an altitude region between $12 - 13$ km. The CTHs of this cloud were detected above the TP_{med} (≈ 400 m) and around the TP_{95}. The

maximum extinction for this cloud is $3.3 \times 10^{-3}\,\text{km}^{-1}$ and its vertical extent ranges from $0.25\,\text{km}$ to $0.75\,\text{km}$ (Fig. 7.1).
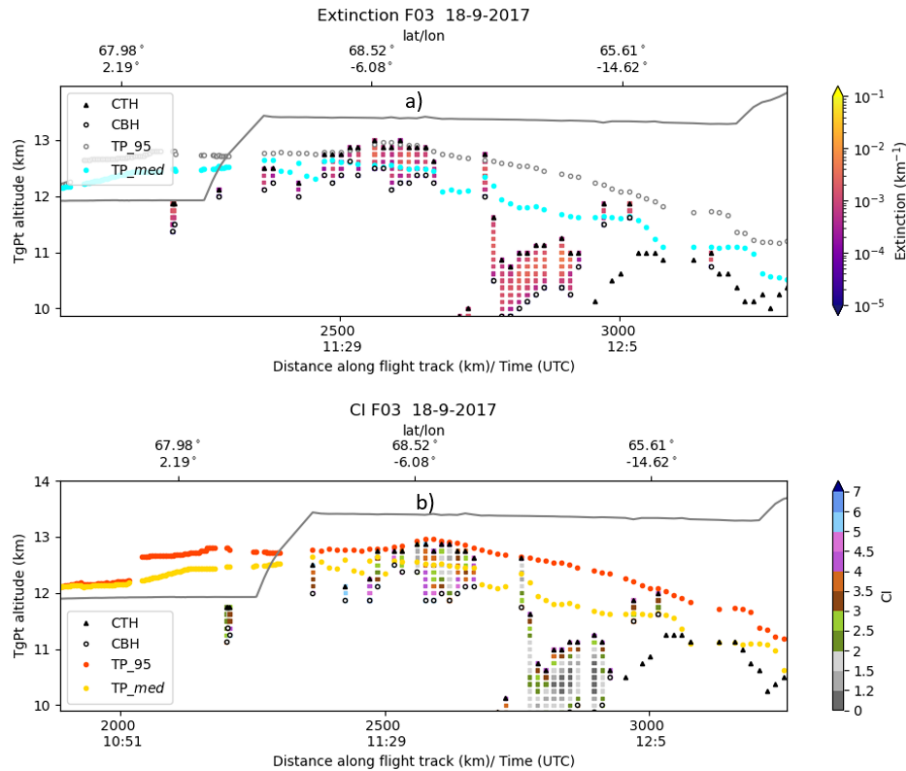
Figure 7.1: Zoomed area of the cross-section of flight F03 on the 18 of September 2017 focusing on the thin cirrus above the tropopause at around 12:00 UTC. (a) Extinction coefficient color scale. Median tropopause (TP$_{med}$) and the percentile 95 of the tropopause (TP$_{95}$) are indicated with blue dots and grey dots, respectively. (b) Cloud index (CI) color scale. Median tropopause (TP$_{med}$) and the percentile 95 of the tropopause (TP$_{95}$) are indicated with yellow dots and orange dots, respectively. Black triangles indicate the CTHs and the white circles the CBHs. The grey line marks the flight trajectory. The altitude of the tangent points (TgPt) is the y-axis.

As explained in the introduction of this chapter, a direct comparison between the model and the observations is challenging due to the uncertainty in the cloud location. Therefore, as an input for the model a box was defined. The longitude was between $15° - 3°$W and the latitude between $66° - 71°$N with a resolution of 1 degree. The altitude grid extended from $11.5\,\text{km}$ to $13.5\,\text{km}$ in steps of $125\,\text{m}$. The upper limit of the given altitude range was higher than the detected CTH to address the possibility of the cloud being located at higher levels.

Figure 7.2 shows an example of the backward and forward trajectory of a single air

parcel for the INP scenario $2 \times 10^4 \, \text{m}^{-3}$. The lower panel shows the backward trajectory using the data from ERA5 (IWC and T) as input every 24 hours. The backward trajectory starts at 12:00 UTC on the 18 of September 2017 and ends at the CP. The CP temperature is then the input for the forward trajectory (upper and middle panels), together with the IWC. If IWC $\neq 0$, then it is indicated as pre-existing (IWC-pre). The example shows the formation of clouds by different ice nucleation processes. When the RH$_{ice}$ is $\approx$ 150 %, homogeneous ice nucleation occurs, reaching $\approx 3 \times 10^{-3} \, \text{gm}^{-3}$. Then, the RH$_{ice}$ decreases, staying high enough to start the heterogeneous ice nucleation. As the temperature increases, the cloud evaporates. Towards the end of the trajectory, the RH$_{ice}$ increases and optically very thin clouds (IWC $\approx 2 \times 10^{-6} \, \text{gm}^{-3}$) at around 12.5 km are formed.

Fig. 7.3 shows the IWC produced along the CLaMS-Ice trajectories for the three INP concentrations. Fig. 7.3 indicates that CLaMS-Ice was able to form cirrus in the region of the GLORIA observations for all predefined INP concentrations. The main difference is that the larger the number of INPs, the larger is the number of parcels with cirrus and the larger the portion of IWC from heterogeneous ice nucleation, as each INP forms an ice particle. Since the cloud was measured during a extended period of time (approximately 45 minutes), only trajectories in which there is IWC at any time during the last hour of the calculation are represented. The cloud was formed in situ (T < 235K), after the air parcels ascended, experiencing a decrease in temperature and an increase in RH$_{ice}$. In the formation of this cloud, the local dynamical processes played a fundamental role. The region was dominated on a synoptic scale by the anti-cyclonic circulation. On the mesoscale, the air mass experienced vertical movements as a consequence of convergence together with potential gravity wave activity (personal communication with D. Kunkel, JGU Mainz). The potential temperature along the trajectories stayed constant with very small perturbations when the cloud was formed. The temperature ranged from 193 K to 223 K. The RH$_{ice}$ reached values high enough (maximum RH$_{ice}$ of 160 %) for the homogeneous ice nucleation to occur. As the freezing RH$_{ice}$ of homogeneous ice nucleation is higher than for heterogeneous, heterogeneous IWC is more frequent: in case of higher INP concen-
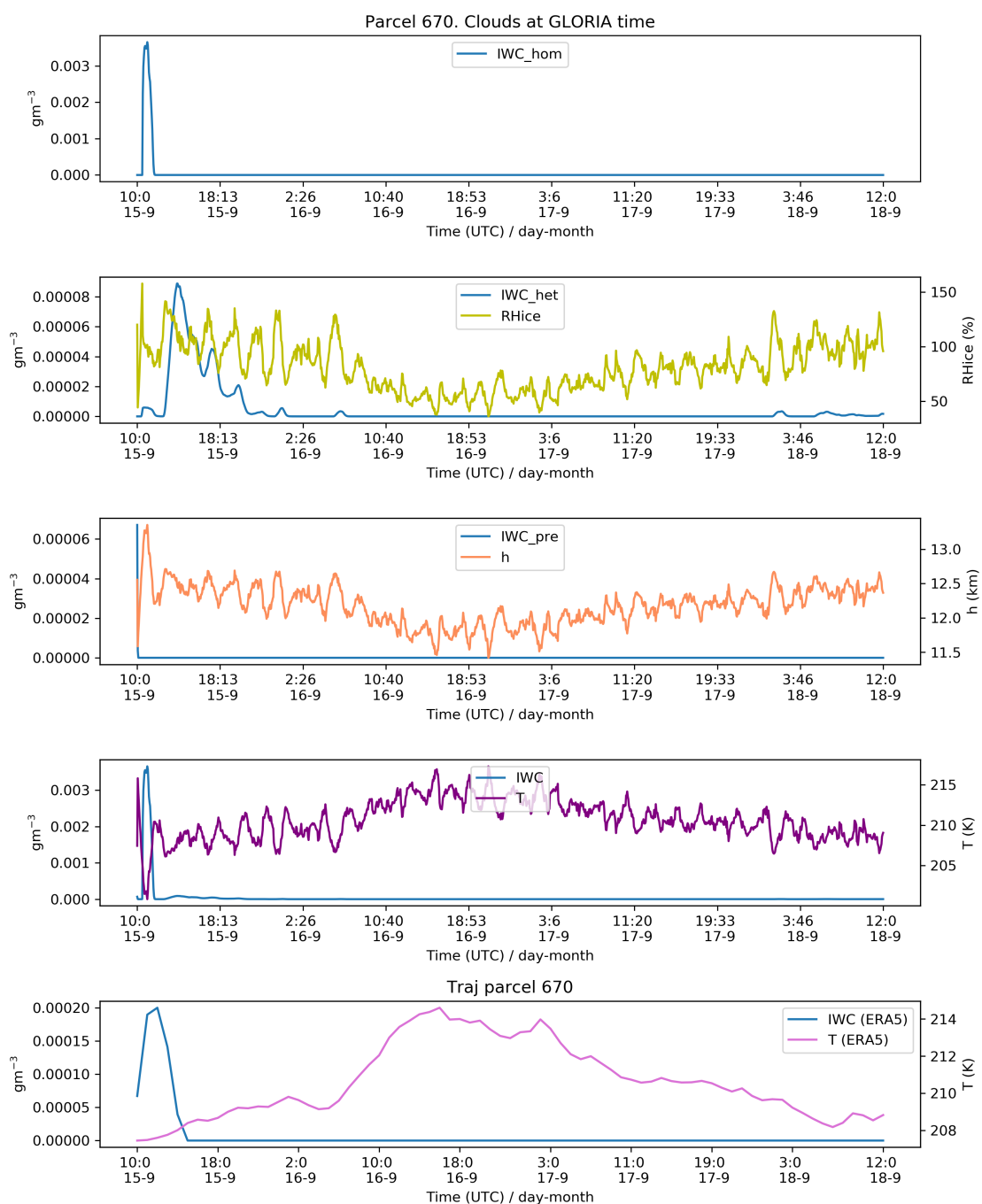
Figure 7.2: Example of backward trajectory (lower panel) computed with CLaMS-Ice for the scenario with ice nuclei particle (INP) . Temperature (T) and IWC are indicated by the green and pink line, respectively. The upper and the middle panels correspond to the forward trajectory. From top donwards: first panel represents homogeneous IWC (IWC_hom); second panel represents heterogeneous IWC (IWC_het) in blue and relative humidity with respect to ice (RH_ice) in green; third panel represents pre-existing ice (IWC_pre) in blue and altitude (h) in orange; fourth panel represents the total IWC (in blue) and T (in purple) from ERA5. The x-axis is time.

tration, more water is depleted by the many heterogeneously formed ice crystals, so that the homogeneous ice nucleation rate is weakened or the homogeneous freezing RH_{ice} is not even reached. However, once triggered, the homogeneous IWC often reaches higher values, especially at the beginning of the homogeneous ice nucleation. The homogeneous IWC has a maximum of $\approx 2 \times 10^{-5}\,gm^{-3}$ for all predefined INP concentrations, whereas the maximum heterogeneous IWC is $\approx 3 \times 10^{-6}\,gm^{-3}$ for the two higher INP concentrations and $5.6 \times 10^{-9}\,gm^{-3}$ for the lowest INP. The difference of almost three orders of magnitude between the maximum heterogeneous IWC, evidences the relation higher INP concentration, more heterogeneous ice nucleation. The maximum of the total IWC increases slightly from $4 \times 10^{-3}\,gm^{-3}$ for INP = $1 \times 10^{1}\,m^{-3}$, to $6 \times 10^{-3}\,gm^{-3}$ for a INP concentration of $2 \times 10^{4}\,m^{-3}$.

As discussed in Sect 6.3, IWC is not the optimal parameter for comparisons with GLORIA, however, it is useful as a reference for the performance of the model and the retrieval. When the IWC of the CLaMS-Ice trajectories is compared with the retrieved IWC (at the tangent point of the LOS) from the observations (Fig. 7.4), the INP concentrations that fit best are the INP $5 \times 10^{3}\,m^{-3}$ and $2 \times 10^{4}\,m^{-3}$, as the retrieved IWC is centered with the maximum of the distribution of the simulated IWC.
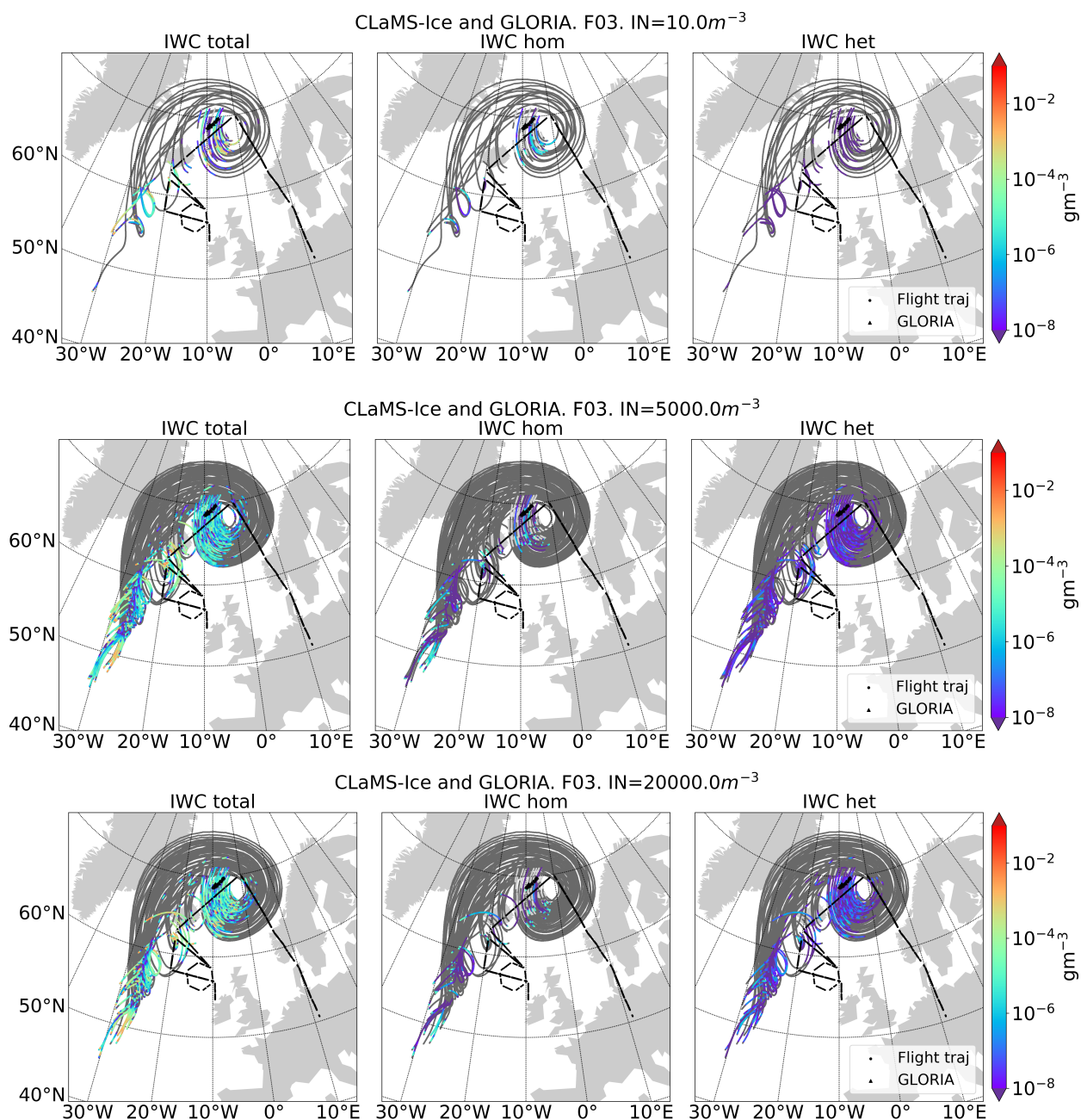
Figure 7.3: CLaMS-Ice trajectories for the case study of F03 of the WISE campaign. The colored part of the trajectories represent the locations where cirrus clouds are simulated, color code is ice water content (IWC). From left to right, the panels show: total IWC, homogeneous IWC and heterogeneous IWC (gm^{-3}) for (upper row) ice nuclei particle concentration (INP) of $10\,m^{-3}$, (middle row) INP of $5 \times 10^3\,m^{-3}$ and (lower row) INP of $2 \times 10^4\,m^{-3}$. The black triangles represent the tangent points of the LOS for which GLORIA observed a cloud. The black dots indicate the parts of the flight path in which GLORIA took measurements. The dark grey line represent the part of the backwards trajectories where no IWC was produced. The light grey parts indicate the last hour of the trajectories.

Figure 7.4: Histogram for the total IWC of the CLaMS-Ice trajectories with formation of a cloud during the last hour of the trajectory (in red) and histogram of the retrieved IWC at the tangent point of the LOS where the selected cirrus is detected (in blue). a) Ice nuclei particle concentration (INP) of $1 \times 10^1 \, \text{m}^{-3}$; b) INP of $5 \times 10^3 \, \text{m}^{-3}$ and c) INP of $2 \times 10^4 \, \text{m}^{-3}$. The x-axis is the logarithm of the IWC. The y-axis indicated the number of occurrences.

7.3 Case study: flight 16

On the 21th of October 2017, the sixteenth scientific flight took place. The main objective of this flight was investigating a breaking Rossby wave and related mixing of air masses. During this flight two cloudy regions with very low extinctions and CTHs above the TP_{med} were identified (Fig. 7.5). One of them, observed between 8:12 UTC and 8:19 UTC at altitudes between 11 km to 11.5 km (500 m above the TP_{med}) was selected for a closer examination. The maximum measured extinction is 5×10^{-3} km^{-1} and its vertical extent of about 500 m. To investigate the origin of this cloud with the model, first, a box with longitude $5° - 8.25°$E, latitude $70° - 72.25°$N ($0.25° \times 0.25°$) and altitude $11 - 12.125$ km (resolution 125 m) was defined.

The results (Fig. 7.6) are similar to the previous case study. However, in the current case the backwards trajectories reached the CP close to the location of the cirrus, which indicates that the mixing occurred very recently. The temperature during the last 24 hours was lower than 235 K, which means that the cloud is of in situ origin. For all INP scenarios, CLaMS-Ice produced clouds, with the larger INP concentration having the larger number of parcels where a cirrus formed. Again, the heterogeneous ice nucleation occurs more often than the homogeneous ice nucleation, as discussed in Sect. 7.2. In comparison with the case study of F03, the altitude of the cirrus in F16 is lower, as well as the homogeneous freezing RH_{ice}, with a maximum of about 158 %. For the current case study, when comparing the simulated IWC with the retrieved IWC, the most probable scenarios would be INP $= 5 \times 10^3$ m^{-3} and the highly polluted with INP $= 2 \times 10^4$ m^{-3}. The clean environment, i.e., INP $= 1 \times 10^1$ m^{-3} is discarded, as it is centered at lower IWC.

Another method used to analyze this case study, was to chose the points along the LOS as the ending points of the forward trajectories. However, with this approach only a few trajectories formed a cloud between 11 and 11.125 km at the ending point or close to it. The reason is that the LOS approach uses very specific coordinates, with no margin for the model to produce clouds in the vicinity. Therefore, the box approach is more flexible and more suitable to test if the model can form clouds in a determined region.
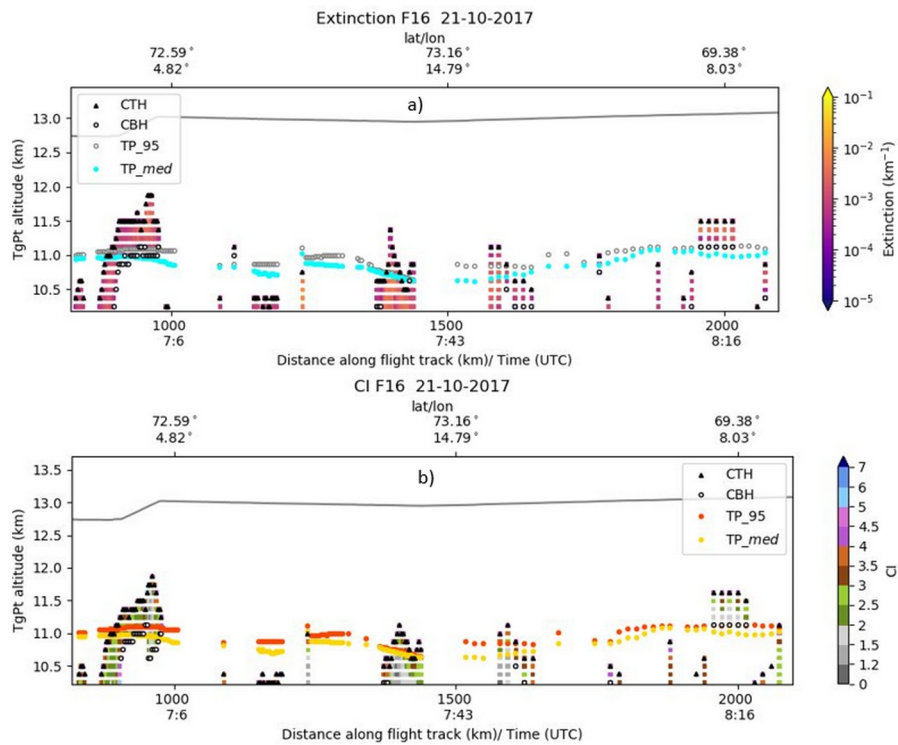
Figure 7.5: Zoomed area of the cross-section of flight F16 on the 21st of October 2017 focusing on the thin cirrus above the tropopause before at 8:15 UTC. (a) Extinction coefficient color scale. Median tropopause (TP_{med}) and the percentile 95 of the tropopause (TP_{95}) are indicated with blue dots and grey dots, respectively. (b) Cloud index (CI) color scale. Median tropopause (TP_{med}) and the percentile 95 of the tropopause (TP_{95}) are indicated with yellow dots and orange dots, respectively. Black triangles indicate the CTHs and the white circles the CBHs. The grey line marks the flight trajectory. The altitude of the tangent points (TgPt) is the y-axis.

Even though the comparison between the model and the observations is not exact, due to the uncertainty in the cloud location, it is a success that CLaMS-Ice is able to form very thin clouds close to the tropopause and to give information about the ice nucleation processes. This proves, that input data with higher resolution (ERA5 in this study) and improved parametrizations of the temperature fluctuations lead to better performance of the micro-physical models.
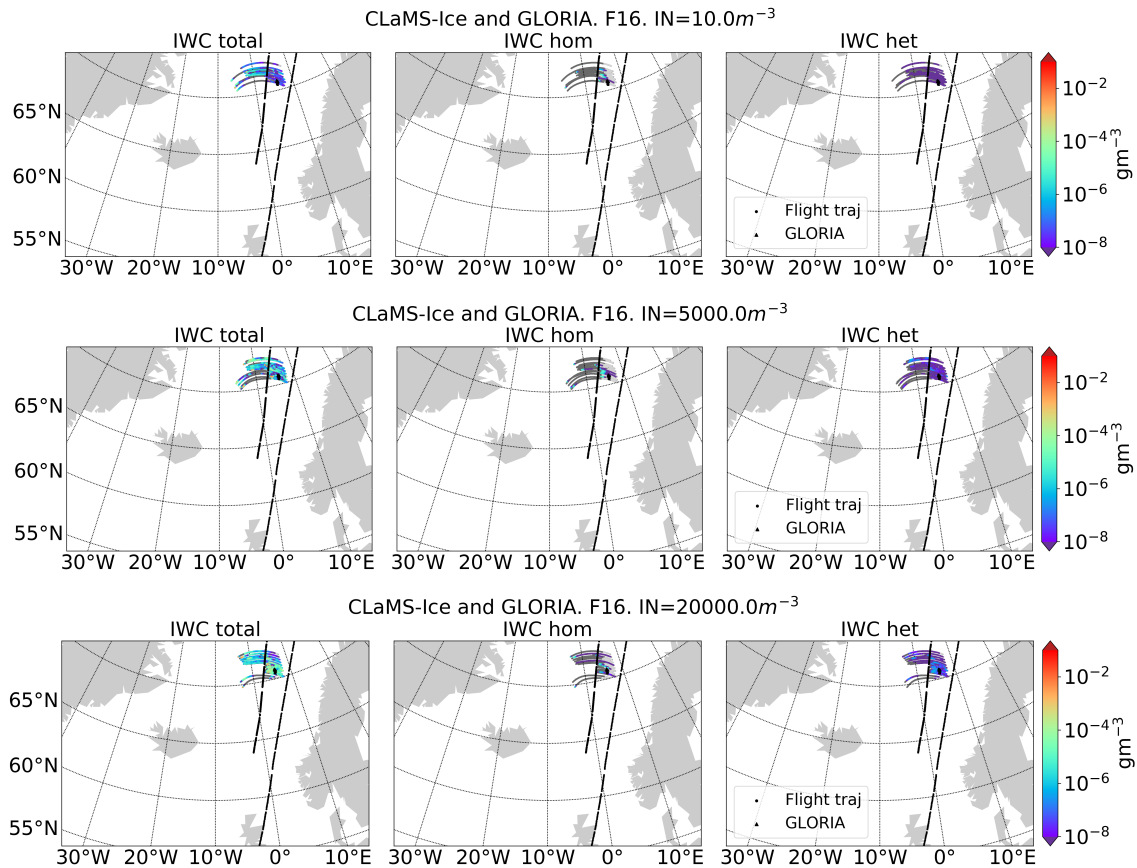
Figure 7.6: CLaMS-Ice trajectories for the case study of F16 of the WISE campaign. The colored part of the trajectories represent the locations where cirrus clouds are simulated, color code is ice water content (IWC). From left to right, the panels show: total IWC, homogeneous IWC and heterogeneous IWC (gm^{-3}) for (upper row) ice nuclei particle concentration (INP) of $10\,\text{m}^{-3}$, (middle row) INP of $5 \times 10^3\,\text{m}^{-3}$ and (lower row) INP of $2 \times 10^4\,\text{m}^{-3}$. The black triangles represent the tangent points of the LOS for which GLORIA observed a cloud. The black dots indicate the parts of the flight path in which GLORIA took measurements. The dark grey line represent the part of the backwards trajectories where no IWC was produced. The light grey parts indicate the last hour of the trajectories.

Figure 7.7: Histogram for the total IWC of the CLaMS-Ice trajectories with formation of a cloud during the last hour of the trajectory (in red) and histogram of the retrieved IWC at the tangent point of the LOS where the selected cirrus is detected (in blue). a) Ice nuclei particle concentration (INP) of $1 \times 10^1 \, \text{m}^{-3}$; b) INP of $5 \times 10^3 \, \text{m}^{-3}$ and c) INP of $2 \times 10^4 \, \text{m}^{-3}$. The x-axis is the logarithm of the IWC. The y-axis indicated the number of occurrences.

7.4 Chapter conclusions

Two case studies of cirrus with CTHs above the tropopause were selected to be simulated with CLaMS-Ice. First, backward trajectories starting in the area of study were computed, followed by simulating the microphysics along the trajectories in the forward direction. To simulate different scenarios, three ice nuclei particle (INP) concentrations were predefined: $10\,\mathrm{m^{-3}}$ (clean environment), $5 \times 10^3\,\mathrm{m^{-3}}$ and $2 \times 10^4\,\mathrm{m^{-3}}$ (highly polluted environment). For all scenarios, clouds were formed in situ (T < 235 K) in the region of study. As the freezing $\mathrm{RH_{ice}}$ of homogeneous ice nucleation is higher than for heterogeneous, heterogeneous IWC is more frequent. However, once triggered, the homogeneous IWC often reaches higher values, especially at the beginning of the homogeneous ice nucleation. For both case studies the more probable scenarios are INP concentrations of $5 \times 10^3\,\mathrm{m^{-3}}$ and $2 \times 10^4\,\mathrm{m^{-3}}$ and not the INP concentration for a very clean environment. Even though the comparison between the model and the observations is not exact, due to the uncertainty in the cloud location, it is an important milestone that CLaMS-Ice was able to form very thin clouds close to the tropopause and provide information about the ice nucleation processes.

Chapter 8

Summary

This chapter summarizes the main results regarding the four main scientific questions that were presented in the introduction.

1. What are the macro-physical properties of cirrus clouds at mid-latitudes, i.e., cloud top and bottom height, vertical extent?

This thesis includes an analysis of cirrus cloud observations taken with the IR limb sounder GLORIA on board of the research aircraft HALO during the WISE campaign. Two identification methods were defined to detect clouds in the measurements: the cloud index and the retrieved extinction coefficient. The analysis focused on high cirrus clouds close to the tropopause and excluded multi-layer clouds. The extinction method indicated very thin clouds with an extinction as low as $2 \times 10^{-4}\,km^{-1}$. Both methods are in good agreement, having similar frequencies of occurrence and similar CTHs. For the extinction method 61 % of all observed profiles show cirrus clouds and 59 % for the CI. This frequencies of occurrence are also in agreement with the ERA5-based dataset, for which the fraction of detected CTHs is 59 %. The CTHs range from 8 km to $\approx$14 km, being the cloud tops more frequently detected at $\approx$11.5 km. From all considered profiles (13539), about 39 % (5232 profiles) become optically thick using the extinction and 41 % (5517 profiles) the CI method. 36 % of all profiles become optically thick for both methods. For both methods, a large fraction of the optically thin cirrus clouds were located between $45 - 65°N$ and had a vertical extent smaller than 1.5 km (31 % of the clouds detected with

the extinction method and 20 % of the clouds detected with the CI method). The main differences are the slightly higher CTHs of the CI method and the more accurately CBHs identified by the extinction method.

2. Do clouds or even complete cloud layers appear above the tropopause? How frequently? In which meteorological situations?

For studying the presence of cloud tops above the tropopause two approaches were used. First, the median tropopause from ERA5 along the LOS of the GLORIA instrument and second, a more conservative criteria using the percentile 95. Similar tropopauses were considered as an indication of homogeneous air masses. The frequency of occurrence above the tropopause varied from 27 % to 16 % for the CI and from 24 % to 13 % for the extinction method, where the differences between both approaches were due to LOS scenes with heterogeneous tropopause heights.

The high vertical resolution of GLORIA together with the better and more accurate knowledge of the tropopause by using ERA5 instead of previous re-analysis allow a more precise answer if ice clouds form above the mid-latitude tropopause. The results presented in this thesis support the higher occurrence frequencies reported in the literature (Goldfarb et al., 2001; Spang et al., 2015; Zou et al., 2020) in contrast to lower frequencies derived from CALIPSO (Pan and Munchak, 2011; Zou et al., 2020) at mid-latitudes. Using the same criterion as in Spang et al. (2015); Zou et al. (2020), i.e. 0.5 km above the tropopause, the frequency of occurrence is 4 % − 7 %. Since the used dataset is ERA5, which has a higher vertical resoltuion, when considering 250 m above the tropopause, the fraction increases to 13 % − 17 %. This means, that when the uncertainty of the tropopause estimate and the measurements is smaller, like for the GLORIA cloud measurements, the stratospheric cirrus cloud occurrence are even higher. Additionally, an analysis using the dynamical tropopause was performed, leading to occurrence frequencies between 18 % − 21 %.

1.5 km below the tropopause both identification methods present good agreement with the clouds indicated by the ERA5-based dataset, when taken the observation geometry of GLORIA into account. However, it is important to highlight, that the observed

frequency of occurrence of cloud tops close to and above the tropopause is about 50 % higher than indicated by ERA5, which evidences that the thinner clouds close to the tropopause are missing in the re-analysis. CBHs above the tropopause were found, but they were within the uncertainties. Consequently, the GLORIA WISE campaign data cannot confirm the presence of unattached cirrus layers above the first thermal tropopause, but can confirm the presence of cirrus clouds at the tropopause with CTHs penetrating well into the lower stratosphere. Cirrus with CTHs above the tropopause were found related to fronts, to Rossby waves and to WCBs. One cloudy region was located over an anti-cyclone. On the mesoscale, the air mass experienced vertical movements as a consequence of convergence together with potential gravity wave activity. This is an example of the importance of local dynamical processes in the formation of clouds.

3. Is it possible to retrieve micro-physical properties of cirrus clouds from GLORIA, i.e., IWC and particle size?

The analysis of micro-physical properties included a first estimation of the IWC, limb IWP and R_{med} for thin clouds. To retrieve these quantities from the data, two approaches were combined in an iterative procedure: a look-up table by Donovan (2003) for several parameters as function of temperature and IWC, and the relation between extinction coefficient and IWC with particle size. Once the R_{med} and the IWC were estimated for all points along the LOS, the limb IWP was calculated as the integral of the IWC along the LOS. The limb IWP is a better quantity to compare with ERA5, since the signal is integrated along the LOS. This method is limited by the assumptions made, such as spherical particles or transforming the effective radius from the look-up table into median radius, since a log-normal distribution is used for the second approach.

The estimated IWC ranges from $1 \times 10^{-6}\,\mathrm{gm^{-3}}$ to $1 \times 10^{-4}\,\mathrm{gm^{-3}}$ and for the CI from $1 \times 10^{-9}\,\mathrm{gm^{-3}}$ to $1 \times 10^{-4}\,\mathrm{gm^{-3}}$. The difference in the lower value is explained by the different CBH. The CI method leads to lower CBH with respect to the extinction method, which means that the cloud identified with the CI method has lower extinctions, which implies lower IWC. The correlation with the IWC from the ERA5-based dataset is low for both methods ($0.10 - 0.14$). The lower limit for ERA5 agrees better with the lower limit

of the extinction method, which could indicate a better determination of the bottom of the cloud. The upper limit for ERA5 is two orders of magnitude higher than the upper limit of the observations. This could be due to an underestimation of the retrieved IWC and the observations reaching saturation. The IWC is however, not the ideal parameter to compare with GLORIA, due to the uncertainty in the location of the cloud and the signal being integrated along the LOS. Therefore, it is more useful to compute the limb IWP. The retrieved limb IWP for the extinction method spreads from $5 \times 10^{-2}\,\mathrm{gm}^{-2}$ to $40\,\mathrm{gm}^{-2}$ and for the CI method $1 \times 10^{-2}\,\mathrm{gm}^{-2}$ to $40\,\mathrm{gm}^{-2}$. These numbers agree better with the limb IWP from ERA5 and the correlation between both datasets is better than for the IWC (about 0.4). The retrieved R_{med} ranges from $5.6\,\mu m$ to $10.5\,\mu m$, which would correspond to small-middle size ice particles in middle-latitudes according to the climatology of Krämer et al. (2020).

4. Can micro-physical models reproduce the formation of cirrus in the UTLS?

To answer this question, two case studies of cirrus with CTHs above the tropopause were selected for comparison with CLaMS-Ice. CLaMS-Ice combines the trajectory module of CLaMS (Chemical Lagrangian Model of the Stratosphere) with a double moment bulk microphysics scheme. First, backward trajectories starting in the area of study were computed, followed by simulating the microphysics along the trajectories in the forward direction.

To simulate different scenarios, three ice nuclei particle (INP) concentrations were predefined: $10\,\mathrm{m}^{-3}$ (clean environment), $5 \times 10^{3}\,\mathrm{m}^{-3}$ and $2 \times 10^{4}\,\mathrm{m}^{-3}$ (highly polluted environment). Whereas the two higher INP values are found in the literature, the lowest value is not based on observations and was an experiment, since in the lowermost stratosphere there is a deficit of measurements of INP. To define the region of study two approaches were used. The first one consists on defining a latitude-longitude-altitude box that includes the region where the cloud was observed. The second one, consists on determining points along the corresponding LOS. For all scenarios, clouds were formed in situ (T < 235 K) in the region of study. RH_{ice} was high enough for the homogeneous ice nucleation to occur. As the freezing RH_{ice} of homogeneous ice nucleation is higher

than for heterogeneous, heterogeneous IWC is more frequent. However, once triggered, the homogeneous IWC often reaches higher values, especially at the beginning of the homogeneous ice nucleation. For both case studies the more probable scenarios are INP concentrations of $5 \times 10^3 \, \mathrm{m}^{-3}$ and $2 \times 10^4 \, \mathrm{m}^{-3}$ and not the INP concentration for a very clean environment.

The LOS approach is more restrictive, since it gives a very specific location. Therefore, only a few trajectories formed a cloud at or close to points along the LOS. The box approach is more flexible and more suitable to test if the model can form clouds in a determined region. Even though the comparison between the model and the observations is not exact, due to the uncertainty in the cloud location, it is a success that CLaMS-Ice is able to form very thin clouds close to the tropopause and to give information about the nucleation processes. This proves, that input data with higher resolution (ERA5 in this study) and improved parametrizations of the temperature fluctuations lead to better performance of the micro-physical models.

List of Figures

List of Tables

List of abbreviations

AI aerosol index

BT brightness temperature

CBH cloud bottom height

CTH cloud top height

ECMWF European Center for Medium-Range Weather Forecasts

Ex-UTLS extratropical upper troposphere–lowermost stratosphere

CALIOP Cloud-Aerosol Lidar with Orthogonal Polarization

CALIPSO Cloud-Aerosol Lidar and Infrared Pathfinder Satellite Observations

CI cloud index

CLaMS Chemical Lagrangian Model of the Stratosphere

CRISTA Cryogenic Infrared Spectrometers and Telescopes

CRISTA-NF Cryogenic Infrared Spectrometers and Telescopes-New Frontiers

GLORIA Gimballed Limb Observer for Radiance Imager of the Atmosphere

INP ice nuclei particle

IR infrared

ITCZ intertropical convergent zone

IWC ice water content

IWP ice water path

JURASSIC2 JUelich Rapid Spectral Simulation Code V2

JUTIL JUelich Tomographic Inversion Library

LOS line of sight

MIPAS Michelson Interferometer for Passive Atmospheric Sounding

PDF probability density function

PV potential vorticity

SVC subvisible cirrus

TIL tropopause inversion layer

UTLS upper troposphere–lowermost stratosphere

UV ultraviolet

WCB warm conveyor belt

WISE Wave-driven ISentropic Exchange

WMO World Meteorological Organization

List of symbols

β_{a}	absorption coefficient
β_{e}	extinction coefficient
β_{s}	scattering coefficient
Δz	thickness of the tangent layer
ϵ	error
Γ	lapse rate
λ	wavelenght
μ	median
$\hat{\Omega}'$	direction from which the scattered radiation can contribute
$\hat{\Omega}$	direction of interest
ν	wavenumber
σ	standar deviation
θ	potential temperature
$B(T)$	Planck's function
c	speed of light
CI_{thres}	cloud index threshold
c_p	specific heat of dry air
$\boldsymbol{F}$	forward model
h	Planck's constant
I	radiance
k	Boltzmann's constant

k_{thres}	extinction coefficient threshold
N^2	static stability
p	pressure
p_0	standard pressure
$p(\hat{\Omega}', \hat{\Omega})$	phase function
T	temperature
TH	tangent altitude
TP_{med}	median tropopause
TP_{95}	95th percentile of the tropopause
R	gas constant for dry air
R_E	Earth's radius: 6 371 km
r_{eff}	effective radius
R_{med}	median radius
RH_{ice}	Relative humidity with respect to ice
s	length of the ray path through the tangent layer
x	size parameter (or state vector in eq. 3.1)
$\boldsymbol{y}$	measurement vector
z	altitude

Bibliography

A. J. Baran, P. N. Francis, and P. Yang. A process study of the dependence of ice crystal absorption on particle geometry: Application to aircraft radiometric measurements of cirrus cloud in the terrestrial window region. *J. Atmos. Sci.*, 60(2):417–427, 2003.

M. Baumgartner, C. Rolf, J.-U. Grooß, J. Schneider, T. Schorr, O. Möhler, P. Spichtinger, and M. Krämer. New investigations on homogeneous ice nucleation: the effects of water activity and water saturation formulations. *Atmos. Chem. Phys. Discuss.*, 2021:1– 40, 2021. doi: $10.5194/\text{acp-2021-320}$. URL `https://acp.copernicus.org/preprints/acp-2021-320/`.

R. Biondi, W. J. Randel, S.-P. Ho, T. Neubert, and S. Syndergaard. Thermal structure of intense convective clouds derived from GPS radio occultations. *Atmos. Chem. Phys.*, 12(12):5309–5318, 2012. doi: $10.5194/\text{acp-12-5309-2012}$.

J. Blank. *Tomographic retrieval of atmospheric trace gases observed by GLORIA*. Ph.D thesis, Bergische Universität Wuppertal, Germany, 2013. URL `https://juser.fz-juelich.de/record/150342,lastaccess:25March2021`.

F. Boudala, G. Isaac, Q. Fu, and S. Cober. Parameterization of effective ice particle size for high-latitude clouds. *International Journal of Climatology*, 22:1267 − 1284, 08 2002. doi: $10.1002/\text{joc.774}$.

A. Costa. *Mixed-phase and ice cloud observations with NIXE-CAPS*. Ph.D thesis, Bergische Universität Wuppertal, Jülich, 2017. URL `https://juser.fz-juelich.de/record/829847`. Universität Wuppertal, Diss., 2017.

A. R. Curtis. Discussion of 'A statistical model for water vapour absorption' by R. M. Goody. *Quart. J. Roy. Meteorol. Soc.*, 78:638–640, 1952.

S. Davis, D. Hlavka, E. Jensen, K. Rosenlof, Q. O. Yang, S. Schmidt, S. Borrmann, W. Frey, P. Lawson, H. Voemel, and T. P. Bui. In situ and lidar observations of tropopause subvisible cirrus clouds during TC4. *J. Geophys. Res.*, 115(D00J17), 2010. doi: $10.1029/2009JD013093$.

J. M. E. Delanoë, A. J. Heymsfield, A. Protat, A. Bansemer, and R. J. Hogan. Normalized particle size distribution for remote sensing application. *J. Geophys. Res. Atmos.*, 119 (7):4204–4227, 2014. doi: $https://doi.org/10.1002/2013JD020700$.

P. J. DeMott, D. J. Cziczo, A. J. Prenni, D. M. Murphy, S. M. Kreidenweis, D. S. Thomson, R. Borys, and D. C. Rogers. Measurements of the concentration and composition of nuclei for cirrus formation. *Proceedings of the National Academy of Sciences*, 100(25): 14655–14660, 2003. ISSN 0027-8424. doi: $10.1073/pnas.2532677100$. URL `https://www.pnas.org/content/100/25/14655`.

A. E. Dessler. Clouds and water vapor in the Northern Hemisphere summertime stratosphere. *J. Geophys. Res.*, 114(D4):D00H09, 2009. ISSN 2156-2202. doi: $10.1029/2009JD012075$.

T. Dinh, A. Podglajen, A. Hertzog, B. Legras, and R. Plougonven. Effect of gravity wave temperature fluctuations on homogeneous ice nucleation in the tropical tropopause layer. *Atmos. Chem. Phys. Discuss.*, 15, 03 2015. doi: $10.5194/acpd-15-8771-2015$.

D. P. Donovan. Ice-cloud effective particle size parameterization based on combined lidar, radar reflectivity, and mean Doppler velocity measurements. *J. Geophys. Res. Atmos.*, 108(D18), 2003. doi: $10.1029/2003JD003469$.

A. Dudhia. The Reference Forward Model (RFM). *J. Quant. Spectrosc. Radiat. Transfer*, 186:243–253, 2017. ISSN 0022-4073. doi: $http://dx.doi.org/10.1016/j.jqsrt.2016.06.018$.

H. Ertel. Ein neuer hydrodynamischer Wirbelsatz. *Meteorol. Z.*, 59 (9):277–281, 1942.

European Space Agency. https://earth.esa.int/web/guest/missions/esa-operational-eo-missions/envisat/instruments/sciamachy-handbook/wiki/-/wiki/SCIAMACHY%20Handbook/The+Atmospheric+Layers, last accessed: 15 April 2021.

F. Friedl-Vallon, T. Gulde, F. Hase, A. Kleinert, T. Kulessa, G. Maucher, T. Neubert, F. Olschewski, C. Piesch, P. Preusse, H. Rongen, C. Sartorius, H. Schneider, A. Schoenfeld, V. Tan, N. Bayer, J. Blank, R. Dapp, A. Ebersoldt, H. Fischer, F. Graf, T. Guggenmoser, M. Hoepfner, M. Kaufmann, E. Kretschmer, T. Latzko, H. Nordmeyer, H. Oelhaf, J. Orphal, M. Riese, G. Schardt, J. Schillings, M. K. Sha, O. Suminska-Ebersoldt, and J. Ungermann. Instrument concept of the imaging Fourier transform spectrometer GLORIA. *Atmos. Meas. Tech.*, 7(10):3565–3577, 2014. doi: $10.5194/\mathrm{amt}\text{-}7\text{-}3565\text{-}2014$.

A. Gettelman, P. Hoor, L. L. Pan, W. J. Randel, M. I. Hegglin, and T. Birner. The extratropical upper troposphere and lower stratosphere. *Rev. Geophys.*, 49(3), 2011. doi: $\mathrm{https://doi.org/10.1029/2011RG000355}$. URL `https://agupubs.onlinelibrary.wiley.com/doi/abs/10.1029/2011RG000355`.

J. Gibbs. Fourier series. *Nature*, (59):200 and 606, 1899. doi: $10.1038/059606a0$.

Global Volcanism Program, 2013. Volcanoes of the world, v.4.9.1 (17 sep 2020), Venzke, E(ed). Smithsonian Institution. `https://volcano.si.edu/faq/index.cfm?question=eruptionsbyyear&checkyear=2017`. Downloaded 23 Nov 2020.

W. L. Godson. The evaluation of infra-red radiative fluxes due to atmospheric water vapour. *Quart. J. Roy. Meteorol. Soc.*, 79:367–379, 1953.

L. Goldfarb, P. Keckhut, M.-L. Chanin, and A. Hauchecorne. Cirrus climatological results from lidar measurements at OHP (44 °N, 6 °E). *Geophys. Res. Lett.*, 28(9):1687–1690, 2001. doi: $10.1029/2000GL012701$.

L. L. Gordley and J. M. Russell. Rapid inversion of limb radiance data using an emissivity growth approximation. *Appl. Optics*, 20:807–813, 1981.

S. Griessbach, L. Hoffmann, M. Hoepfner, M. Riese, and R. Spang. Scattering in infrared radiative transfer: A comparison between the spectrally averaging model JURASSIC and the line-by-line model KOPRA. *J. Quant. Spectrosc. Radiat. Transfer*, 27:102–118, 2013. doi: 10.1016/j.jqsrt.2013.05.004.

S. Griessbach, L. Hoffmann, R. Spang, and M. Riese. Volcanic ash detection with infrared limb sounding: MIPAS observations and radiative transfer simulations. *Atmos. Meas. Tech.*, 7(5):1487–1507, 2014. doi: 10.5194/amt-7-1487-214.

S. Griessbach, L. Hoffmann, R. Spang, M. von Hobe, R. Müller, and M. Riese. Infrared limb emission measurements of aerosol in the troposphere and stratosphere. *Atmos. Meas. Tech.*, 9(9):4399–4423, 2016. doi: 10.5194/amt-9-4399-2016.

S. Griessbach, L. Hoffmann, R. Spang, P. Achtert, M. von Hobe, N. Mateshvili, R. Müller, M. Riese, C. Rolf, P. Seifert, and J.-P. Vernier. Aerosol and cloud top height information of Envisat MIPAS measurements. *Atmos. Meas. Tech.*, 13(3):1243–1271, 2020. doi: 10.5194/amt-13-1243-2020.

K. Grise, D. Thompson, and T. Birner. A Global Survey of Static Stability in the Stratosphere and Upper Troposphere. *J. Clim.*, 23:2275–2292, 05 2010. doi: 10.1175/2009JCLI3369.1.

T. Guggenmoser. *Data Processing and Trace Gas Retrievals for the GLORIA Limb Sounder*. Ph.d thesis, Bergische Universität Wuppertal, 2014. URL https://juser.fz-juelich.de/record/185613.

J. E. Hansen and L. D. Travis. Light scattering in planetary atmospheres. *Space Science Review*, 16, 1974.

H. Hersbach, B. Bell, P. Berrisford, S. Hirahara, A. Horányi, J. Muñoz-Sabater, J. Nicolas, C. Peubey, R. Radu, D. Schepers, A. Simmons, C. Soci, S. Abdalla, X. Abellan, G. Balsamo, P. Bechtold, G. Biavati, J. Bidlot, M. Bonavita, G. De Chiara, P. Dahlgren, D. Dee, M. Diamantakis, R. Dragani, J. Flemming, R. Forbes, M. Fuentes, A. Geer, L. Haimberger, S. Healy, R. J. Hogan, E. Hólm, M. Janisková, S. Keeley, P. Laloyaux,

P. Lopez, C. Lupu, G. Radnoti, P. de Rosnay, I. Rozum, F. Vamborg, S. Villaume, and J.-N. Thépaut. The ERA5 global reanalysis. *Quart. J. Roy. Meteorol. Soc.*, 146(730): 1999–2049, 2020. doi: $10.1002/\mathrm{qj}.3803$.

L. Hoffmann, M. Kaufmann, R. Spang, R. Müller, J. Remedios, D. P. Moore, C. M. Volk, T. von Clarmann, and M. Riese. Envisat MIPAS measurements of CFC-11: retrieval, validation, and climatology. *Atmos. Chem. Phys.*, 8:3671–3688, 2008.

J. R. Holton, P. H. Haynes, M. E. McIntyre, A. R. Douglass, R. B. Rood, and L. Pfister. Stratosphere-troposphere exchange. *Rev. Geophys.*, 33(4):403–439, 1995. doi: $\mathrm{https://doi.org/10.1029/95RG02097}$. URL `https://agupubs.onlinelibrary.wiley.com/doi/abs/10.1029/95RG02097`.

M. Höpfner and C. Emde. Comparison of single and multiple scattering approaches for the simulation of limb-emission observations in the mid-IR. *J. Quant. Spectrosc. Radiat. Transfer*, 91:275–285, 2005.

M. Höpfner, J. Ungermann, S. Borrmann, R. Wagner, R. Spang, M. Riese, G. Stiller, O. Appel, A. M. Batenburg, S. Bucci, F. Cairo, A. Dragoneas, F. Friedl-Vallon, A. Hünig, S. Johansson, L. Krasauskas, B. Legras, T. Leisner, C. Mahnke, O. Möhler, S. Molleker, R. Müller, T. Neubert, J. Orphal, P. Preusse, M. Rex, H. Saathoff, F. Stroh, R. Weigel, and I. Wohltmann. Ammonium nitrate particles formed in upper troposphere from ground ammonia sources during Asian monsoons. *Nature Geosciences*, 12(8):608–612, 2019. ISSN 1752-0908. doi: $10.1038/\mathrm{s}41561\text{-}019\text{-}0385\text{-}8$.

R. Hossaini, M. Chipperfield, S. Montzka, A. Rap, S. Dhomse, and W. Feng. Efficiency of short-lived halogens at influencing climate through depletion of stratospheric ozone. *Nature Geoscience*, 8(3):186–190, March 2015. © 2015 Macmillan Publishers Limited. This is an author produced version of a paper published in Nature Geoscience. Uploaded in accordance with the publisher's self-archiving policy.

L. Howard. *ESSAY, ETC*, page 1–37. Cambridge Library Collection - Earth Science. Cambridge University Press, 2011. doi: $10.1017/\mathrm{CBO}9781139096966.004$.

IPCC. *Climate Change 2013: The Physical Science Basis. Contribution of Working Group I to the Fifth Assessment Report of the Intergovernmental Panel on Climate Change [Stocker, T.F., D. Qin, G.-K. Plattner, M. Tignor, S.K. Allen, J. Boschung, A. Nauels, Y. Xia, V. Bex and P.M. Midgley (eds.)]*. Cambridge University Press, Cambridge, United Kingdom and New York, NY, USA, 2013. ISBN ISBN 978-1-107-66182-0. doi: $10.1017/CBO9781107415324$.

C. Kalicinsky, S. Griessbach, and R. Spang. A new method to detect and classify polar stratospheric nictric acid tryhydrate clouds derived from a radiative transfer simulations and its first application to airborne infrared limb emission. *Atmos. Meas. Tech.*, 14(3): 1893–1915, 2021. doi: $10.5194/amt$-14-1893-2021. URL https://amt.copernicus.org/articles/14/1893/2021/.

P. Keckhut, A. Hauchecorne, S. Bekki, A. Colette, C. David, and J. Jumelet. Indications of thin cirrus clouds in the stratosphere at mid-latitudes. *Atmos. Chem. Phys.*, 5:3407–3414, 2005.

G. S. Kent, D. M. Winker, M. A. Vaughan, P. H. Wang, and K. M. Skeens. Simulation of Stratospheric Aerosol and Gas Experiment (SAGE) II cloud measurements using airborne lidar data. *J. Geophys. Res.*, 102(D18):21795–21807, SEP 27 1997. doi: $\{10.1029/97JD01390\}$.

A. Kleinert, F. Friedl-Vallon, T. Guggenmoser, M. Höpfner, T. Neubert, R. Ribalda, M. Sha, J. Ungermann, J. Blank, A. Ebersoldt, E. Kretschmer, T. Latzko, H. Oelhaf, F. Olschewski, and P. Preusse. Level 0 to 1 processing of the imaging Fourier transform spectrometer GLORIA: generation of radiometrically and spectrally calibrated spectra. *Atmos. Meas. Tech.*, 7:4167–4184, 12 2014. doi: $10.5194/amt$-7-4167-2014.

P. Konopka, H.-M. Steinhorst, J.-U. Grooß, G. Günther, R. Müller, J. W. Elkins, H.-J. Jost, E. Richard, U. Schmidt, G. Toon, and D. S. McKenna. Mixing and ozone loss in the 1999-2000 Arctic vortex: Simulations with the three-dimensional Chemical Lagrangian Model of the Stratosphere (CLaMS). *J. Geophys. Res. Atmos.*, 109(D2), 2004. doi: $10.1029/2003JD003792$.

M. Krämer, C. Schiller, A. Afchine, R. Bauer, I. Gensch, A. Mangold, S. Schlicht, N. Spelten, N. Sitnikov, S. Borrmann, M. de Reus, and P. Spichtinger. Ice supersaturations and cirrus cloud crystal numbers. *Atmos. Chem. Phys.*, 9(11):3505–3522, 2009. doi: $10.5194/\text{acp-9-3505-2009}$. URL `https://acp.copernicus.org/articles/9/3505/2009/`.

M. Krämer, C. Rolf, N. Spelten, A. Afchine, D. Fahey, E. Jensen, S. Khaykin, T. Kuhn, P. Lawson, A. Lykov, L. L. Pan, M. Riese, A. Rollins, F. Stroh, T. Thornberry, V. Wolf, S. Woods, P. Spichtinger, J. Quaas, and O. Sourdeval. A microphysics guide to cirrus – Part 2: Climatologies of clouds and humidity from observations. *Atmos. Chem. Phys.*, 20(21):12569–12608, 2020. doi: $10.5194/\text{acp-20-12569-2020}$.

M. Krämer, C. Rolf, A. Luebke, A. Afchine, N. Spelten, A. Costa, J. Meyer, M. Zoeger, J. Smith, R. L. Herman, B. Buchholz, V. Ebert, D. Baumgardner, S. Borrmann, M. Klingebiel, and L. Avallone. A microphysics guide to cirrus clouds - Part 1: Cirrus types. *Atmos. Chem. Phys.*, 16(5):3463–3483, 2016. ISSN 1680-7316. doi: $\{10.5194/\text{acp-16-3463-2016}\}$.

B. Kärcher, A. Dörnbrack, and I. Sölch. Supersaturation Variability and Cirrus Ice Crystal Size Distributions. *J. Atmos. Sci.*, 71(8):2905 – 2926, 2014. doi: $10.1175/\text{JAS-D-13-0404.1}$. URL `https://journals.ametsoc.org/view/journals/atsc/71/8/jas-d-13-0404.1.xml`.

I. Krisch, J. Ungermann, P. Preusse, E. Kretschmer, and M. Riese. Limited angle tomography of mesoscale gravity waves by the infrared limb-sounder GLORIA. *Atmos. Meas. Tech.*, 11(7):4327–4344, 2018. doi: $10.5194/\text{amt-11-4327-2018}$.

A. Kunz, P. Konopka, R. Müller, L. Pan, C. Schiller, and F. Rohrer. High static stability in the mixing layer above the extratropical tropopause. *J. Geophys. Res.*, 114:D16305, 08 2009. doi: $10.1029/\text{2009JD011840}$.

A. Kunz, P. Konopka, R. Müller, and L. L. Pan. Dynamical tropopause based on isentropic potential vorticity gradients. *J. Geophys. Res.*, 116(D1):D01110, 2011. ISSN 2156-2202. doi: $10.1029/\text{2010JD014343}$.

R. P. Lawson, B. Baker, B. Pilson, and Q. X. Mo. In situ observations of the microphysical properties of wave, cirrus, and anvil clouds. Part II: Cirrus clouds. *J. Atmos. Sci.*, 63 (12):3186–3203, 2006.

K.-N. Liou. Influence of Cirrus Clouds on Weather and Climate Processes: A Global Perspective. *Monthly Weather Review*, 114(6):1167–1199, 06 1986. ISSN 0027-0644. doi: $10.1175/1520\text{-}0493(1986)114{<}1167{:}IOCCOW{>}2.0.CO;2$.

A. E. Luebke, A. Afchine, A. Costa, J.-U. Grooß, J. Meyer, C. Rolf, N. Spelten, L. M. Avallone, D. Baumgardner, and M. Krämer. The origin of midlatitude ice clouds and the resulting influence on their microphysical properties. *Atmos. Chem. Phys.*, 16(9): 5793–5809, 2016. doi: $10.5194/acp\text{-}16\text{-}5793\text{-}2016$.

G. G. Mace, Q. Zhang, M. Vaughan, R. Marchand, G. Stephens, C. Trepte, and D. Winker. A description of hydrometeor layer occurrence statistics derived from the first year of merged cloudsat and calipso data. *J. Geophys. Res. Atmos.*, 114(D8), 2009. doi: `https://doi.org/10.1029/2007JD009755`. URL `https://agupubs.onlinelibrary.wiley.com/doi/abs/10.1029/2007JD009755`.

C. Magono and C. Lee. Meteorological classificaiton of natural snow crystals. *J. Fac. Sci. Hokkaido Univ.*, Ser. VII(2):321–335, 1966.

E. Martins, V. Noel, and H. Chepfer. Properties of cirrus and subvisible cirrus from nighttime Cloud-Aerosol Lidar with Orthogonal Polarization (CALIOP), related to atmospheric dynamics and water vapor. *J. Geophys. Res. Atmos.*, 116(D02208), 2011. doi: `https://doi.org/10.1029/2010JD014519`.

D. S. McKenna, J.-U. Grooß, G. Günther, P. Konopka, R. Müller, G. Carver, and Y. Sasano. A new Chemical Lagrangian Model of the Stratosphere (CLaMS): 2. Formulation of chemistry scheme and initialization. *J. Geophys. Res.*, 107(D15):4256, 2002a. doi: $10.1029/2000JD000113$.

D. S. McKenna, P. Konopka, J.-U. Grooß, G. Günther, R. Müller, R. Spang, D. Offermann, and Y. Orsolini. A new Chemical Lagrangian Model of the Stratosphere (CLaMS): 1.

Formulation of advection and mixing. *J. Geophys. Res.*, 107(D16):4309, 2002b. doi: 10.1029/2000JD000114.

Met Office, 2017. URL www1.wetter3.de/archiv_ukmet_dt.html.

V. Noël and M. Haeffelin. Midlatitude cirrus clouds and multiple tropopauses from a 2002–2006 climatology over the SIRTA observatory. *J. Geophys. Res.*, 112(D13): D13206, 2007. ISSN 2156-2202. doi: 10.1029/2006JD007753.

L. L. Pan and L. A. Munchak. Relationship of cloud top to the tropopause and jet structure from CALIPSO data. *J. Geophys. Res.*, 116(D12):D12201, 2011. ISSN 2156-2202. doi: 10.1029/2010JD015462.

T. R. Peevey, J. C. Gille, C. E. Randall, and A. Kunz. Investigation of double tropopause spatial and temporal global variability utilizing high resolution dynamics limb sounder temperature observations. *J. Geophys. Res. Atmos.*, 117(D1), 2012. doi: https://doi.org/10.1029/2011JD016443.

T. R. Peevey, J. C. Gille, C. R. Homeyer, and G. L. Manney. The double tropopause and its dynamical relationship to the tropopause inversion layer in storm track regions. *J. Geophys. Res. Atmos.*, 119(17):10,194–10,212, 2014. doi: https://doi.org/10.1002/2014JD021808.

G. W. Petty. *A first Course in Atmospheric Radiation*. Sundog Publishing, 2006.

A. Podglajen, A. Hertzog, R. Plougonven, and B. Legras. Lagrangian temperature and vertical velocity fluctuations due to gravity waves in the lower stratosphere. *Geophys. Res. Lett.*, 43(7):3543–3553, 2016. doi: https://doi.org/10.1002/2016GL068148.

W. J. Randel, D. J. Seidel, and L. L. Pan. Observational characteristics of double tropopauses. *J. Geophys. Res.*, 112:D07309, 2007. doi: 10.1029/2006JD007904.

J. J. Remedios, R. J. Leigh, A. M. Waterfall, D. P. Moore, H. Sembhi, I. Parkes, J. Green-hough, M. Chipperfield, and D. Hauglustaine. MIPAS reference atmospheres and com-

parisons to V4.61/V4.62 MIPAS level 2 geophysical data sets. *Atmos. Chem. Phys. Discuss.*, 7:9973–10017, 2007. doi: $10.5194/\mathrm{acpd}\text{-}7\text{-}9973\text{-}2007$.

M. Reverdy, V. Noel, H. Chepfer, and B. Legras. On the origin of subvisible cirrus clouds in the tropical upper troposphere. *Atmos. Chem. Phys.*, 12(24):12081–12101, 2012. doi: $10.5194/\mathrm{acp}\text{-}12\text{-}12081\text{-}2012$.

M. Riese, Kaufmann, and P. M., Hoor. *WISE: project description*, 2017, last accessed: 13 August 2020. URL `https://www.halo.dlr.de/science/missions/wise/wise.html`.

M. Riese, F. Ploeger, A. Rap, B. Vogel, P. Konopka, M. Dameris, and P. Forster. Impact of uncertainties in atmospheric mixing on simulated UTLS composition and related radiative effects. *J. Geophys. Res.*, 117:D16305, AUG 23 2012. ISSN 2169-897X. doi: $\{10.1029/2012\mathrm{JD}017751\}$.

M. Riese, H. Oelhaf, P. Preusse, J. Blank, M. Ern, F. Friedl-Vallon, H. Fischer, T. Guggenmoser, M. Hoepfner, P. Hoor, M. Kaufmann, J. Orphal, F. Ploeger, R. Spang, O. Suminska-Ebersoldt, J. Ungermann, B. Vogel, and W. Woiwode. Gimballed Limb Observer for Radiance Imaging of the Atmosphere (GLORIA) scientific objectives. *Atmos. Meas. Tech.*, 7(7):1915–1928, 2014. doi: $10.5194/\mathrm{amt}\text{-}7\text{-}1915\text{-}2014$.

C. Rolf. *Lidar observations of natural and volcanic-ash-induced cirrus clouds*. Ph.D thesis, Universität Wuppertal, Jülich, 2013. URL `https://juser.fz-juelich.de/record/151817`. Dissertation, Universität Wuppertal, 2012.

K. Sassen and B. S. Cho. Subvisual-thin cirrus lidar data set for satellite verification and climatological research. *J. Appl. Met.*, 31:1275–1285, 1992. doi: $\mathrm{https://doi.org/10.1175/1520\text{-}0450(1992)031{<}1275{:}STCLDF{>}2.0.CO;2}$.

K. Sassen, Z. Wang, and D. Liu. Global distribution of cirrus clouds from CloudSat/Cloud-Aerosol Lidar and Infrared Pathfinder Satellite Observations (CALIPSO) measurements. *J. Geophys. Res.*, 113(D20):D00A12, OCT 31 2008. ISSN 2169-897X. doi: $\{10.1029/2008\mathrm{JD}009972\}$.

W. Schubert, E. Ruprecht, R. Hertenstein, R. Nieto Ferreira, R. Taft, C. Rozoff, P. Ciesielski, and H.-C. Kuo. English translations of twenty-one of ertel's papers on geophysical fluid dynamics. *Meteorologische Zeitschrift - METEOROL Z*, 13, 12 2004. doi: $10.1127/0941\text{-}2948/2004/0013\text{-}0527$.

H. Sembhi, J. Remedios, T. Trent, D. P. Moore, R. Spang, S. Massie, and J. P. Vernier. MIPAS detection of cloud and aerosol particle occurrence in the utls with comparison to HIRDLS and CALIOP. *Atmos. Meas. Tech.*, 5(10):2537–2553, 2012. doi: $10.5194/amt\text{-}5\text{-}2537\text{-}2012$.

M. K. Sha. Characterization and Optimization of the new Imaging Fourier Transform Spectrometer GLORIA. 2013. doi: $10.5445/IR/1000038372$. URL `https://publikationen.bibliothek.kit.edu/1000038372`.

R. Spang, M. Riese, and D. Offermann. CRISTA-2 observations of the south polar vortex in winter 1997: A new dataset for polar process studies. *Geophys. Res. Lett.*, 28(16): 3159–3162, 2001. doi: $10.1029/2000GL012374$.

R. Spang, L. Hoffmann, A. Kullmann, F. Olschewski, P. Preusse, P. Knieling, S. Schroeder, F. Stroh, K. Weigel, and M. Riese. High resolution limb observations of clouds by the CRISTA-NF experiment during the SCOUT-O3 tropical aircraft campaign. *Adv. Space Res.*, 42(10):1765–1775, 2008. doi: $10.1016/j.asr.2007.09.036$.

R. Spang, K. Arndt, A. Dudhia, M. Höpfner, L. Hoffmann, J. Hurley, R. G. Grainger, S. Griessbach, C. Poulsen, J. J. Remedios, M. Riese, H. Sembhi, R. Siddans, A. Waterfall, and C. Zehner. Fast cloud parameter retrievals of MIPAS/Envisat. *Atmos. Chem. Phys.*, 12(15):7135–7164, 2012. doi: $10.5194/acp\text{-}12\text{-}7135\text{-}2012$.

R. Spang, G. Günther, M. Riese, L. Hoffmann, R. Müller, and S. Griessbach. Satellite observations of cirrus clouds in the northern hemisphere lowermost stratosphere. *Atmos. Chem. Phys.*, 15(2):927–950, 2015. doi: $10.5194/acp\text{-}15\text{-}927\text{-}2015$.

R. Spang, L. Hoffmann, M. Höpfner, S. Griessbach, R. Müller, M. C. Pitts, A. M. W. Orr, and M. Riese. A multi-wavelength classification method for polar stratospheric cloud

types using infrared limb spectra. *Atmos. Meas. Tech.*, 9(8):3619–3639, 2016. doi: $10.5194/\mathrm{amt}\text{-}9\text{-}3619\text{-}2016$.

P. Spichtinger and K. M. Gierens. Modelling of cirrus clouds – Part 1a: Model description and validation. *Atmos. Chem. Phys.*, 9(2):685–706, 2009. doi: $10.5194/\mathrm{acp}\text{-}9\text{-}685\text{-}2009$.

L. Tian, G. M. Heymsfield, L. Li, A. J. Heymsfield, A. Bansemer, C. H. Twohy, and R. C. Srivastava. A Study of Cirrus Ice Particle Size Distribution Using TC4 Observations. *J. Atmos. Sci.*, 67(1):195 – 216, 2010. doi: $10.1175/2009\mathrm{JAS}3114.1$.

O. B. Toon, M. A. Tolbert, B. G. Koehler, A. M. Middlebrook, and J. Jordan. Infrared optical constants of H_2O, ice, amorphous nitric acid solutions, and nitric acid hydrates. *J. Geophys. Res.*, 99(D12):25631–25654, 1994.

A. F. Tuck, D. Baumgardner, K. R. Chan, J. E. Dye, J. W. Elkins, S. J. Hovde, K. K. Kelly, M. Loewenstein, J. J. Margitan, R. D. May, J. R. Podolske, M. H. Proffitt, K. H. Rosenlof, W. L. Smith, C. R. Webster, and J. C. Wilson. The Brewer-Dobson Circulation In the Light of High Altitude In Situ Aircraft Observations. *Quart. J. Roy. Meteorol. Soc.*, 123(537):1–69, 1997. doi: $\mathrm{https://doi.org/10.1002/qj.49712353702}$. URL `https://rmets.onlinelibrary.wiley.com/doi/abs/10.1002/qj.49712353702`.

J. Ungermann, M. Kaufmann, L. Hoffmann, P. Preusse, H. Oelhaf, F. Friedl-Vallon, and M. Riese. Towards a 3-D tomographic retrieval for the air-borne limb-imager GLORIA. *Atmos. Meas. Tech.*, 3(6):1647–1665, 2010. doi: $10.5194/\mathrm{amt}\text{-}3\text{-}1647\text{-}2010$.

J. Ungermann, J. Blank, J. Lotz, K. Leppkes, L. Hoffmann, T. Guggenmoser, M. Kaufmann, P. Preusse, U. Naumann, and M. Riese. A 3-D tomographic retrieval approach with advection compensation for the air-borne limb-imager GLORIA. *Atmos. Meas. Tech.*, 4:2509 – 2529, 2011. ISSN 1867-1381. doi: $10.5194/\mathrm{amt}\text{-}4\text{-}2509\text{-}2011$.

J. Ungermann, J. Blank, M. Dick, A. Ebersoldt, F. Friedl-Vallon, A. Giez, T. Guggenmoser, M. Höpfner, T. Jurkat, M. Kaufmann, S. Kaufmann, A. Kleinert, M. Krämer, T. Latzko, H. Oelhaf, F. Olchewski, P. Preusse, C. Rolf, J. Schillings, and M. Riese. Level 2 processing for the imaging Fourier transform spectrometer GLORIA: Derivation and valida-

tion of temperature and trace gas volume mixing ratios from calibrated dynamics mode spectra. *Atmos. Meas. Tech.*, 8:2473–2489, 06 2015. doi: $10.5194/amt\text{-}8\text{-}2473\text{-}2015$.

J. Ungermann, I. Bartolome, S. Grießbach, R. Spang, C. Rolf, M. Krämer, M. Höpfner, and M. Riese. Cirrus cloud shape detection by tomographic extinction retrievals from infrared limb emission sounder measurements. *Atmos. Meas. Tech.*, 13(12):7025–7045, 2020. doi: $10.5194/amt\text{-}13\text{-}7025\text{-}2020$. URL https://amt.copernicus.org/articles/13/7025/2020/.

J. Ungermann, A. Kleinert, G. Maucher, I. Bartolomé, F. Friedl-Vallon, S. Johansson, L. Krasauskas, and T. Neubert. Quantification and mitigation of the airborne limb imaging FTIR GLORIA instrument effects and uncertainties. *Atmos. Meas. Tech. Discuss.*, 2021:1–69, 2021. doi: $10.5194/amt\text{-}2021\text{-}293$. URL https://amt.copernicus.org/preprints/amt-2021-293/.

J. Wallace and P. V. Hobbs. *Atmospheric Science: an introductory survey*. Elsevier Academic Press, Amsterdam, Boston, Heidelberg, London, New York, Oxford, Paris, San Diego, San Francisco, Singapore, Sydney, Tokyo, second edition, 2006.

M. P. Weinreb and A. C. Neuendorffer. Method to apply homogeneous-path transmittance models to inhomogenous atmospheres. *J. Atmos. Sci.*, 30:662–666, 1973.

WMO. Meteorology – A three-dimensional science. *WMO Bull*, 4:134–138, 1957.

V. Wolf, T. Kuhn, and M. Krämer. On the Dependence of Cirrus Parametrizations on the Cloud Origin. *Geophys. Res. Lett.*, 46(21):12565–12571, 2019. doi: $\text{https://doi.org/}10.1029/2019GL083841$.

World Meteorological Organization. *International Cloud Atlas*, last accessed: 28 April 2021). URL https://cloudatlas.wmo.int/en/upper-atmospheric-clouds.html.

L. Zou, S. Griessbach, L. Hoffmann, B. Gong, and L. Wang. Revisiting global satellite observations of stratospheric cirrus clouds. *Atmos. Chem. Phys.*, 20(16):9939–9959, 2020. doi: $10.5194/acp\text{-}20\text{-}9939\text{-}2020$.

Appendix A

Comparison GLORIA vs ERA5

This appendix includes the cross-sections for each scientific flight of the WISE campaign comparing the inferred clouds in the ERA5-based dataset and the identified clouds with the observations. As the performance of the CI method and the extinction method is similar, only the extinction method is presented. The cross-sections represent the following classification: true-true cases (TT) if there is a cloudy occurrence for both the observations and ERA5; false-true (FT) if GLORIA detected clear air and ERA5 a cloud; true-false (TF) if GLORIA observed a cloud but ERA5 indicates clear air and FF, when both datasets indicate clear air. The tropopause corresponds to TP_{med}.
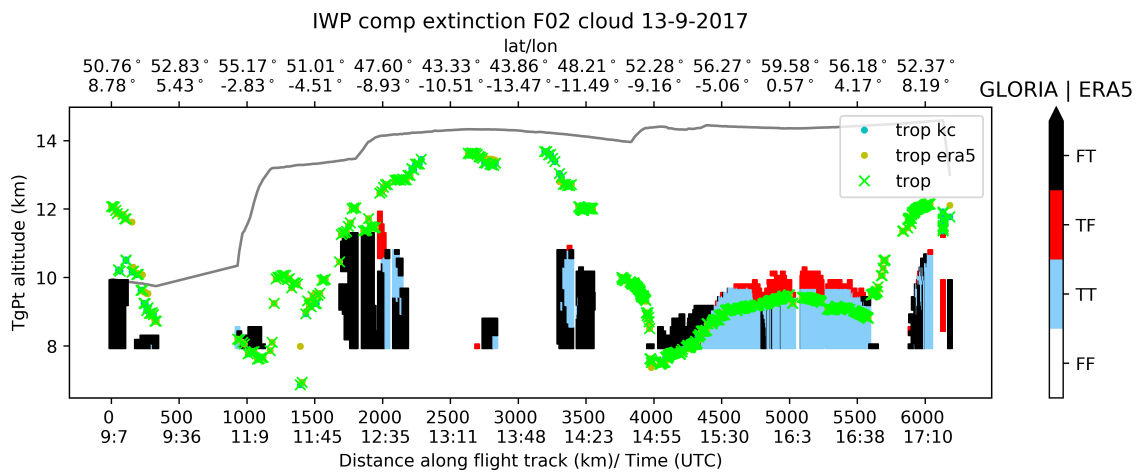
Figure A.1: Cross-sections comparing ERA5 inferred clouds and the identified with the extinction method for GLORIA for flight 2 of the WISE campaign. The results are restricted to levels below flight path (grey line). Color code represents the true-true cases (TT, in light blue) when both datasets identified a cloud; true-false (TF, in red) when a cloud was observed with GLORIA but ERA5 indicated clear air; false-true (FT, in black) when GLORIA indicated clear air and ERA5 registered a cloud and false-false (FF, in white) when both datasets indicated clear air. The blue dots indicate the median tropopause TP_{med} corresponding to the location of the observed cirrus by GLORIA. The yellow dots represent the TP_{med} corresponding to the location of the inferred cirrus with ERA5. The green crosses indicate the combined TP_{med}.The altitude of the tangent points (TgPt) is the y-axis.
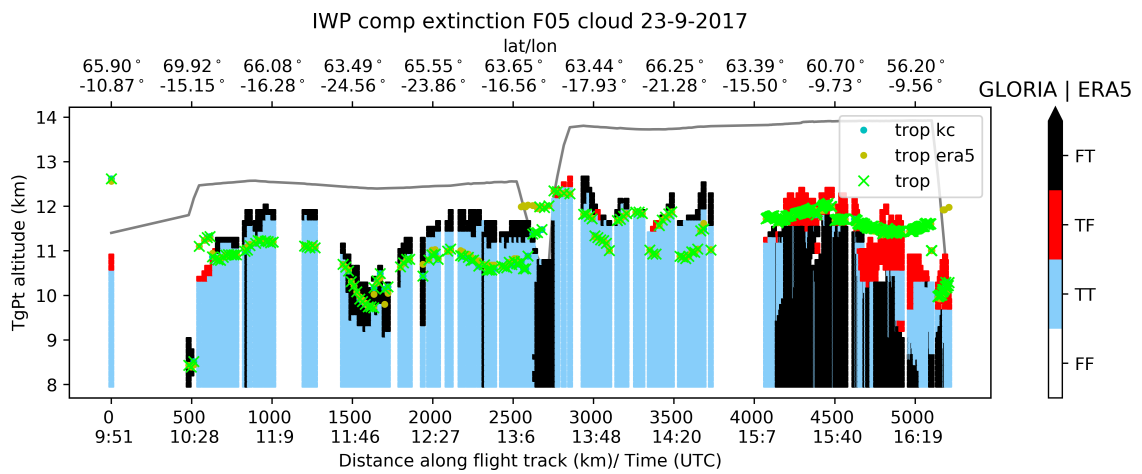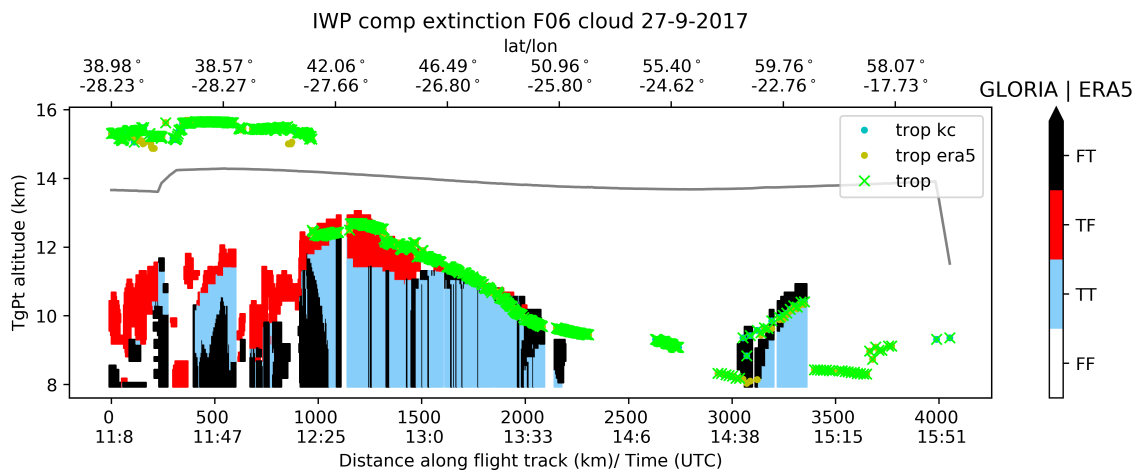
Figure A.2: Cross-sections comparing ERA5 inferred clouds and the identified with the extinction method for GLORIA for flight 3 of the WISE campaign. The results are restricted to levels below flight path (grey line). Color code represents the true-true cases (TT, in light blue) when both datasets identified a cloud; true-false (TF, in red) when a cloud was observed with GLORIA but ERA5 indicated clear air; false-true (FT, in black) when GLORIA indicated clear air and ERA5 registered a cloud and false-false (FF, in white) when both datasets indicated clear air. The blue dots indicate the median tropopause TP_{med} corresponding to the location of the observed cirrus by GLORIA. The yellow dots represent the TP_{med} corresponding to the location of the inferred cirrus with ERA5. The green crosses indicate the combined TP_{med}.The altitude of the tangent points (TgPt) is the y-axis.

Figure A.3: Cross-sections comparing ERA5 inferred clouds and the identified with the extinction method for GLORIA for flight 4 of the WISE campaign. The results are restricted to levels below flight path (grey line). Color code represents the true-true cases (TT, in light blue) when both datasets identified a cloud; true-false (TF, in red) when a cloud was observed with GLORIA but ERA5 indicated clear air; false-true (FT, in black) when GLORIA indicated clear air and ERA5 registered a cloud and false-false (FF, in white) when both datasets indicated clear air. The blue dots indicate the median tropopause TP_{med} corresponding to the location of the observed cirrus by GLORIA. The yellow dots represent the TP_{med} corresponding to the location of the inferred cirrus with ERA5. The green crosses indicate the combined TP_{med}. The altitude of the tangent points (TgPt) is the y-axis.
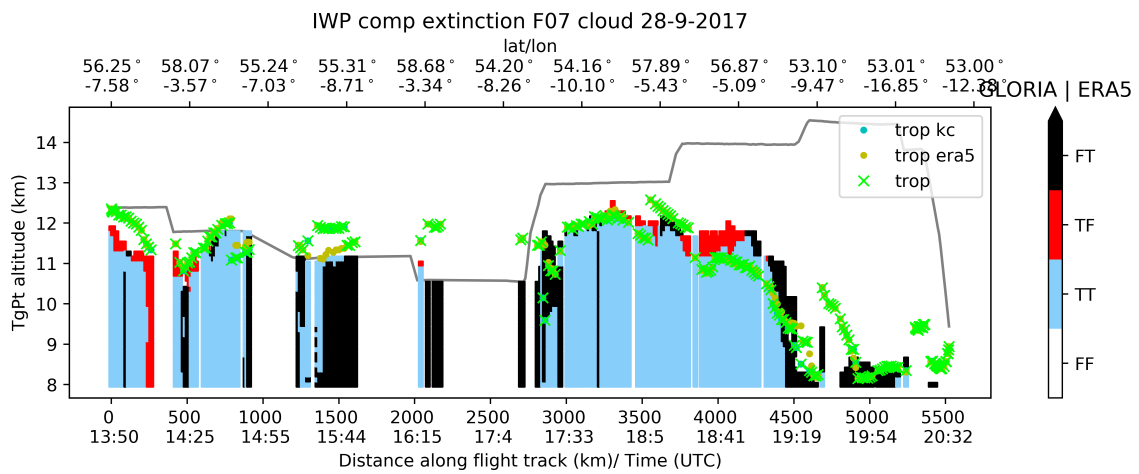
Figure A.4: Cross-sections comparing ERA5 inferred clouds and the identified with the extinction method for GLORIA for flight 5 of the WISE campaign. The results are restricted to levels below flight path (grey line). Color code represents the true-true cases (TT, in light blue) when both datasets identified a cloud; true-false (TF, in red) when a cloud was observed with GLORIA but ERA5 indicated clear air; false-true (FT, in black) when GLORIA indicated clear air and ERA5 registered a cloud and false-false (FF, in white) when both datasets indicated clear air. The blue dots indicate the median tropopause TP_{med} corresponding to the location of the observed cirrus by GLORIA. The yellow dots represent the TP_{med} corresponding to the location of the inferred cirrus with ERA5. The green crosses indicate the combined TP_{med}.The altitude of the tangent points (TgPt) is the y-axis.
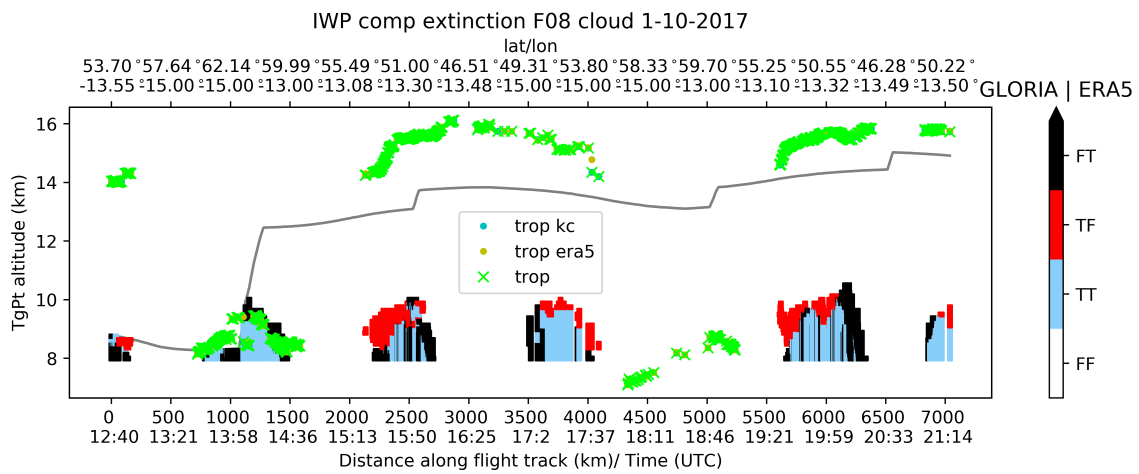
Figure A.5: Cross-sections comparing ERA5 inferred clouds and the identified with the extinction method for GLORIA for flight 6 of the WISE campaign. The results are restricted to levels below flight path (grey line). Color code represents the true-true cases (TT, in light blue) when both datasets identified a cloud; true-false (TF, in red) when a cloud was observed with GLORIA but ERA5 indicated clear air; false-true (FT, in black) when GLORIA indicated clear air and ERA5 registered a cloud and false-false (FF, in white) when both datasets indicated clear air. The blue dots indicate the median tropopause TP_{med} corresponding to the location of the observed cirrus by GLORIA. The yellow dots represent the TP_{med} corresponding to the location of the inferred cirrus with ERA5. The green crosses indicate the combined TP_{med}.The altitude of the tangent points (TgPt) is the y-axis.
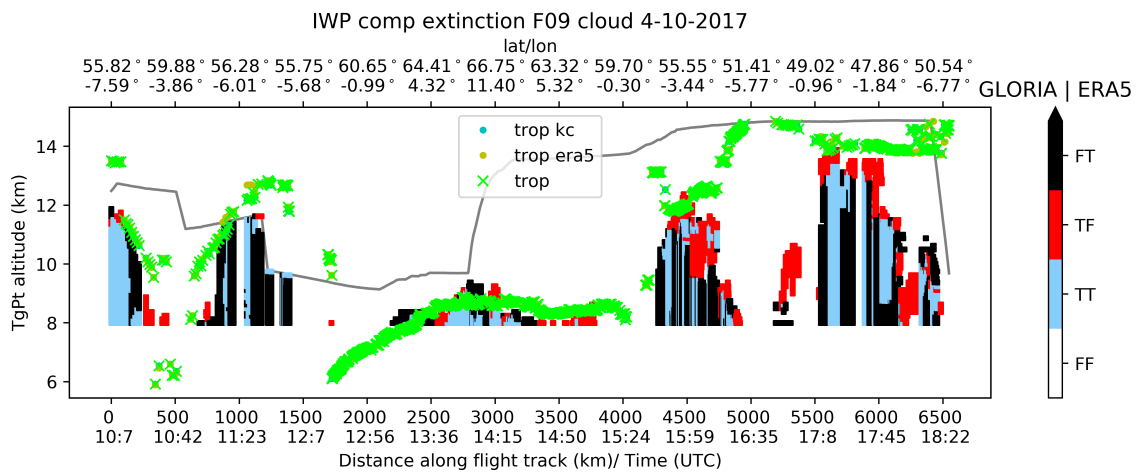
Figure A.6: Cross-sections comparing ERA5 inferred clouds and the identified with the extinction method for GLORIA for flight 7 of the WISE campaign. The results are restricted to levels below flight path (grey line). Color code represents the true-true cases (TT, in light blue) when both datasets identified a cloud; true-false (TF, in red) when a cloud was observed with GLORIA but ERA5 indicated clear air; false-true (FT, in black) when GLORIA indicated clear air and ERA5 registered a cloud and false-false (FF, in white) when both datasets indicated clear air. The blue dots indicate the median tropopause TP_{med} corresponding to the location of the observed cirrus by GLORIA. The yellow dots represent the TP_{med} corresponding to the location of the inferred cirrus with ERA5. The green crosses indicate the combined TP_{med}.The altitude of the tangent points (TgPt) is the y-axis.
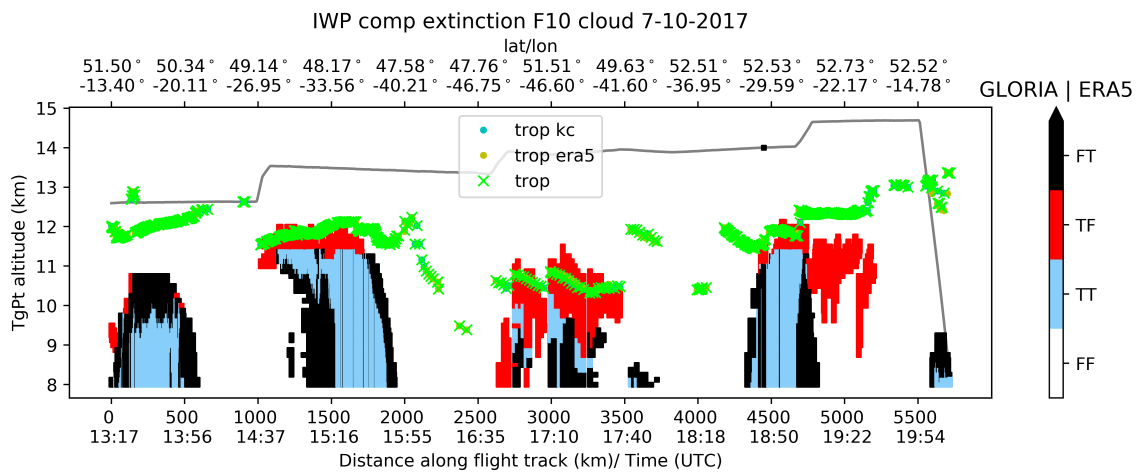
Figure A.7: Cross-sections comparing ERA5 inferred clouds and the identified with the extinction method for GLORIA for flight 8 of the WISE campaign. The results are restricted to levels below flight path (grey line). Color code represents the true-true cases (TT, in light blue) when both datasets identified a cloud; true-false (TF, in red) when a cloud was observed with GLORIA but ERA5 indicated clear air; false-true (FT, in black) when GLORIA indicated clear air and ERA5 registered a cloud and false-false (FF, in white) when both datasets indicated clear air. The blue dots indicate the median tropopause TP_{med} corresponding to the location of the observed cirrus by GLORIA. The yellow dots represent the TP_{med} corresponding to the location of the inferred cirrus with ERA5. The green crosses indicate the combined TP_{med}. The altitude of the tangent points (TgPt) is the y-axis.
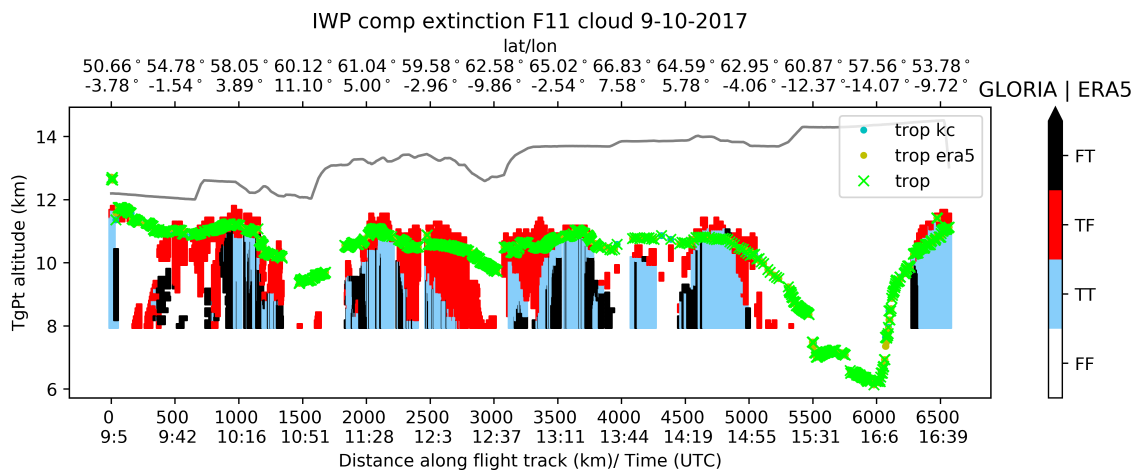
Figure A.8: Cross-sections comparing ERA5 inferred clouds and the identified with the extinction method for GLORIA for flight 9 of the WISE campaign. The results are restricted to levels below flight path (grey line). Color code represents the true-true cases (TT, in light blue) when both datasets identified a cloud; true-false (TF, in red) when a cloud was observed with GLORIA but ERA5 indicated clear air; false-true (FT, in black) when GLORIA indicated clear air and ERA5 registered a cloud and false-false (FF, in white) when both datasets indicated clear air. The blue dots indicate the median tropopause TP$_{med}$ corresponding to the location of the observed cirrus by GLORIA. The yellow dots represent the TP$_{med}$ corresponding to the location of the inferred cirrus with ERA5. The green crosses indicate the combined TP$_{med}$.The altitude of the tangent points (TgPt) is the y-axis.
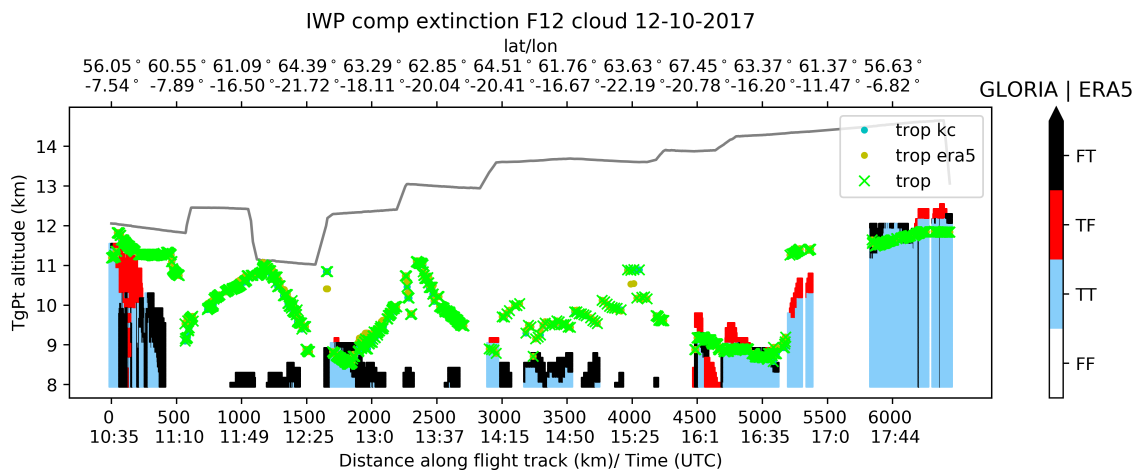
Figure A.9: Cross-sections comparing ERA5 inferred clouds and the identified with the extinction method for GLORIA for flight 10 of the WISE campaign. The results are restricted to levels below flight path (grey line). Color code represents the true-true cases (TT, in light blue) when both datasets identified a cloud; true-false (TF, in red) when a cloud was observed with GLORIA but ERA5 indicated clear air; false-true (FT, in black) when GLORIA indicated clear air and ERA5 registered a cloud and false-false (FF, in white) when both datasets indicated clear air. The blue dots indicate the median tropopause TP_{med} corresponding to the location of the observed cirrus by GLORIA. The yellow dots represent the TP_{med} corresponding to the location of the inferred cirrus with ERA5. The green crosses indicate the combined TP_{med}.The altitude of the tangent points (TgPt) is the y-axis.
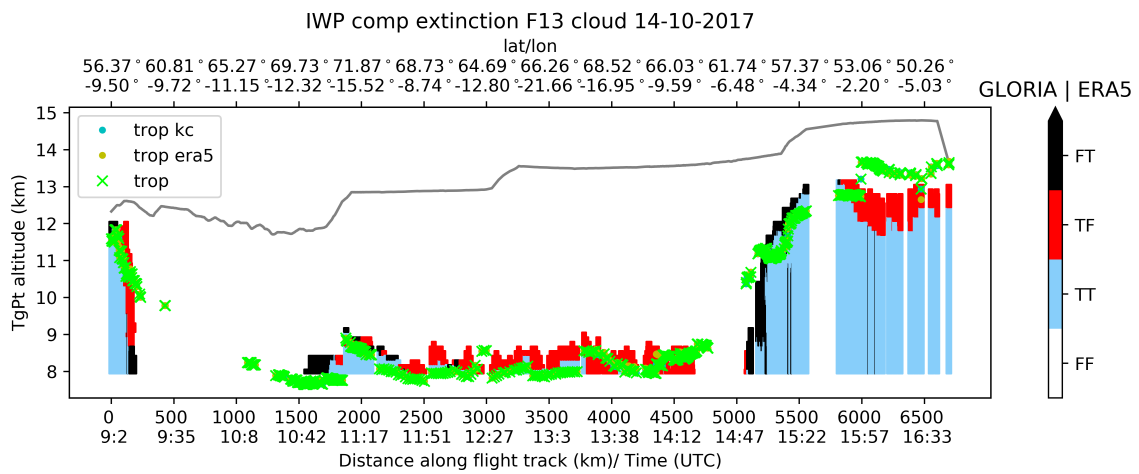
Figure A.10: Cross-sections comparing ERA5 inferred clouds and the identified with the extinction method for GLORIA for flight 11 of the WISE campaign. The results are restricted to levels below flight path (grey line). Color code represents the true-true cases (TT, in light blue) when both datasets identified a cloud; true-false (TF, in red) when a cloud was observed with GLORIA but ERA5 indicated clear air; false-true (FT, in black) when GLORIA indicated clear air and ERA5 registered a cloud and false-false (FF, in white) when both datasets indicated clear air. The blue dots indicate the median tropopause TP_{med} corresponding to the location of the observed cirrus by GLORIA. The yellow dots represent the TP_{med} corresponding to the location of the inferred cirrus with ERA5. The green crosses indicate the combined TP_{med}. The altitude of the tangent points (TgPt) is the y-axis.
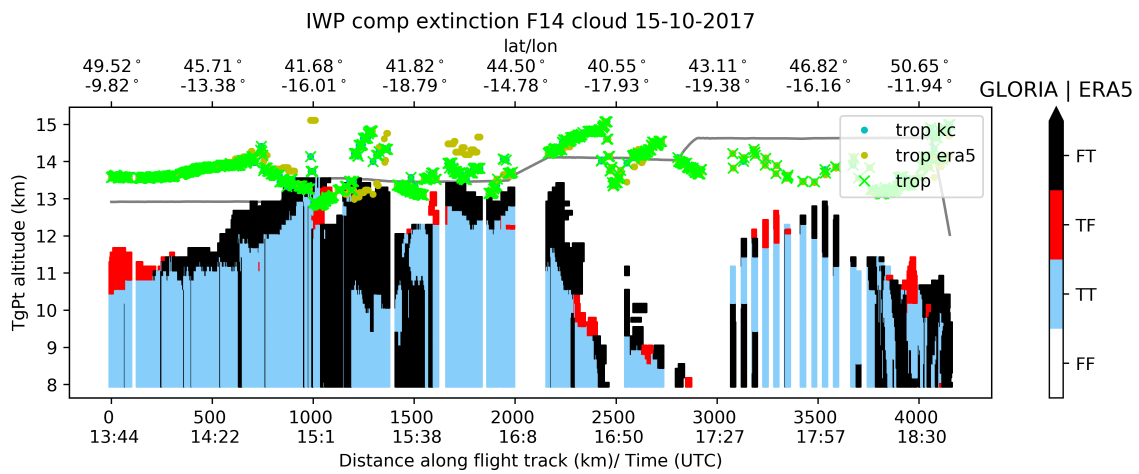
Figure A.11: Cross-sections comparing ERA5 inferred clouds and the identified with the extinction method for GLORIA for flight 12 of the WISE campaign. The results are restricted to levels below flight path (grey line). Color code represents the true-true cases (TT, in light blue) when both datasets identified a cloud; true-false (TF, in red) when a cloud was observed with GLORIA but ERA5 indicated clear air; false-true (FT, in black) when GLORIA indicated clear air and ERA5 registered a cloud and false-false (FF, in white) when both datasets indicated clear air. The blue dots indicate the median tropopause TP_{med} corresponding to the location of the observed cirrus by GLORIA. The yellow dots represent the TP_{med} corresponding to the location of the inferred cirrus with ERA5. The green crosses indicate the combined TP_{med}.The altitude of the tangent points (TgPt) is the y-axis.
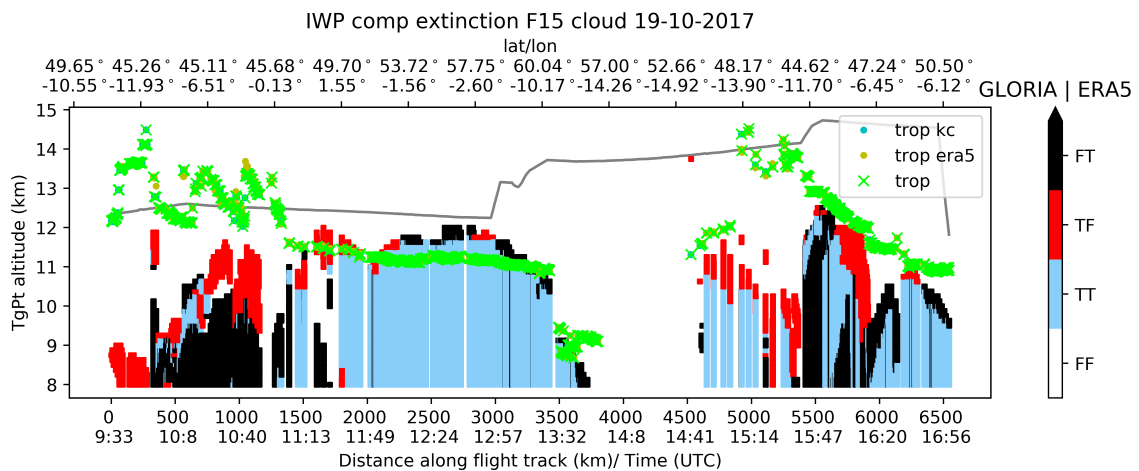
Figure A.12: Cross-sections comparing ERA5 inferred clouds and the identified with the extinction method for GLORIA for flight 13 of the WISE campaign. The results are restricted to levels below flight path (grey line). Color code represents the true-true cases (TT, in light blue) when both datasets identified a cloud; true-false (TF, in red) when a cloud was observed with GLORIA but ERA5 indicated clear air; false-true (FT, in black) when GLORIA indicated clear air and ERA5 registered a cloud and false-false (FF, in white) when both datasets indicated clear air. The blue dots indicate the median tropopause TP_{med} corresponding to the location of the observed cirrus by GLORIA. The yellow dots represent the TP_{med} corresponding to the location of the inferred cirrus with ERA5. The green crosses indicate the combined TP_{med}.The altitude of the tangent points (TgPt) is the y-axis.
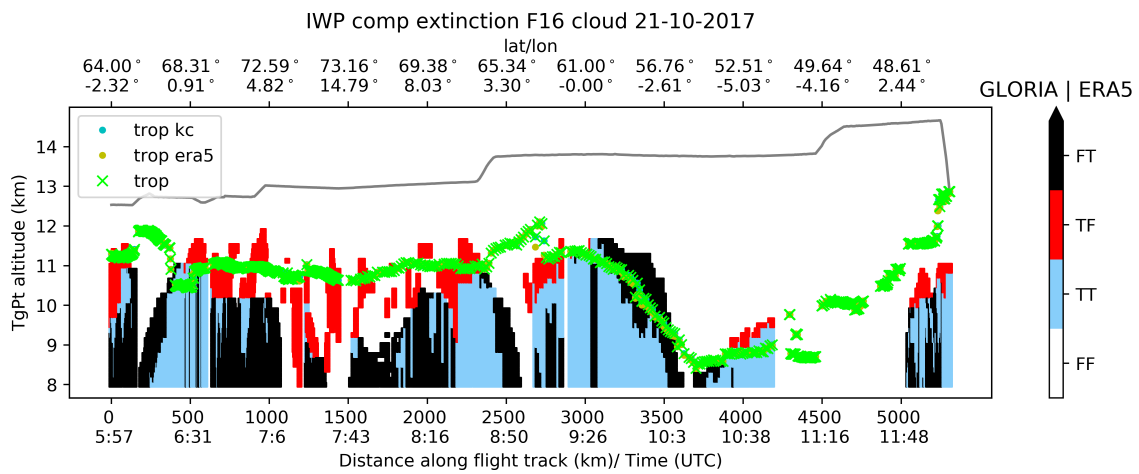
Figure A.13: Cross-sections comparing ERA5 inferred clouds and the identified with the extinction method for GLORIA for flight 14 of the WISE campaign. The results are restricted to levels below flight path (grey line). Color code represents the true-true cases (TT, in light blue) when both datasets identified a cloud; true-false (TF, in red) when a cloud was observed with GLORIA but ERA5 indicated clear air; false-true (FT, in black) when GLORIA indicated clear air and ERA5 registered a cloud and false-false (FF, in white) when both datasets indicated clear air. The blue dots indicate the median tropopause TP_{med} corresponding to the location of the observed cirrus by GLORIA. The yellow dots represent the TP_{med} corresponding to the location of the inferred cirrus with ERA5. The green crosses indicate the combined TP_{med}. The altitude of the tangent points (TgPt) is the y-axis.

Figure A.14: Cross-sections comparing ERA5 inferred clouds and the identified with the extinction method for GLORIA for flight 15 of the WISE campaign. The results are restricted to levels below flight path (grey line). Color code represents the true-true cases (TT, in light blue) when both datasets identified a cloud; true-false (TF, in red) when a cloud was observed with GLORIA but ERA5 indicated clear air; false-true (FT, in black) when GLORIA indicated clear air and ERA5 registered a cloud and false-false (FF, in white) when both datasets indicated clear air. The blue dots indicate the median tropopause TP_{med} corresponding to the location of the observed cirrus by GLORIA. The yellow dots represent the TP_{med} corresponding to the location of the inferred cirrus with ERA5. The green crosses indicate the combined TP_{med}.The altitude of the tangent points (TgPt) is the y-axis.

Figure A.15: Cross-sections comparing ERA5 inferred clouds and the identified with the extinction method for GLORIA for flight 16 of the WISE campaign. The results are restricted to levels below flight path (grey line). Color code represents the true-true cases (TT, in light blue) when both datasets identified a cloud; true-false (TF, in red) when a cloud was observed with GLORIA but ERA5 indicated clear air; false-true (FT, in black) when GLORIA indicated clear air and ERA5 registered a cloud and false-false (FF, in white) when both datasets indicated clear air. The blue dots indicate the median tropopause TP_{med} corresponding to the location of the observed cirrus by GLORIA. The yellow dots represent the TP_{med} corresponding to the location of the inferred cirrus with ERA5. The green crosses indicate the combined TP_{med}.The altitude of the tangent points (TgPt) is the y-axis.
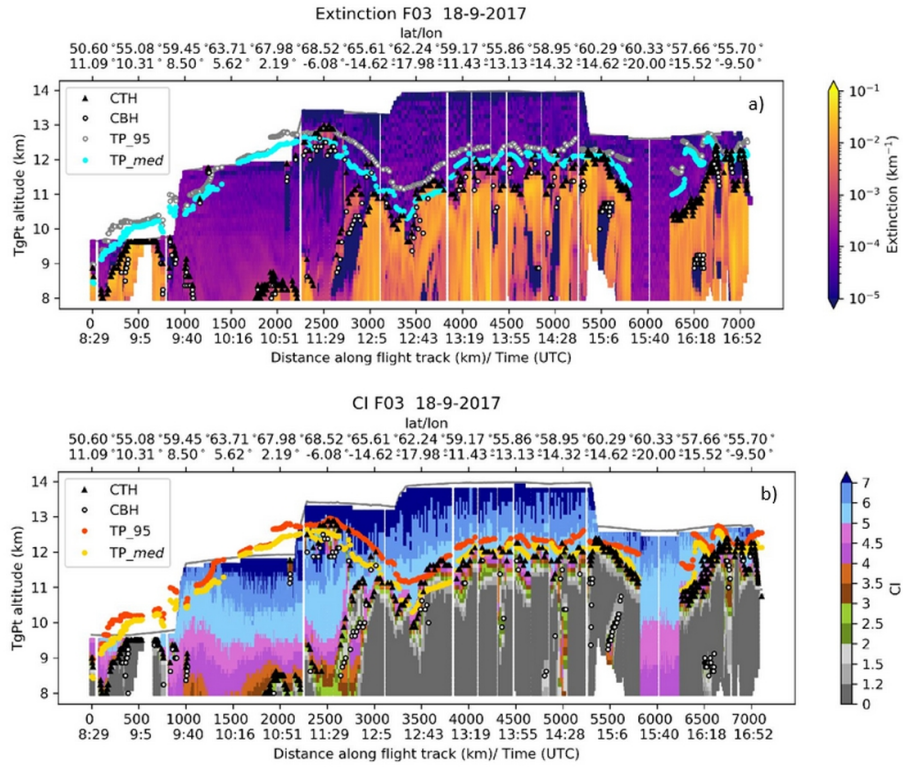
Appendix B

Cross-sections
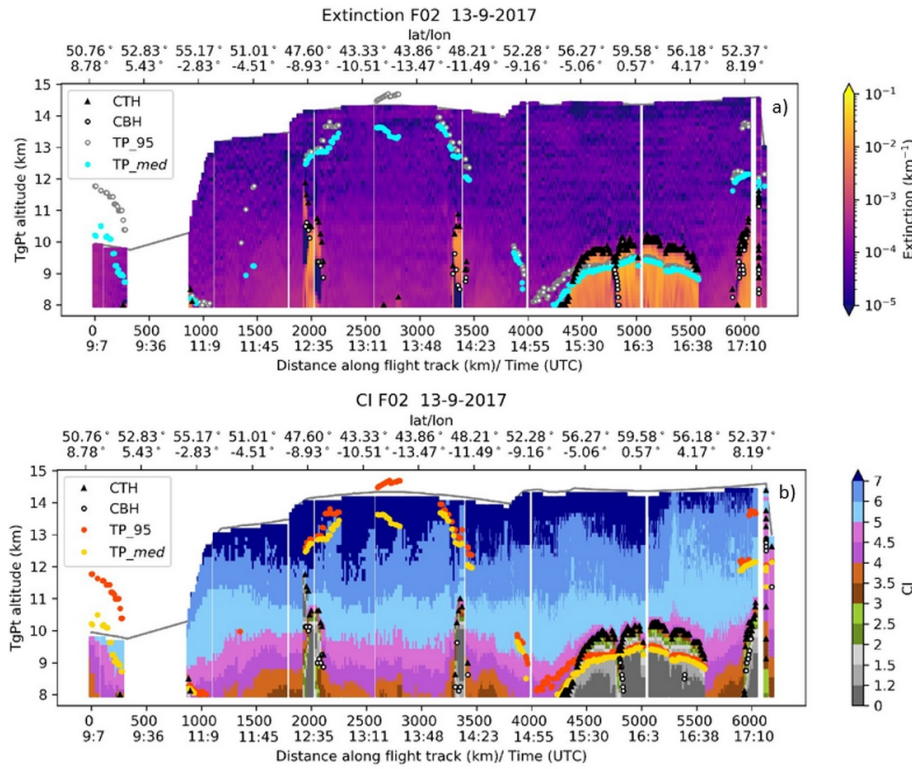
Figure B.1: Cross-sections of extinction (a) and cloud index (b) for flight 2 of the WISE campaign. The results are restricted to levels below flight path. (a) Color code for extinction in km^{-1}. Orange-pink colors indicate the presence of clouds; (b) color code for CI. Depending on the altitude, CI values below 2 to 5 (colors from grey to pink) indicate the presence of clouds. Median tropopause (TP$_{med}$) and the percentile 95 of the tropopause (TP$_{95}$) are represented with orange and yellow circles, respectively. Cloud top height (CTH) and cloud bottom height (CBH) are represented with a black triangle and with a white circle, respectively. The altitude of the tangent points (TgPt) is the y-axis. The white areas in both cross-sections correspond to a first filtering of optically thicker regions (CI < 2).
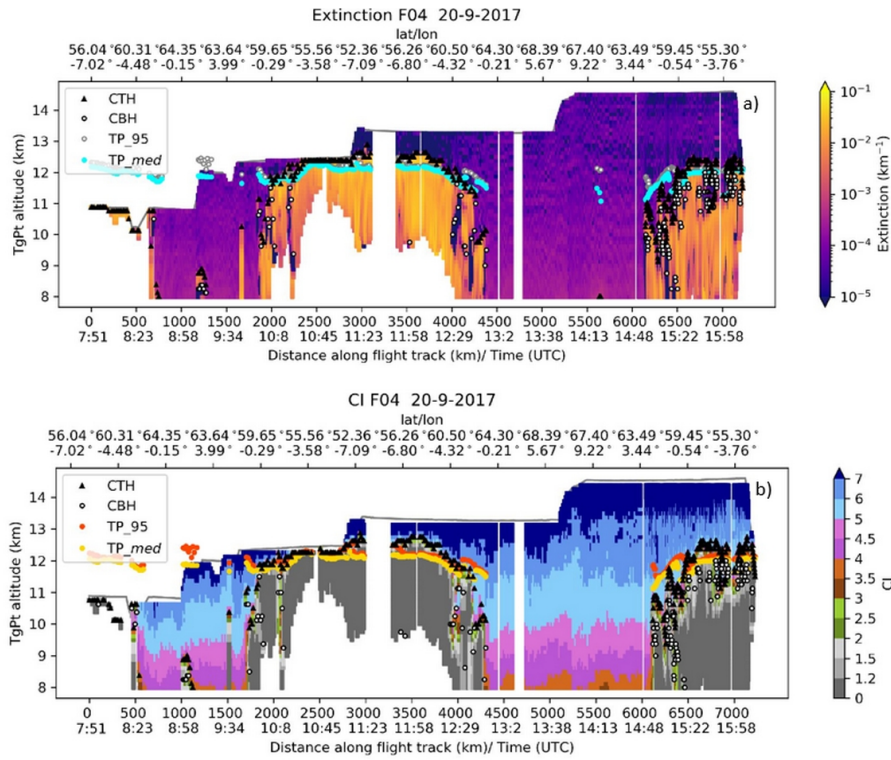
Figure B.2: Cross-sections of extinction (a) and cloud index (b) for flight 3 of the WISE campaign. The results are restricted to levels below flight path. (a) Color code for extinction in km^{-1}. Orange-pink colors indicate the presence of clouds; (b) color code for CI. Depending on the altitude, CI values below 2 to 5 (colors from grey to pink) indicate the presence of clouds. Median tropopause (TP$_{med}$) and the percentile 95 of the tropopause (TP$_{95}$) are represented with orange and yellow circles, respectively. Cloud top height (CTH) and cloud bottom height (CBH) are represented with a black triangle and with a white circle, respectively. The altitude of the tangent points (TgPt) is the y-axis. The white areas in both cross-sections correspond to a first filtering of optically thicker regions (CI < 2).
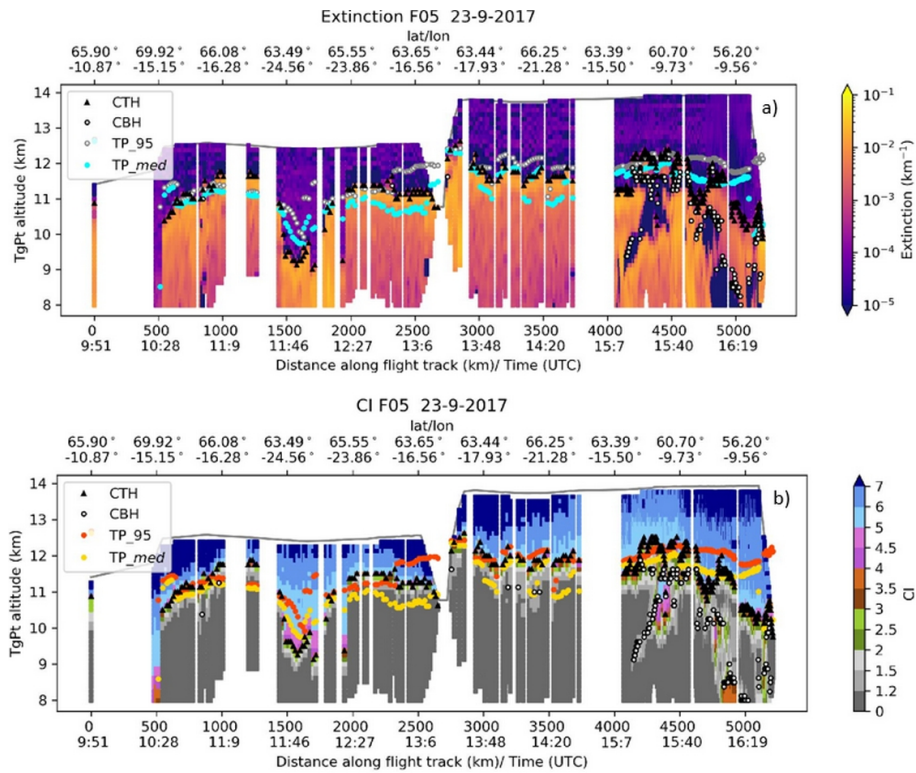
Figure B.3: Cross-sections of extinction (a) and cloud index (b) for flight 4 of the WISE campaign. The results are restricted to levels below flight path. (a) Color code for extinction in km^{-1}. Orange-pink colors indicate the presence of clouds; (b) color code for CI. Depending on the altitude, CI values below 2 to 5 (colors from grey to pink) indicate the presence of clouds. Median tropopause (TP$_{med}$) and the percentile 95 of the tropopause (TP$_{95}$) are represented with orange and yellow circles, respectively. Cloud top height (CTH) and cloud bottom height (CBH) are represented with a black triangle and with a white circle, respectively. The altitude of the tangent points (TgPt) is the y-axis. The white areas in both cross-sections correspond to a first filtering of optically thicker regions (CI < 2).
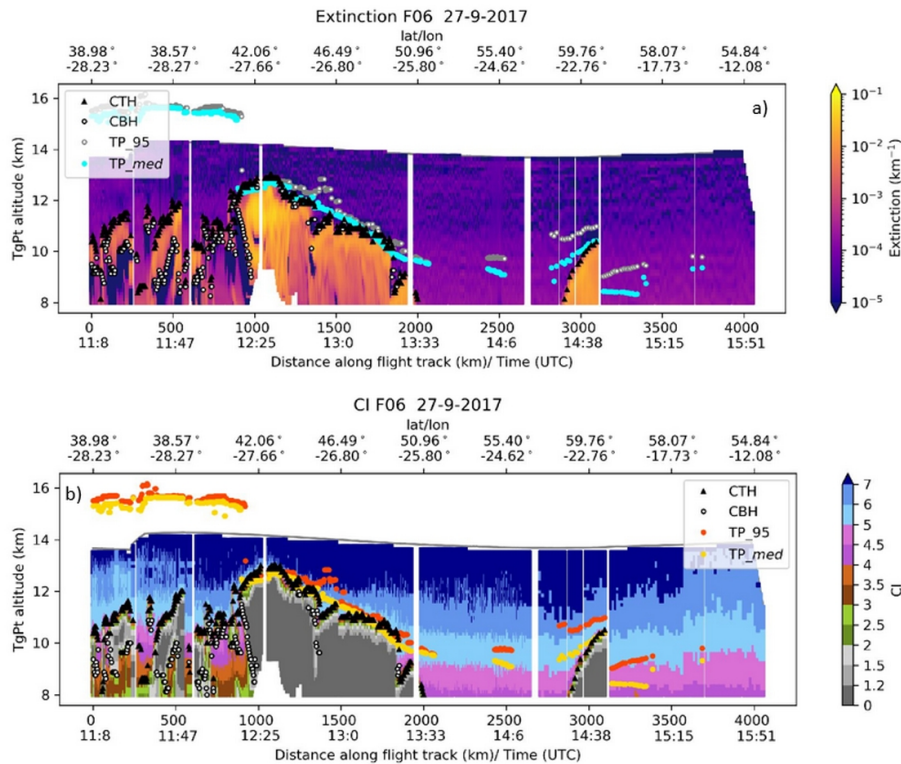
Figure B.4: Cross-sections of extinction (a) and cloud index (b) for flight 5 of the WISE campaign. The results are restricted to levels below flight path. (a) Color code for extinction in km^{-1}. Orange-pink colors indicate the presence of clouds; (b) color code for CI. Depending on the altitude, CI values below 2 to 5 (colors from grey to pink) indicate the presence of clouds. Median tropopause (TP$_{med}$) and the percentile 95 of the tropopause (TP$_{95}$) are represented with orange and yellow circles, respectively. Cloud top height (CTH) and cloud bottom height (CBH) are represented with a black triangle and with a white circle, respectively. The altitude of the tangent points (TgPt) is the y-axis. The white areas in both cross-sections correspond to a first filtering of optically thicker regions (CI < 2).
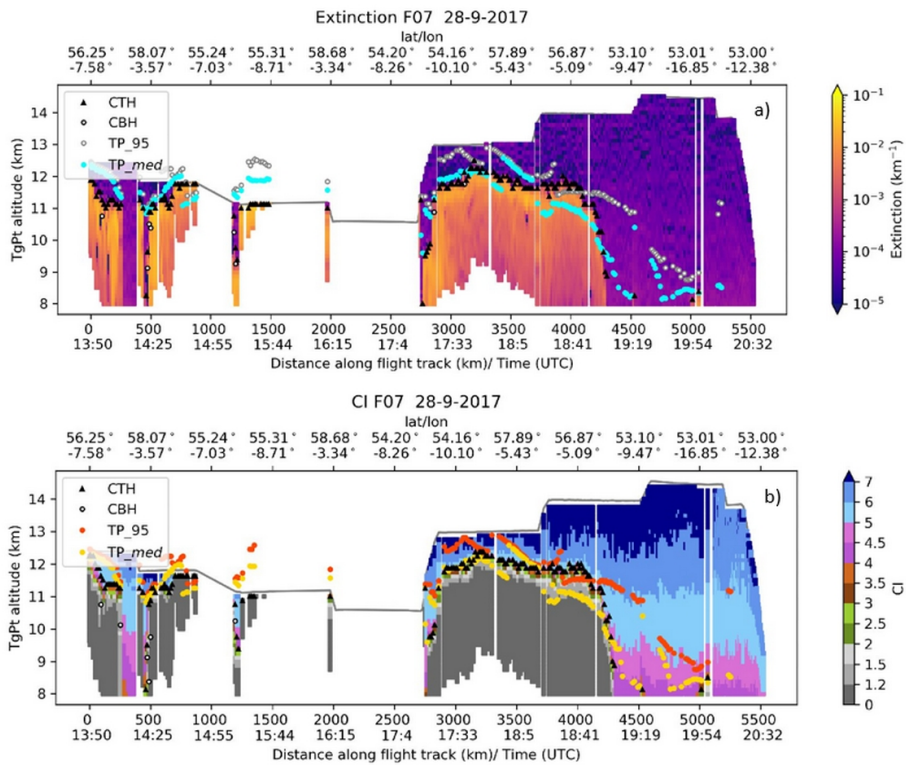
Figure B.5: Cross-sections of extinction (a) and cloud index (b) for flight 6 of the WISE campaign. The results are restricted to levels below flight path. (a) Color code for extinction in km^{-1}. Orange-pink colors indicate the presence of clouds; (b) color code for CI. Depending on the altitude, CI values below 2 to 5 (colors from grey to pink) indicate the presence of clouds. Median tropopause (TP$_{med}$) and the percentile 95 of the tropopause (TP$_{95}$) are represented with orange and yellow circles, respectively. Cloud top height (CTH) and cloud bottom height (CBH) are represented with a black triangle and with a white circle, respectively. The altitude of the tangent points (TgPt) is the y-axis. The white areas in both cross-sections correspond to a first filtering of optically thicker regions (CI < 2).
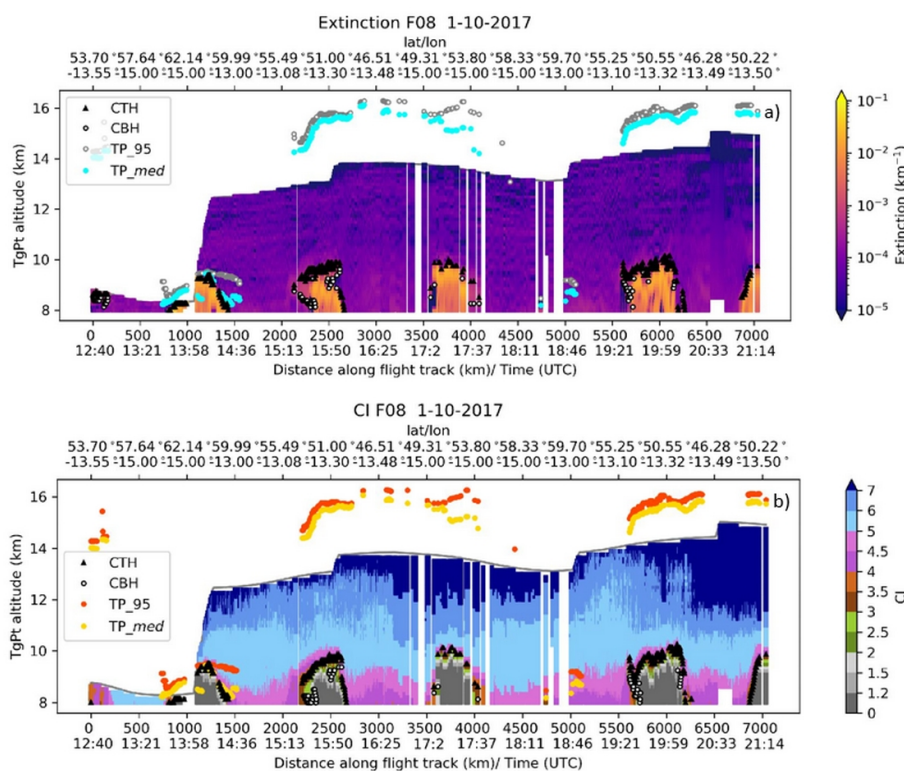
Figure B.6: Cross-sections of extinction (a) and cloud index (b) for flight 7 of the WISE campaign. The results are restricted to levels below flight path. (a) Color code for extinction in km^{-1}. Orange-pink colors indicate the presence of clouds; (b) color code for CI. Depending on the altitude, CI values below 2 to 5 (colors from grey to pink) indicate the presence of clouds. Median tropopause (TP$_{med}$) and the percentile 95 of the tropopause (TP$_{95}$) are represented with orange and yellow circles, respectively. Cloud top height (CTH) and cloud bottom height (CBH) are represented with a black triangle and with a white circle, respectively. The altitude of the tangent points (TgPt) is the y-axis. The white areas in both cross-sections correspond to a first filtering of optically thicker regions (CI < 2).
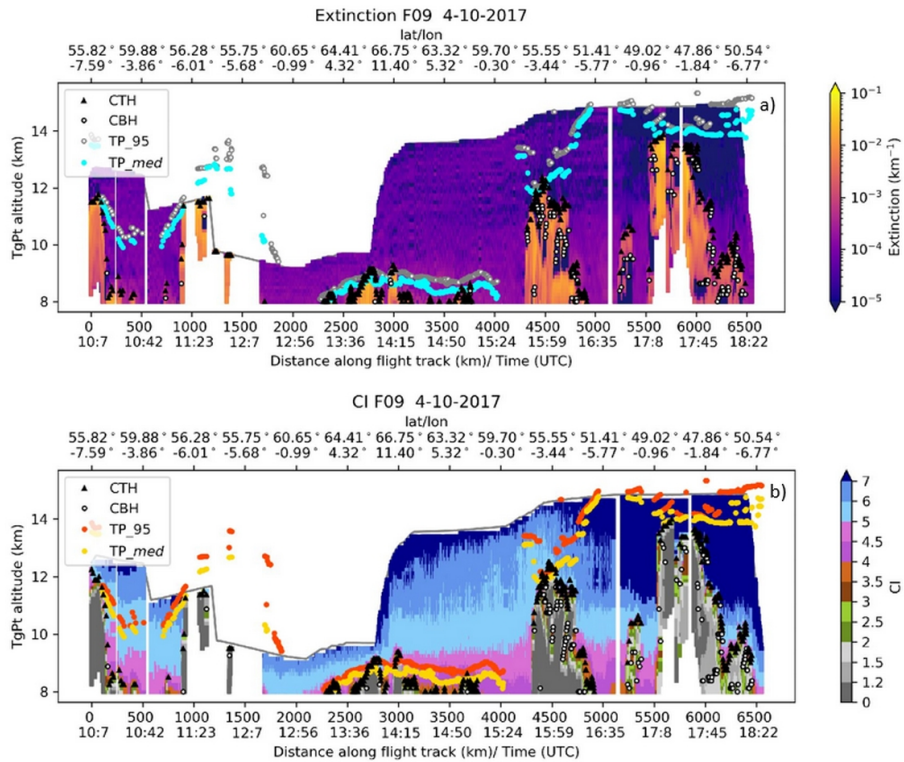
Figure B.7: Cross-sections of extinction (a) and cloud index (b) for flight 8 of the WISE campaign. The results are restricted to levels below flight path. (a) Color code for extinction in km^{-1}. Orange-pink colors indicate the presence of clouds; (b) color code for CI. Depending on the altitude, CI values below 2 to 5 (colors from grey to pink) indicate the presence of clouds. Median tropopause (TP$_{med}$) and the percentile 95 of the tropopause (TP$_{95}$) are represented with orange and yellow circles, respectively. Cloud top height (CTH) and cloud bottom height (CBH) are represented with a black triangle and with a white circle, respectively. The altitude of the tangent points (TgPt) is the y-axis. The white areas in both cross-sections correspond to a first filtering of optically thicker regions (CI < 2).
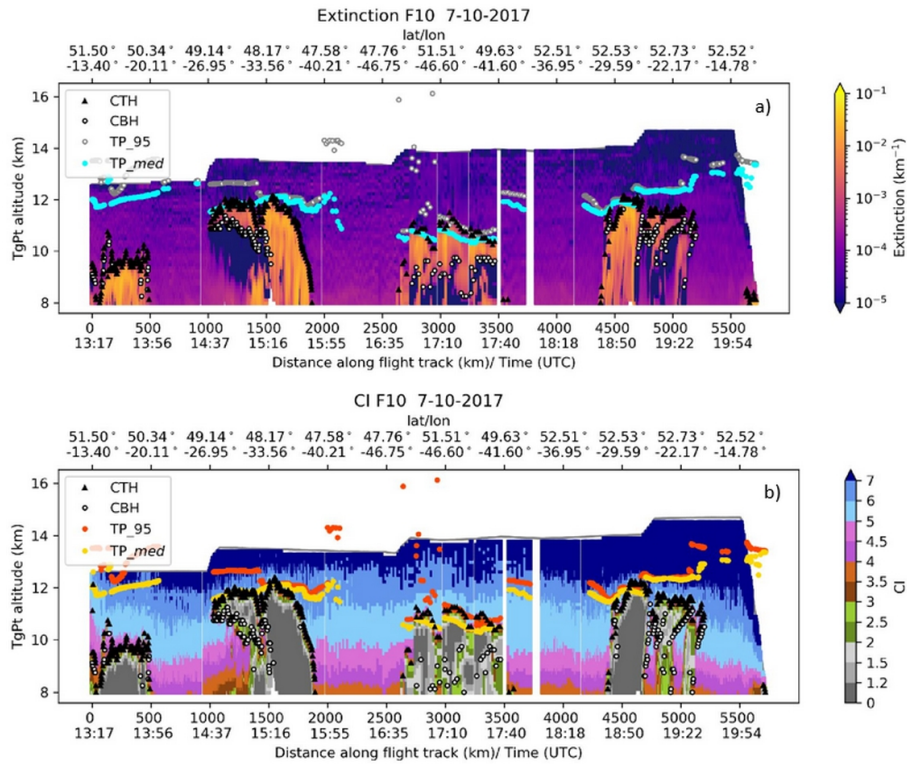
Figure B.8: Cross-sections of extinction (a) and cloud index (b) for flight 9 of the WISE campaign. The results are restricted to levels below flight path. (a) Color code for extinction in km^{-1}. Orange-pink colors indicate the presence of clouds; (b) color code for CI. Depending on the altitude, CI values below 2 to 5 (colors from grey to pink) indicate the presence of clouds. Median tropopause (TP$_{med}$) and the percentile 95 of the tropopause (TP$_{95}$) are represented with orange and yellow circles, respectively. Cloud top height (CTH) and cloud bottom height (CBH) are represented with a black triangle and with a white circle, respectively. The altitude of the tangent points (TgPt) is the y-axis. The white areas in both cross-sections correspond to a first filtering of optically thicker regions (CI < 2).

Figure B.9: Cross-sections of extinction (a) and cloud index (b) for flight 10 of the WISE campaign. The results are restricted to levels below flight path. (a) Color code for extinction in km^{-1}. Orange-pink colors indicate the presence of clouds; (b) color code for CI. Depending on the altitude, CI values below 2 to 5 (colors from grey to pink) indicate the presence of clouds. Median tropopause (TP$_{med}$) and the percentile 95 of the tropopause (TP$_{95}$) are represented with orange and yellow circles, respectively. Cloud top height (CTH) and cloud bottom height (CBH) are represented with a black triangle and with a white circle, respectively. The altitude of the tangent points (TgPt) is the y-axis. The white areas in both cross-sections correspond to a first filtering of optically thicker regions (CI < 2).
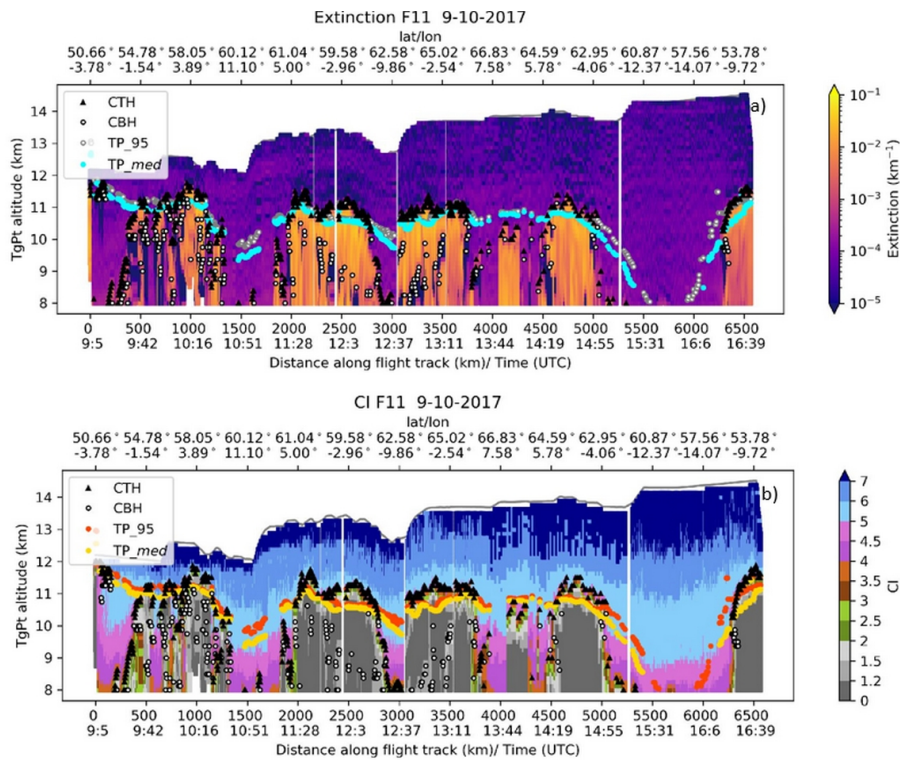
Figure B.10: Cross-sections of extinction (a) and cloud index (b) for flight 11 of the WISE campaign. The results are restricted to levels below flight path. (a) Color code for extinction in km^{-1}. Orange-pink colors indicate the presence of clouds; (b) color code for CI. Depending on the altitude, CI values below 2 to 5 (colors from grey to pink) indicate the presence of clouds. Median tropopause (TP$_{med}$) and the percentile 95 of the tropopause (TP$_{95}$) are represented with orange and yellow circles, respectively. Cloud top height (CTH) and cloud bottom height (CBH) are represented with a black triangle and with a white circle, respectively. The altitude of the tangent points (TgPt) is the y-axis. The white areas in both cross-sections correspond to a first filtering of optically thicker regions (CI < 2).
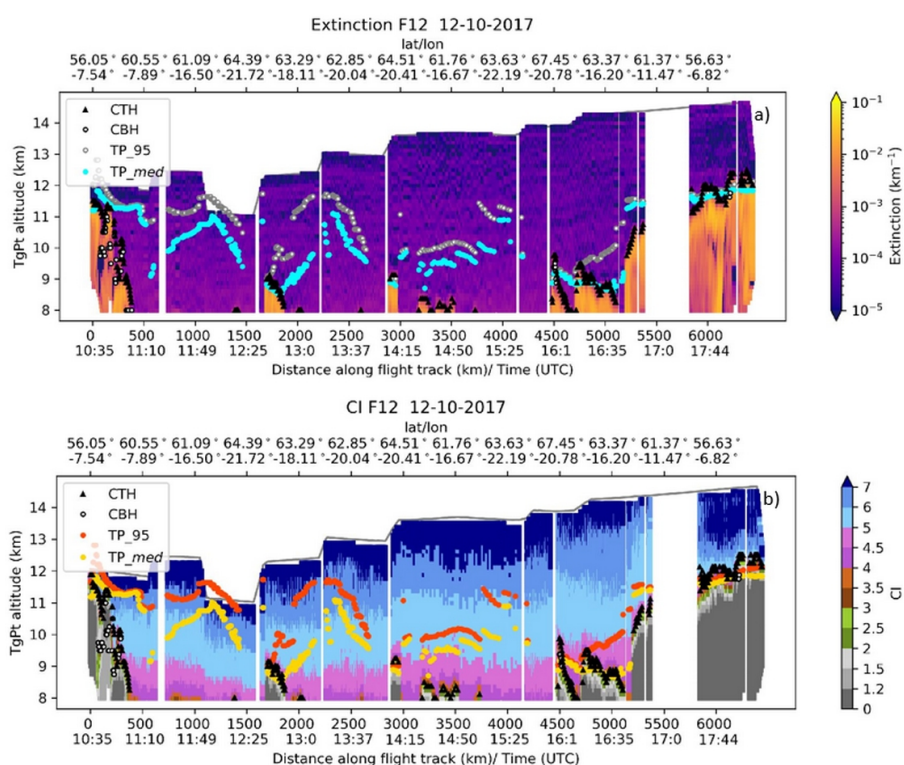
Figure B.11: Cross-sections of extinction (a) and cloud index (b) for flight 12 of the WISE campaign. The results are restricted to levels below flight path. (a) Color code for extinction in km^{-1}. Orange-pink colors indicate the presence of clouds; (b) color code for CI. Depending on the altitude, CI values below 2 to 5 (colors from grey to pink) indicate the presence of clouds. Median tropopause (TP$_{med}$) and the percentile 95 of the tropopause (TP$_{95}$) are represented with orange and yellow circles, respectively. Cloud top height (CTH) and cloud bottom height (CBH) are represented with a black triangle and with a white circle, respectively. The altitude of the tangent points (TgPt) is the y-axis. The white areas in both cross-sections correspond to a first filtering of optically thicker regions (CI < 2).
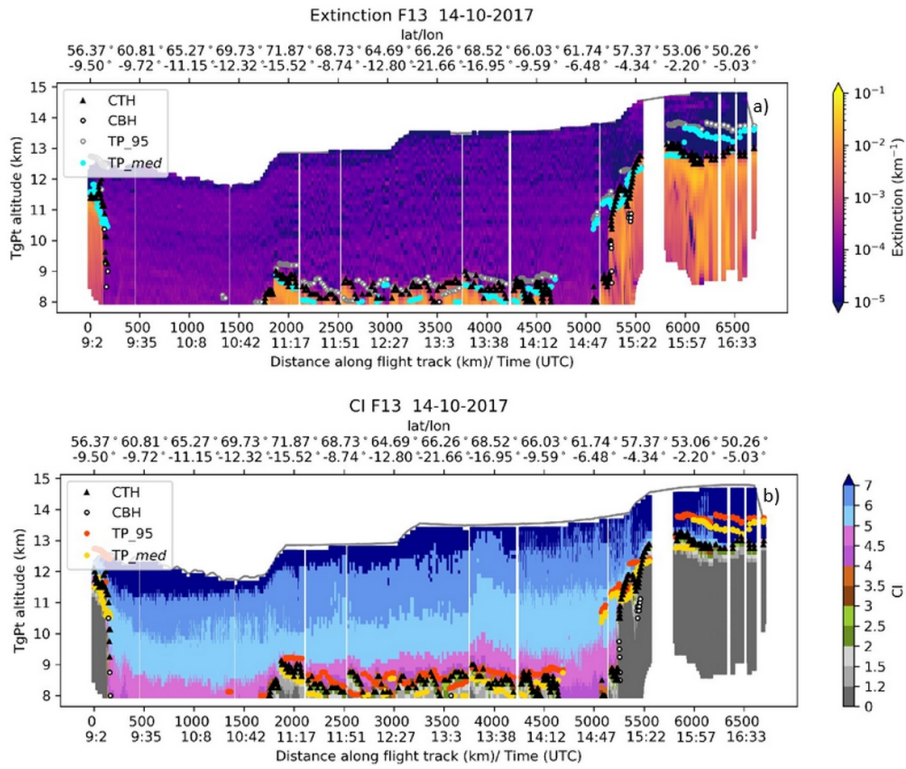
149

Figure B.12: Cross-sections of extinction (a) and cloud index (b) for flight 13 of the WISE campaign. The results are restricted to levels below flight path. (a) Color code for extinction in km^{-1}. Orange-pink colors indicate the presence of clouds; (b) color code for CI. Depending on the altitude, CI values below 2 to 5 (colors from grey to pink) indicate the presence of clouds. Median tropopause (TP$_{med}$) and the percentile 95 of the tropopause (TP$_{95}$) are represented with orange and yellow circles, respectively. Cloud top height (CTH) and cloud bottom height (CBH) are represented with a black triangle and with a white circle, respectively. The altitude of the tangent points (TgPt) is the y-axis. The white areas in both cross-sections correspond to a first filtering of optically thicker regions (CI < 2).
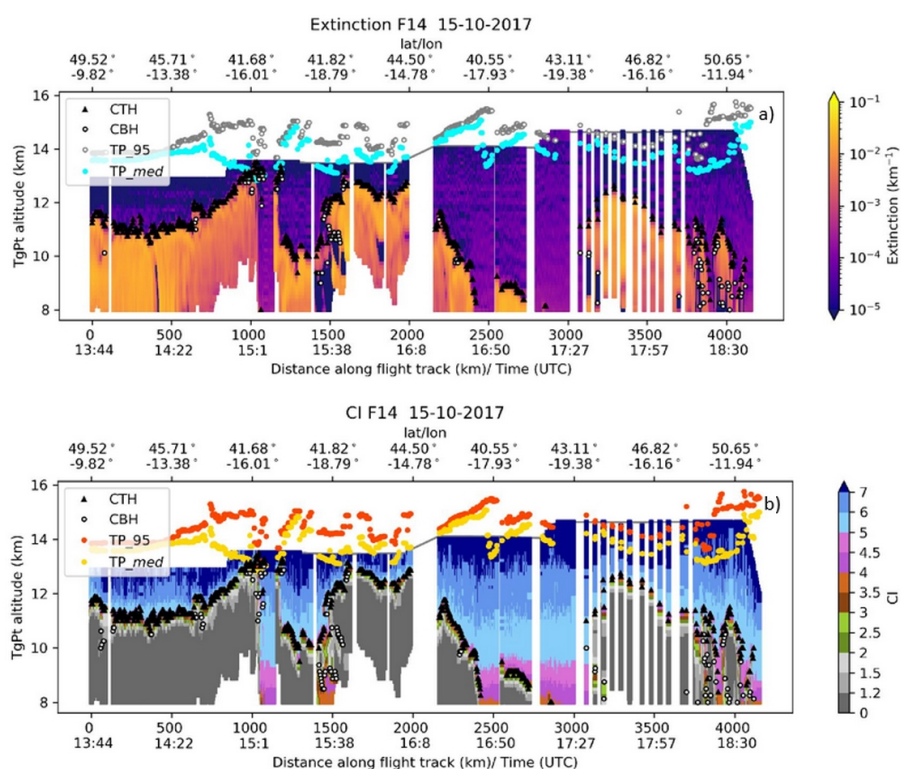
Figure B.13: Cross-sections of extinction (a) and cloud index (b) for flight 14 of the WISE campaign. The results are restricted to levels below flight path. (a) Color code for extinction in km^{-1}. Orange-pink colors indicate the presence of clouds; (b) color code for CI. Depending on the altitude, CI values below 2 to 5 (colors from grey to pink) indicate the presence of clouds. Median tropopause (TP$_{med}$) and the percentile 95 of the tropopause (TP$_{95}$) are represented with orange and yellow circles, respectively. Cloud top height (CTH) and cloud bottom height (CBH) are represented with a black triangle and with a white circle, respectively. The altitude of the tangent points (TgPt) is the y-axis. The white areas in both cross-sections correspond to a first filtering of optically thicker regions (CI < 2).
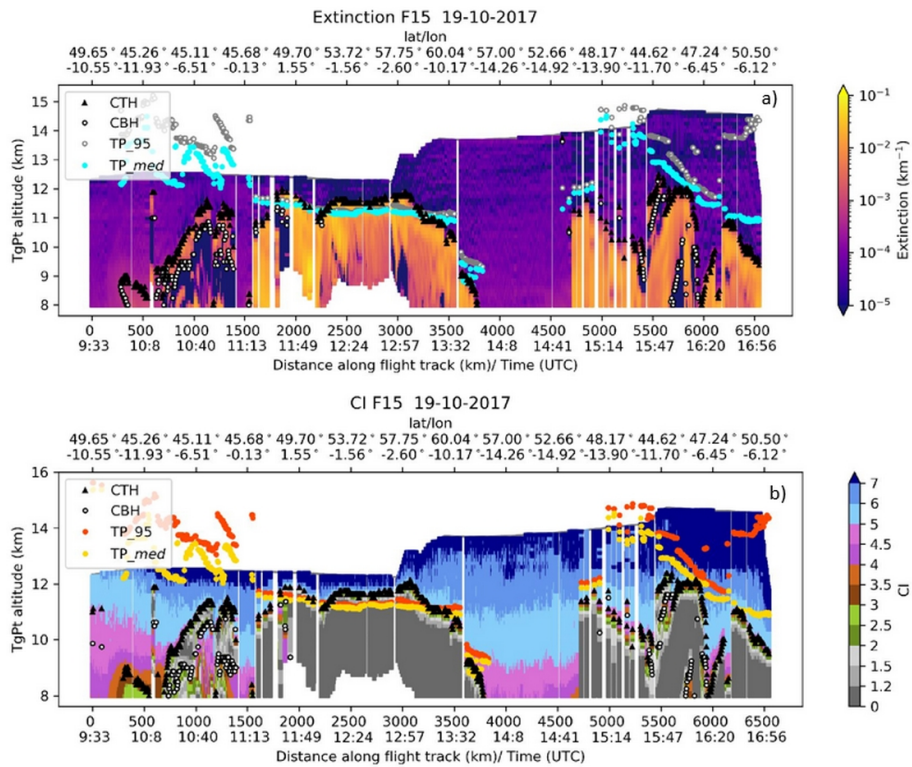
Figure B.14: Cross-sections of extinction (a) and cloud index (b) for flight 15 of the WISE campaign. The results are restricted to levels below flight path. (a) Color code for extinction in km^{-1}. Orange-pink colors indicate the presence of clouds; (b) color code for CI. Depending on the altitude, CI values below 2 to 5 (colors from grey to pink) indicate the presence of clouds. Median tropopause (TP$_{med}$) and the percentile 95 of the tropopause (TP$_{95}$) are represented with orange and yellow circles, respectively. Cloud top height (CTH) and cloud bottom height (CBH) are represented with a black triangle and with a white circle, respectively. The altitude of the tangent points (TgPt) is the y-axis. The white areas in both cross-sections correspond to a first filtering of optically thicker regions (CI < 2).
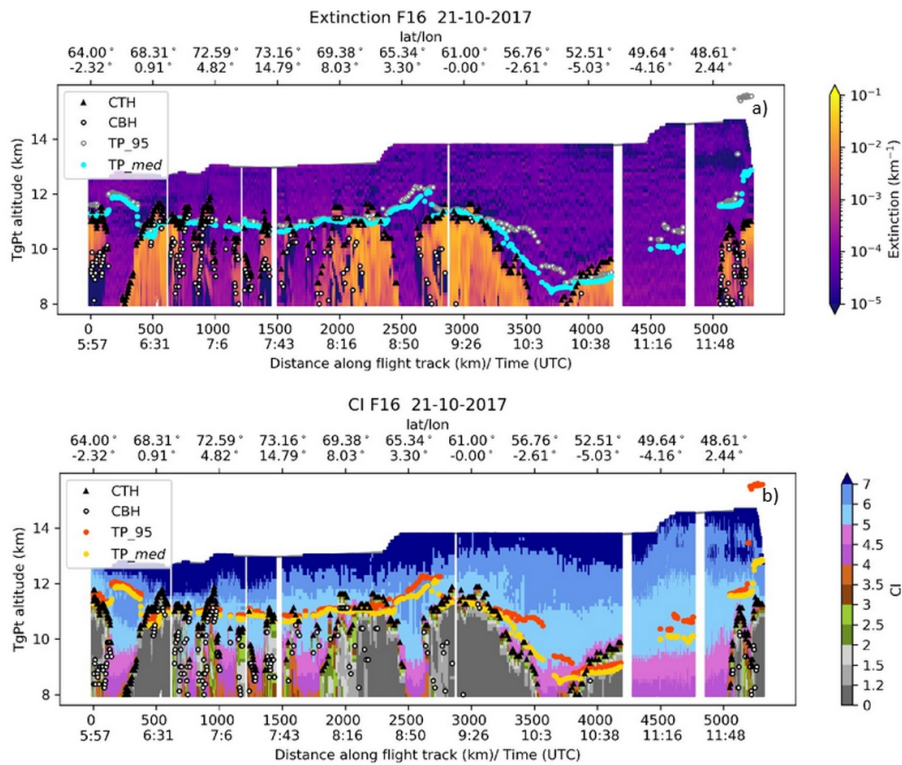
Figure B.15: Cross-sections of extinction (a) and cloud index (b) for flight 16 of the WISE campaign. The results are restricted to levels below flight path. (a) Color code for extinction in km^{-1}. Orange-pink colors indicate the presence of clouds; (b) color code for CI. Depending on the altitude, CI values below 2 to 5 (colors from grey to pink) indicate the presence of clouds. Median tropopause (TP$_{med}$) and the percentile 95 of the tropopause (TP$_{95}$) are represented with orange and yellow circles, respectively. Cloud top height (CTH) and cloud bottom height (CBH) are represented with a black triangle and with a white circle, respectively. The altitude of the tangent points (TgPt) is the y-axis. The white areas in both cross-sections correspond to a first filtering of optically thicker regions (CI < 2).

Acknowledgments

I would like to begin by thanking Prof. Dr. Martin Riese and Dr. Reinhold Spang for giving me the opportunity of joining the IEK - 7 institute to pursue my doctorate. Also for giving me the chance of participating in two international campaigns (WISE and SOUTHTRAC), in conferences, workshops and summer schools. These experiences were fundamental in my development, as they are perfect for sharing the scientific work, discussing and meeting new people. Special thanks to Dr. Jörn Ungermann for all his support with JURASSIC and GLORIA, answering all my questions and helping me to understand them a little bit more. Many thanks go to Dr. Martina Krämer and Dr. Christian Rolf for their interesting discussions about cirrus clouds and their help using CLaMS-Ice. I would also like to thank Dr. Sabine Griessbach for our many discussions about discrimination of aerosols and clouds, radiative transfer and ice particle properties and Dr. Michael Höpfner for the interesting conversation about radiative transfer. I also want to thank Markus Geldenhuys for sharing his knowledge about meteorology and to all my colleagues in IEK-7, that made these years in Jülich so fun and memorable, from both a professional perspective as from a social one.

To my friends: Ana, Laura and Miriam; Ana, Eva, Mayte and Miriam; Clara and Miriam. It was always great meeting you when I was back in Spain and, of course, our Skype talks. I also want to mention my friend Nuria, it was fantastic sharing with you so many experiences during our PhDs. I am looking forward for more and who knows, maybe even a collaboration! Thanks also to Philipp for always supporting me, specially during the last months while writing this thesis. Last, a huge thank you to my family for their support and encouragement, without them, none of this would be possible. Once more, thank you.